

TOPICAL REVIEW

# Cavity QED with hybrid nanocircuits: from atomic-like physics to condensed matter phenomena

To cite this article: Audrey Cottet *et al* 2017 *J. Phys.: Condens. Matter* **29** 433002

View the [article online](#) for updates and enhancements.

## Related content

- [Supplementary data](#)
- [Physics of lateral triple quantum-dot molecules with controlled electron numbers](#)  
Chang-Yu Hsieh, Yun-Pil Shim, Marek Korkusinski et al.
- [Spin-polarized supercurrents for spintronics: a review of current progress](#)  
Matthias Eschrig

## Topical Review

# Cavity QED with hybrid nanocircuits: from atomic-like physics to condensed matter phenomena

Audrey Cottet<sup>1</sup>, Matthieu C Dartiailh<sup>1</sup>, Matthieu M Desjardins<sup>1</sup>,  
Tino Cubaynes<sup>1</sup>, Lauriane C Contamin<sup>1</sup>, Matthieu Delbecq<sup>1</sup>,  
J eremie J Viennot<sup>1</sup>, Laure E Bruhat<sup>1</sup>, Benoit Dou ot<sup>2</sup> and Takis Kontos<sup>1</sup>

<sup>1</sup> Laboratoire Pierre Aigrain, Ecole Normale Sup erieure, CNRS UMR 8551, Laboratoire associ e aux universit es Pierre et Marie Curie et Denis Diderot, 24, rue Lhomond, 75231 Paris Cedex 05, France

<sup>2</sup> Sorbonne Universit es, Universit  Pierre et Marie Curie, CNRS, LPTHE, UMR 7589, 4 place Jussieu, 75252 Paris Cedex 05, France

E-mail: [cottet@lpa.ens.fr](mailto:cottet@lpa.ens.fr)

Received 31 January 2017

Accepted for publication 23 June 2017

Published 19 September 2017



## Abstract

Circuit QED techniques have been instrumental in manipulating and probing with exquisite sensitivity the quantum state of superconducting quantum bits coupled to microwave cavities. Recently, it has become possible to fabricate new devices in which the superconducting quantum bits are replaced by hybrid mesoscopic circuits combining nanoconductors and metallic reservoirs. This mesoscopic QED provides a new experimental playground to study the light–matter interaction in electronic circuits. Here, we present the experimental state of the art of mesoscopic QED and its theoretical description. A first class of experiments focuses on the artificial atom limit, where some quasiparticles are trapped in nanocircuit bound states. In this limit, the circuit QED techniques can be used to manipulate and probe electronic degrees of freedom such as confined charges, spins, or Andreev pairs. A second class of experiments uses cavity photons to reveal the dynamics of electron tunneling between a nanoconductor and fermionic reservoirs. For instance, the Kondo effect, the charge relaxation caused by grounded metallic contacts, and the photo-emission caused by voltage-biased reservoirs have been studied. The tunnel coupling between nanoconductors and fermionic reservoirs also enable one to obtain split Cooper pairs, or Majorana bound states. Cavity photons represent a qualitatively new tool to study these exotic condensed matter states.

Keywords: cavity quantum electrodynamics, quantum dots, quantum transport

(Some figures may appear in colour only in the online journal)

## 1. Introduction

Since the 1980s, the continual progress of nanofabrication techniques has enabled the fabrication of a wide diversity of nanoelectronic devices which reveal the oddities of quantum mechanics when placed at low temperatures. The strong confinement of electrons in narrow conductors leads

to a quantization of transport into a few transverse channels. This phenomenon has been observed for instance in quantum point contacts made in a two-dimensional electron gas in a semiconductor [1], or in break-junctions between metals [2], where the electric current can be carried by a very low number of transverse channels. Another major ingredient of nanoelectronics is the longitudinal confinement of electrons between

two potential barriers along the transport path [3]. This leads to the formation of quantum dots with a discrete energy spectrum, which are often seen as artificial atoms. The fabrication of quantum dot circuits has reached a very high level of control in two-dimensional electron gas structures, where small quasi-zero dimensional dots are contacted to large two-dimensional reservoirs through quantum point contacts [4]. Interesting alternatives are offered by self-assembled quantum dots [5], carbon nanotubes [6] and semiconducting nanowires [7]. To form a nanocircuit with these nanoconductors, one must contact them with metallic electrodes, which can be made out of normal metals, ferromagnets or superconductors. Due to the versatility of nanofabrication techniques, many circuit configurations can be used, with for instance multiple metallic contacts, or superconducting flux loops. This leads to a large variety of configurations to study quantum transport and obtain new electronic functionalities. For instance, a quantum dot coupled to ferromagnetic contacts can show a ferromagnetic proximity effect which is interesting for the control of spin transport [8] or for local spin manipulations [9]. Another intriguing example, the Cooper pair splitter, enables the spatial separation of the two spin-entangled electrons from a Cooper pair into two different quantum dots, which could be an interesting resource for quantum information [10]. Finally, semiconducting nanowires coupled to superconductors raise a strong interest in the context of the search for topological matter and Majorana bound states [11]. In these three examples, the coupling between the nanoconductors and the superconducting or ferromagnetic reservoirs deeply modifies the electronic properties of the nanoconductors. The hybrid nature of nanoelectronics devices therefore appears as an essential feature.

The first nanoelectronics experiments were naturally based on dc transport measurements. However, it soon became apparent that studying the response of nanocircuits to a microwave excitation was also very interesting. For instance, photo-assisted tunneling was observed in quantum dot circuits, either between a dot and a reservoir [12] or inside a double quantum dot [13]. Microwave irradiation was used to investigate the Kondo physics in a quantum dot with normal metal reservoirs [14]. Radio-frequency single electron transistors [15] were used for the electrometry of quantum dots [16–18]. Wide-band [19] and resonant [20, 21] techniques were developed to measure the impedance of quantum dot circuits. Eventually, microwaves were used to perform coherent manipulations of charges [22] or spins [23, 24] in double quantum dots.

A new surge in the microwave operation of electric nanocircuits is now starting under the influence of cavity and circuit quantum electrodynamics (QED). These experiments study respectively atoms strongly coupled to high finesse superconducting mirror cavities [25], and superconducting Josephson circuits strongly coupled to microwave resonators [26, 27]. In both cases, one can study the interaction of light and matter at the most elementary level because the cavity can trap a controlled low number of photons with a high spectral purity. Furthermore, the atoms and Josephson circuits behave as effective two-level systems. By analogy with these experiments, the idea of combining quantum dot circuits and microwave cavities

emerged theoretically, mainly with the motivation of using quantum dots as quantum bits for quantum information science [28, 29]. In that context, quantum dot circuits are operated in a well confined regime, i.e. the tunnel junctions between the dots and reservoirs are very opaque in order to minimize possible decoherence due to these reservoirs, and the metallic reservoirs are grounded to prevent dc transport. Several strategies are possible to reach the strong coupling regime between a nanocircuit and cavity photons. In particular, one can use the charge [30–32] or spin degree of freedom [34] of a double quantum dot, or Andreev bound states on a narrow superconducting contact [35]. This could offer new means to encode and manipulate quantum information in the context of the development of quantum computing and quantum communication.

Nevertheless, using nanocircuits coupled to microwave cavities to mimic atomic cavity QED or circuit QED experiments is a bit restrictive, since it evades quantum transport effects which occur in out-of-equilibrium conditions, as well as strong correlation effects caused by highly transparent dot-metal contacts. Along this direction, it appears that the use of microwave cavities combined with hybrid nanocircuits enables experiments with no analogue in atomic cavity QED or metallic circuit QED. Indeed, cavity photons provide means to study quantum transport under a new perspective and with very high sensitivity. For instance, they can give direct access to the out-of-equilibrium state occupation of a double quantum dot [36], reservoir-induced quantum charge relaxation in a single dot [37], or photo-assisted tunneling processes [37–41]. They can also represent a powerful tool to characterize exotic condensed matter states caused by the existence of the dot/reservoir interfaces, such as Kondo clouds [167], split Cooper pairs [42, 43], or Majorana bound states [44–49].

Following [50], we will refer to experiments combining microwave cavities and electronic nanocircuits as mesoscopic QED experiments, because the metallic reservoirs in a nanocircuit are typically separated by a micronic distance (see for instance figure 1(c)). The purpose of this short review is to introduce this recent but fast growing new field of research and give possible directions for its future developments. In section 2, we describe the mesoscopic QED architecture. In section 3, we present a theoretical description of mesoscopic QED devices, from the mesoscopic QED Hamiltonian to the semiclassical description of the cavity signals. In section 4, we review experiments performed so far in the artificial atom limit. In section 5, we discuss mesoscopic QED experiments beyond the artificial atom limit, i.e. when the tunneling dynamics between the nanoconductor and metallic reservoir leads to significant effects. Section 6 presents conclusions and perspectives. In this review we use  $\hbar = 1$  in most equations, and we will thus define many parameters as pulsations. We note  $e$  the absolute value of the electron charge ( $e > 0$ ).

## 2. Building a mesoscopic QED experiment

### 2.1. Embedding a hybrid nanocircuit in a microwave cavity

The combination of hybrid nanocircuits with coplanar microwave cavities pushes further the on-chip design initially

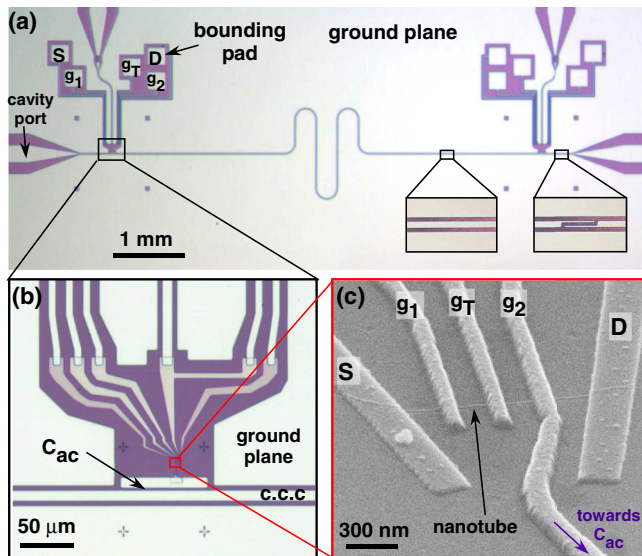


**Figure 1.** Example of mesoscopic QED device. (a) Optical micrograph of a coplanar waveguide microwave resonator coupled to a hybrid nanocircuit. The squares are bonding pads for the nanocircuit, which are isolated from the cavity ground plane and carry dc voltage or current. The left inset shows a zoom on the coplanar waveguide, which is a central conductor surrounded by two ground planes. The right inset shows one of the capacitances which interrupts the waveguide to form a microwave cavity (b) Closeup on the connection between the cavity and the nanocircuit. In this particular sample, an extra superconducting pad was placed next to the resonator line, providing a large coupling capacitance  $C_{ac}$  between the cavity central conductor (c.c.c.) and one of the sample gates (c) Scanning electron micrograph of the nanocircuit coupled to the cavity—here a single wall carbon nanotube (SWNT) connected to source and drain (S and D) reservoirs as well as three top gates  $g_1$ ,  $g_2$  and  $g_T$ . Adapted figure with permission from [36], Copyright (2014) by the American Physical Society.

introduced in the context of circuit QED experiments to control and read out the state of a superconducting quantum bit [26]. Many different types of nanoconductors have already been embedded in coplanar cavities, such as lateral quantum dots defined on GaAs/AlGaAs heterostructures [51, 52] or Si/SiGe heterostructures [33, 53], quasi-one dimensional conductors such as carbon nanotubes [54, 55], InAs nanowires [56–58], or InSb nanowires [59], but also graphene quantum dots [60] and atomic contacts [35]. Different types of metallic contacts can be used, such as normal metals, superconductors [37] and ferromagnets with collinear [8] or non-collinear magnetizations [34, 61]. Therefore, a large variety of geometries and situations can be studied. Figure 1 shows an example of mesoscopic QED sample. Here, the hybrid nanocircuit is a double quantum dot fabricated out of a carbon nanotube on top of which source (S), drain (D), and top dc gates ( $g_1$ ,  $g_2$  and  $g_T$ ) have been deposited (figure 1(c)). The double dot is coupled capacitively to the cavity central conductor (c.c.c.), through the capacity  $C_{ac}$ , near a cavity electric field antinode (figure 1(b)). The cavity central conductor is interrupted by on-chip capacitances such as the one visible in the right inset of figure 1(a). Openings are fabricated across the cavity ground plane to allow for an electric connection of the source, drain and gate electrodes of the double dot at bonding pads visible as squares in figure 1(a). These openings must

be designed in order to preserve the cavity quality factor. To avoid spurious photon dissipation, it is also important to introduce as little conductive material as possible close to the cavity. In experiments realized with semiconducting nanowires and first experiments realized with carbon nanotubes, numerous nanoconductors were dispersed on the substrate during the fabrication process. Stamping techniques [62] are now used to deposit fewer carbon nanotubes inside the cavity [63], which leads to cavity quality factors  $Q_0 > 10\,000$  [34, 37]. In the case of nanostructures based on two-dimensional electron gases, the coupling to the whole electronic substrate seems more difficult to avoid. Among other feats of technical progress, one can mention the measurement of a double quantum dot in a cavity by using a Josephson parametric amplifier which considerably speeds up data acquisition [64]. Microwave-frequency resonators based on NbTiN nanowires [65] and SQUID arrays [32] have recently been developed in order to increase the cavity electric field by a factor of ten in comparison with standard coplanar cavities based on Al or Nb metallic strips. This can be used to increase the light–matter coupling. Other alternative cavity technologies compatible with nanocircuit architectures are being investigated [66–68].

## 2.2. Tailoring the spectrum of a hybrid nanocircuit with fermionic reservoirs

One important specificity of circuit QED experiments performed with superconducting quantum bits, in comparison with atomic cavity QED experiments, is that the spectrum of a superconducting quantum bit is not set by nature like the spectrum of an atom, but can be designed at the nanolithography stage by choosing the circuit geometry and the value of the capacitive and Josephson elements. This spectrum can also be tuned during the experiment using gate voltages or magnetic fluxes. This represents a significant advantage in performing various tasks such as the selective microwave control of individual quantum bits in an experiment. In mesoscopic QED, the use of fermionic reservoirs offers other resources to tailor the spectrum of a nanocircuit. One must find configurations where the nanocircuit displays energy scales comparable with the cavity frequency. In this section, we discuss different possibilities to do so.

For simplicity, we first consider the case where two normal metal reservoirs delimit a single quantum dot with length  $\ell$  inside a single channel nanoconductor (figure 2(a)). In a non-interacting scattering picture, the phase shift acquired by an electron in crossing the dot once is  $\delta(E) = \ell(k_F + (E - E_F)/v_F)$ , where  $E_F$ ,  $k_F$  and  $v_F$  are the Fermi energy, wavevector and velocity inside the nanoconductor and  $E$  is the electron energy treated at first order. The electron is reflected on the normal metal contacts with a spin-independent reflection phase  $\varphi_{r,\sigma} = \varphi_r$ , so that the dot orbital energies are given by the resonant condition  $2\delta(E) + 2\varphi_r = 2\pi n$ , with  $n \in \mathbb{N}$  (see figure 2(a)). This corresponds to an orbital level spacing

$$\Delta_o = \pi \hbar v_F / \ell \quad (1)$$

which is typically in the THz range, whereas the cavity frequency  $\nu_0$  is typically of the order of 10 GHz. Resonant effects between microwave cavity photons and this local

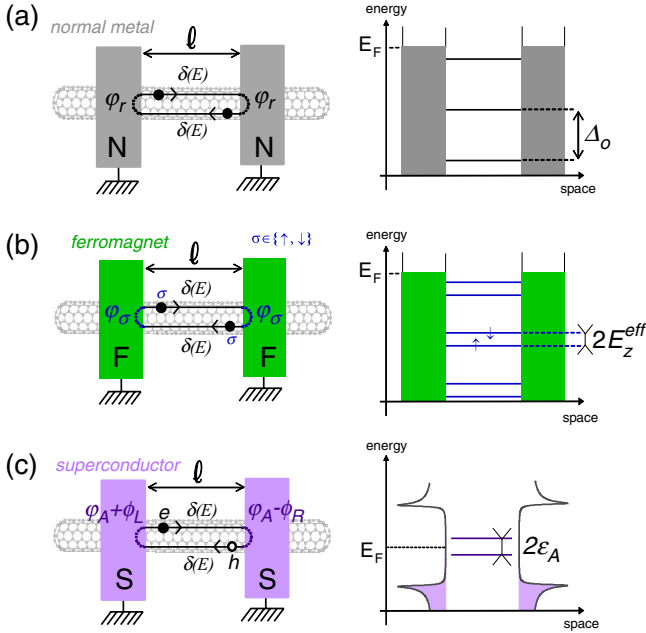


**Figure 2.** Hybrid quantum dot circuits (left panels) and the corresponding energy spectra (right panels) (a) case of a quantum dot formed by a portion with length  $\ell$  of nanoconductor (here a carbon nanotube) delimited by normal metal reservoirs (in gray). The separation between the orbital levels in the dot is  $\Delta_o = \pi \hbar v_F / \ell$  (b) case of ferromagnetic reservoirs. The dot levels have an effective Zeeman spin splitting  $2E_z^{\text{eff}} = (\varphi_{\uparrow} - \varphi_{\downarrow}) \hbar v_F / \ell$  because electrons with spin  $\sigma$  have a spin dependent reflection phase  $\varphi_{\sigma}$  on the ferromagnetic reservoirs (c) case of superconducting reservoirs with superconducting phases  $\phi_L$  and  $\phi_R$ . Electrons and holes are reflected on the left (right) superconductor with phases  $\varphi_A + \phi_{L(R)}$  and  $\varphi_A - \phi_{L(R)}$  respectively, where  $\varphi_A$  is the Andreev phase. This leads to the appearance of a twofold degenerate low energy Andreev doublet with a splitting  $2\varepsilon_A = 2\Delta \cos((\phi_R - \phi_L)/2)$  in the DOS of the nanoconductor.

orbital degree of freedom are therefore impossible. However, there exist other configurations more favorable to reaching the resonant regime, as we will see below.

Ferromagnetic materials are widely used to control spin transport in industrial spintronics devices [69]. They also represent a promising resource for coherent nanocircuits. If a quantum dot is delimited by ferromagnetic contacts, the reflection phases on its boundaries can become spin-dependent, because the Stoner exchange fields inside the ferromagnets provide a spin dependent confinement potential for electrons in the dot [70] (see figure 2(b)). Hence, an effective Zeeman splitting

$$2E_z^{\text{eff}} = (\varphi_{\uparrow} - \varphi_{\downarrow}) \hbar v_F / \ell \quad (2)$$

occurs inside the dot. The factor  $\ell^{-1}$  in the above equation occurs because  $E_z^{\text{eff}}$  is an interference effect between the two contacts, given by the resonance condition  $2\delta(E) + 2\varphi_{r,\sigma} = 2\pi n$ , for spin  $\sigma \in \{\uparrow, \downarrow\}$ . Due to this factor,  $E_z^{\text{eff}}$  can reach values of the order of  $2 \text{ T} \sim 56 \text{ GHz}$  for small dots with  $g \sim 2$  ( $\ell \sim 500 \text{ nm}$ ) [8]. In principle, this value is larger than stray fields from standard ferromagnets, which are independent of  $\ell$  and typically reach a few 100 mT. Furthermore, the effective field of equation (2) presents the advantage of being local, which can be useful in building complex devices.

Another interesting possibility to modify the spectrum of a nanocircuit is to use superconducting contacts which produce the Andreev reflection of an electron quasiparticle into a hole quasiparticle and vice versa (see figure 2(c)). For simplicity, we will consider the case where only the value of the superconducting gap changes at the superconductor/nanoconductor interface, from  $\Delta$  to 0, in a single channel model. In this case, the resonant condition between the two contacts is  $2\delta(E) + 2\varphi_A \pm (\phi_R - \phi_L) = 2\pi n$ , with  $\varphi_A = -\arccos(E/\Delta)$  the Andreev phase and  $\phi_{L(R)}$  the phase of the superconducting order parameter in the left(right) contact. Therefore, in the limit  $\Delta \ll \Delta_o$ , the interferences between electron and holes lead to the creation of an Andreev doublet at energies  $\pm\varepsilon_A$  with

$$\varepsilon_A = \Delta \cos\left(\frac{\phi_R - \phi_L}{2}\right). \quad (3)$$

One has, for instance,  $\Delta \sim 42 \text{ GHz}$  for aluminium electrodes. Hence, the scale  $\varepsilon_A$  can become very close to the cavity frequency  $\omega_0$  if the superconductor/quantum dot/superconductor junction is inserted inside a flux biased superconducting loop in order to obtain  $\phi_R - \phi_L < \pi$ . Note that the Andreev doublet discussed above has a two-fold degeneracy, since it can be produced by spin  $\uparrow$  electrons and spin  $\downarrow$  holes as well as spin  $\downarrow$  electrons and spin  $\uparrow$  holes. Such a degeneracy has to be taken into account in predicting the microwave response of superconducting nanostructures, as we will see in section 4.4. In summary, ferromagnetic and superconducting contacts offer interesting possibilities to make the spin or the electron/hole energy scales of a single quantum dot comparable to the cavity frequency. In contrast, the local charge degree of freedom associated to the scale  $\Delta_0$  is expected to be off resonant. Note that there can be a local orbital degeneracy related to the atomic structure of the nanoconductor, such as the K/K' degree of freedom in a carbon nanotube. Effects related to this type of degree of freedom will be evoked in section 4.3.3.

Above, we have discussed exclusively the spectrum of a single quantum dot delimited by fermionic contacts, in order to find intradot degrees of freedom which could be coupled resonantly to the cavity. However, we will see in the coming sections that non-local charge degrees of freedom associated to tunneling processes also play a major role in mesoscopic QED. First, there can be tunneling between two dots separated by a tunnel barrier with a hopping constant  $t$  (see figure 14). This strongly affects the spectrum of a double quantum dot, where bonding and anti-bonding states appear. In practice,  $t \sim \omega_0$  can be obtained with many different types of nanoconductors. Second, electrons can tunnel between a quantum dot and a metallic reservoir with a tunnel rate  $\Gamma$  that can also be of the order of  $\omega_0$ . These two types of resonance can lead to interesting effects, as we will see below.

### 3. Theory of light–matter interaction in mesoscopic QED devices

#### 3.1. The mesoscopic QED Hamiltonian

**3.1.1. Comparison between the different types of cavity QED experiments.** It is instructive to make a comparison of the

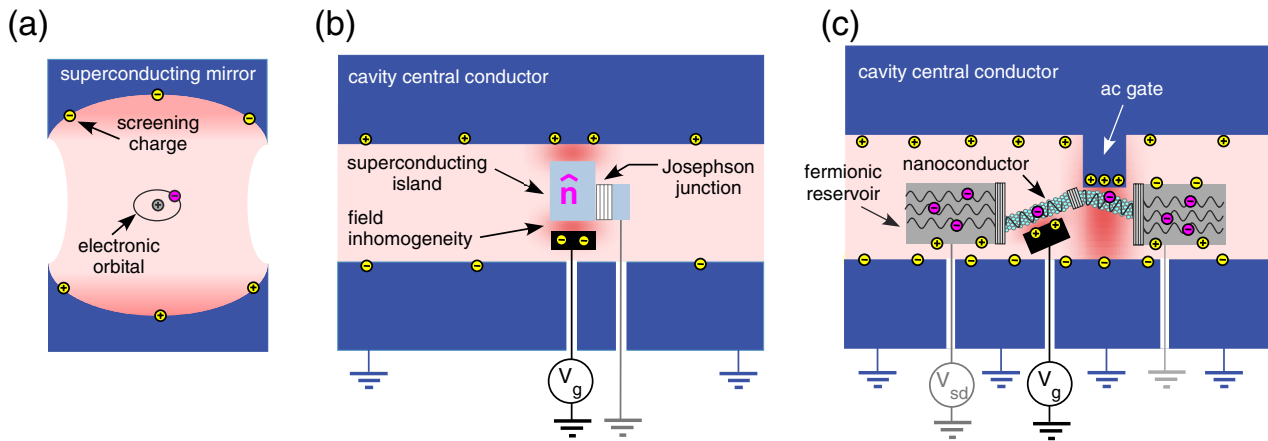


**Figure 3.** Schematic representation of the different types of cavity QED experiments. (a) Cavity QED experiment with an atom (b) circuit QED experiment with a charge superconducting quantum bit (c) Mesoscopic QED experiment with a hybrid nanocircuit. Cavity conductors are represented in blue and dc electrostatic gates in black. The photonic field is represented in pink, with inhomogeneities in dark pink. Electronic charges occupying orbitals of the flying atom in (a), or tunneling between quasi-localized orbitals of the nanocircuit in (c), are represented in fuchsia. Plasmonic screening charges on the metallic elements are represented in yellow.

physical ingredients involved in cavity, circuit and mesoscopic QED to identify the specificities of the light–nanocircuit interaction. Cavity QED focuses on the interactions between electrons in the atomic orbitals of a flying atom and the photons trapped inside a superconducting mirror cavity (see figure 3(a)). In these experiments, the effect of the cavity magnetic field on the atom can be disregarded for weak microwave amplitudes [75]. In most situations, one can consider that the cavity electric field is constant at the scale of the atom, because the atom is very small in comparison with the cavity. In this case, the light–matter interaction can be expressed quantum mechanically as  $\hat{H}_d = \vec{E}_0 \cdot \vec{d}$ , with  $\vec{E}_0$  being the quantized cavity electric field and  $\vec{d} = \sum_i q_i \vec{r}_i$  the dipole associated to the atomic charges  $q_i$  at position  $\vec{r}_i$ . Note that this charge distribution includes not only electrons but also the ions of the atomic nucleus. However, the explicit description of these ions essentially grants the electroneutrality condition  $\sum_i q_i = 0$ , which simplifies calculations. Cavity QED mainly focuses on electronic transitions between the atomic orbitals, induced by the cavity electric field.

In circuit QED, the concept of orbital degree of freedom is no longer relevant, because only macroscopic collective degrees of freedom matter, due to the rigidity of the superconducting phase. For instance, in a Cooper pair box, which is a small superconducting island coupled to a superconducting reservoir through a Josephson junction, only the total excess number  $\hat{n}$  of electrons on the island matters (see figure 3(b)). A second important difference from atomic cavity QED is that the cavity field cannot be considered as homogeneous on the scale of the superconducting quantum bit. Indeed, its spatial profile is strongly modified by the presence of the superconducting elements which tend to expel it. Figure 3(b) illustrates this situation in the case of a Cooper pair box embedded in a coplanar microwave cavity. The cavity electric field concentrates in capacitive areas between neighboring metallic elements, as represented by the darker pink areas. This capacitive coupling scheme is often described with a lumped element

circuit model which discretizes the device into nodes with uniform photonic potential and superconducting phase, connected by capacitors, inductors or Josephson junctions. In the simplest picture, the cavity is modeled as a distributed (L,C) line, and the superconducting island in figure 3(b) corresponds to a single node contacted through capacitors and a Josephson junction to the rest of the circuit (see figure 2 of [76]). The cavity electric field shifts the island potential due to the presence of the capacitive coupling between the dot island and the cavity central conductor. Recently, more sophisticated lumped element circuit models have been introduced for a more realistic description of circuit QED devices [77, 78]. Note that Josephson circuits with superconducting loops may equally couple to the cavity magnetic field (not represented in figure 3(b)).

Mesoscopic QED represents an intermediate situation between cavity and circuit QED (see figure 3(c)). Indeed, due to the existence of small confined nanoconductor areas (like for instance quantum dots), there exist discrete electronic orbital levels which recall the atomic orbitals of cavity QED. However, the cavity field is strongly inhomogeneous on the scale of the nanocircuit, which rather recalls circuit QED. For instance, one can use ac gates often connected directly (see figure 3(c)) or sometimes capacitively (see figure 1) to the cavity central conductor to reinforce locally the coupling between the cavity electric field and the electrons in one small part of the nanocircuit. The area between the ac gate and the nanoconductor in figure 3(c) concentrates the electric field, as represented by the darker pink shade. This provides a capacitive coupling between the cavity central conductor and the nanoconductor. Field screening effects represent another source of field inhomogeneity. First, the cavity fields are confined between the superconducting cavity conductors, represented in blue in figure 3(c). This effect naturally goes together with a screening of the fields inside the cavity conductors. Second, the fermionic reservoirs in the nanocircuit can at least partially screen the cavity fields. These screening effects are due to electronic plasmonic modes, which are

only implicitly taken into account in the usual descriptions of circuit QED, through current conservation. In mesoscopic QED, it is not *a priori* obvious to take into account plasmonic modes because one must take into account that fermionic reservoirs simultaneously host plasmonic modes *and* fermionic quasiparticle modes which cause quantum transport effects in the nanocircuit. These quasiparticle modes are coupled to the localized discrete electronic orbitals inside the nanoconductors through tunnel junctions. Tunneling is also at the heart of the Josephson coupling in superconducting circuits. However, tunneling from a normal metal reservoir involves the numerous quasiparticle modes in a reservoir on top of the nanoconductor levels. Therefore, the study of mesoscopic QED devices requires a description which combines physical ingredients from both cavity and circuit QED. In the following, we will follow the approach proposed by [80].

**3.1.2. Effective decomposition of a mesoscopic QED device.** In order to take into account both quasiparticle tunneling and plasmonic screening in a minimal way, one can assume that the plasmonic screening charges on the cavity conductors or fermionic reservoirs have a frequency which is much higher than all the other relevant frequencies in the device. In particular, we assume that the plasmonic frequency is much higher than the tunnel rate between a reservoir and a nanoconductor, or than the tunnel hopping constant between two dots. Under this assumption, one can decompose the nanocircuit of figure 4(a) heuristically into two parts: an effective orbital nanocircuit represented in black in figures 4(b) and (d), in which tunneling physics prevails, and an effective plasmonic circuit made out of perfect conductors, represented in blue in figures 4(b) and (d). Below, we discuss this decomposition in more detail.

In the black circuit of figure 4(d), the electronic orbital levels in the various circuit elements are connected through tunnel junctions (striped rectangles). In order to allow current conservation, the ‘orbital’ reservoirs have to be connected to the black voltage source and the ground, through wirings which necessarily host plasmonic modes. However, one can assume that these plasmonic modes do not have a significant influence on the value of the cavity field near the nanocircuit. The role of the black voltage source in figure 4(b) is essentially to ensure that the electronic levels in the nearby reservoir are filled up to the Fermi level plus a shift caused by the applied bias voltage.

The blue circuit of figure 4(c) is electrically disconnected from the black circuit. It represents the physical host of the screening charges which propagate together with the cavity photons. Some of these blue conductors directly correspond to the cavity central conductor and ground planes, or to the nanocircuit dc gates. The other conductors correspond to the nanocircuit reservoirs, and account at least qualitatively for the local screening of the cavity field in these reservoirs. This produces a renormalization of the cavity field, which can affect the coupling between the cavity photons and the quasiparticles in the black orbital circuit. Importantly, the blue conductors are connected to dc sources, drain, and gate voltage sources, similarly to the initial circuit of figure 4(a). This enables one to make a complete description of the cavity fields, including dc field contributions (this description

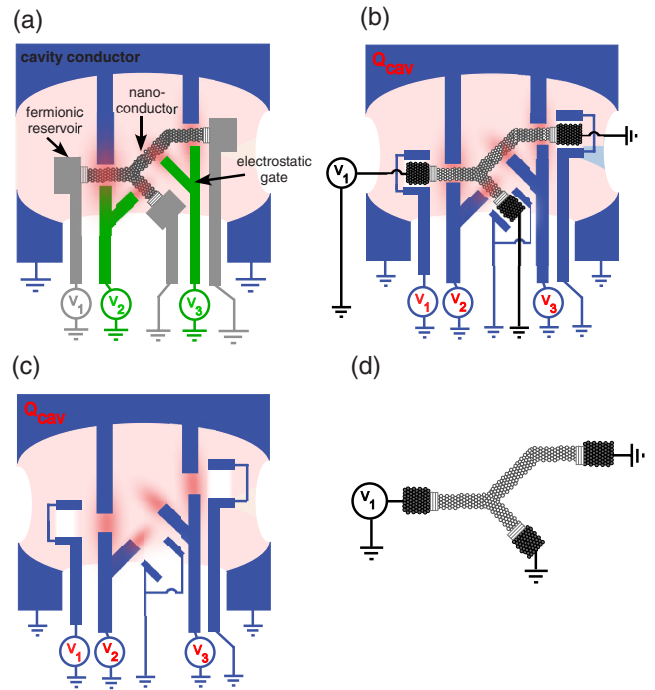


**Figure 4.** (a) Schematic representation of a hybrid circuit QED device which includes a nanoconductor, fermionic reservoirs and electrostatic gates. (b) Heuristic decomposition of the device into an effective plasmonic circuit in blue, and an effective quasiparticle nanocircuit in black. (c) Separate representation of the effective plasmonic circuit. The blue perfect conductors host the plasmons which propagate together with the photonic modes. The photonic field outside the blue conductors (in pink) is inhomogeneous, as represented by darker pink areas near the ac gates, and white areas between the small blue conductors. (d) Separate representation of the effective orbital nanocircuit which hosts electronic quasiparticle modes. The quasiparticles can tunnel through the barriers represented by the striped rectangles. Adapted figure with permission from [80], Copyright (2015) by the American Physical Society.

will be implemented mathematically in section 3.1.3). Note that when a tunneling event occurs in the nanocircuit, displacement currents occur in order to effect the reorganization of the screening charges throughout the whole mesoscopic QED device. In the model of figure 4(b), these displacement currents are also carried by the blue plasmonic circuit. Importantly, the model of figure 4(b), which separates physically the plasmonic and fermionic modes of the nanocircuit, is only an effective model which we will use in next section to justify the form of the mesoscopic QED Hamiltonian. In practice, the plasmonic modes and tunneling quasiparticles are of course not spatially separated. To calculate in a realistic way how the spatial profile of the cavity field is renormalized by the screening charges of the nanocircuit, one should use microwave simulation software (which disregards tunneling physics). On the basis of the heuristic model discussed above, we will introduce in the next section a description of mesoscopic QED in which plasmons are not described explicitly. This approach is allowed by the large separation in the characteristic timescales associated with plasmons and tunneling.

**3.1.3. Hodge decomposition of the electromagnetic field.** In order to exploit the effective model of figure 4(b), we will

first quantize the electromagnetic field outside the blue perfect conductors. Ultrafast plasmonic modes on these conductors will not be treated explicitly but included through boundary conditions on the blue conductors. These boundary conditions, which are disregarded in most descriptions of cavity QED, make the quantization of the electromagnetic field non-trivial. Some of the blue conductors are biased with a voltage  $V_i$ , such as for instance the electrostatic gates which are used to tune the positions of the energy levels in the nanocircuit. Some others are left floating with a constant charge  $Q_i$ , such as the central conductor of a coplanar waveguide cavity. To take this into account, we will decompose the total electric field  $\vec{E}(\vec{r}, t)$  outside the blue conductors into a longitudinal component  $\vec{E}_{\parallel}(\vec{r}, t)$ , which has a finite gradient but no rotational, a transverse component  $\vec{E}_{\perp}(\vec{r}, t)$ , which has a finite rotational but no gradient, and a harmonic component  $\vec{E}_{\text{harm}}(\vec{r})$ , which has none, such that:

$$\vec{E}(\vec{r}, t) = \vec{E}_{\perp}(\vec{r}, t) + \vec{E}_{\parallel}(\vec{r}, t) + \vec{E}_{\text{harm}}(\vec{r}). \quad (4)$$

Then, it is very convenient to use the Coulomb gauge, defined by  $\vec{\nabla}_{\vec{r}} \cdot \vec{A}(\vec{r}, t) = 0$ . In this case, both the magnetic field in the system and the transverse electric field can be expressed in terms of the vector potential as

$$\vec{E}_{\perp}(\vec{r}, t) = -\partial \vec{A}(\vec{r}, t) / \partial t \quad (5)$$

and

$$\vec{B} = \vec{\nabla}_{\vec{r}} \wedge \vec{A}(\vec{r}, t). \quad (6)$$

We now define scalar potentials  $U_{\parallel}$  and  $\Phi_{\text{harm}}$  from the equations

$$\vec{E}_{\parallel}(\vec{r}, t) = -\vec{\nabla}_{\vec{r}} U_{\parallel}(\vec{r}, t) \quad (7)$$

and

$$\vec{E}_{\text{harm}}(\vec{r}) = -\vec{\nabla} \cdot \Phi_{\text{harm}}(\vec{r}). \quad (8)$$

By combining the Maxwell equations with equations (4-8), one finds that  $\Phi_{\text{harm}}(\vec{r})$ ,  $U_{\parallel}(\vec{r}, t)$  and  $\vec{A}(\vec{r}, t)$  are set by separate equations. First,  $\Phi_{\text{harm}}$  is a static field set by the boundary conditions on the blue perfect conductors. More precisely, it fulfills the Poisson equation

$$\Delta_{\vec{r}} \Phi_{\text{harm}}(\vec{r}) = 0 \quad (9)$$

with boundary conditions corresponding to having charges  $Q_i$  or voltages  $V_i$  on the blue conductors (see [80] for details). Second, the potential  $U_{\parallel}$  is instantaneously set by the charge distribution  $\{e_{\alpha}, \vec{q}_{\alpha}\}$  in the black nanocircuit, i.e.

$$U_{\parallel}(\vec{r}, t) = \sum_{\alpha} e_{\alpha} G(\vec{r}, \vec{q}_{\alpha}). \quad (10)$$

The function  $G$  above is the solution of the Poisson equation  $\Delta_{\vec{r}} G(\vec{r}, \vec{r}') = -\delta(\vec{r} - \vec{r}') / \epsilon_0$  with boundary conditions  $Q_i = 0$  and  $V_i = 0$  on the blue conductors. In other words,  $G(\vec{r}, \vec{r}')$  describes the electrostatic interaction between two charges at points  $\vec{r}$  and  $\vec{r}'$ , renormalized by the screening charges on the blue conductors. Finally,  $\vec{A}$  follows the propagation equation

$$\left( \Delta_{\vec{r}} - \frac{1}{c^2} \frac{\partial^2}{\partial t^2} \right) \vec{A}(\vec{r}, t) = -\mu_0 \vec{j}_{\perp}(\vec{r}, t) \quad (11)$$

with the same boundary conditions as equation (10). One can conclude that  $\vec{A}$  corresponds to the photonic field which can be quantized. Interestingly, this picture is similar to the picture used for cavity QED, up to two differences. First, in cavity QED, the harmonic potential is generally omitted because the boundary conditions on the cavity conductors are not explicitly treated [79]. Second, in the simplest descriptions of cavity QED, the longitudinal potential  $U_{\parallel}$  corresponds to the potential caused by the atom in vacuum [75], i.e.  $U_{\parallel}(\vec{r}, t) = \sum_{\alpha} e_{\alpha} / 4\pi\epsilon_0 |\vec{r} - \vec{q}_{\alpha}|$ . In the case of mesoscopic QED, this potential is dressed by the screening charges on the blue conductors. This effect is taken into account by the  $G$  function in equation (10).

**3.1.4. Minimal coupling Hamiltonian.** From the above section, the independent degrees of freedom in the mesoscopic QED device are the value of the cavity potential  $\vec{A}$ , and the position  $\vec{q}_{\alpha}$  of the charges  $e_{\alpha}$  in the black nanocircuit. In principle, the charge distribution  $\{e_{\alpha}, \vec{q}_{\alpha}\}$  includes the crystalline background  $\mathbf{C}$  and electrons from the valence bands  $\mathbf{V}$  of the black nanocircuit. However, assuming that these charges are off resonant with the cavity, one can describe them with the mean field approximation. This requires taking into account that conduction electrons feel a confinement potential  $V_{\text{conf}}(\vec{r}) = \langle \sum_{\alpha \in \mathbf{C}, \mathbf{V}} e_{\alpha} G(\vec{r}_{\alpha}, \vec{q}_{\alpha}) \rangle$ , with  $\langle \rangle$  a statistical average on the state of the charges of  $\mathbf{C}$  and  $\mathbf{V}$ . This potential accounts for the transverse confinement of the conduction electrons inside the nanocircuit, and the tunnel barriers between the different nanocircuit elements. Then, by using a quantization procedure analogous to that used in cavity QED, one can express the mesoscopic QED Hamiltonian as (see [80] for details):

$$\hat{H}_{\text{tot}} = \int d^3 r \hat{\psi}^{\dagger}(\vec{r}) \hat{h}_{\rho}(\vec{r}) \hat{\psi}(\vec{r}) + \hat{H}_{\text{Coul}} + \omega_0 \hat{a}^{\dagger} \hat{a} + \int d^3 r \left( \Delta(\vec{r}) e^{2\Phi(\vec{r})} \hat{\psi}_{\uparrow}^{\dagger}(\vec{r}) \hat{\psi}_{\downarrow}^{\dagger}(\vec{r}) + \text{H.c.} \right) \quad (12)$$

with

$$\hat{h}_{\rho}(\vec{r}) = \frac{1}{2m} \left( \frac{\vec{\nabla}_{\vec{r}}}{i} + e \vec{A}(\vec{r}) \right)^2 - e \Phi_{\text{harm}}(\vec{r}) - e V_{\text{conf}}(\vec{r}), \quad (13)$$

$$\hat{H}_{\text{Coul}} = \frac{e^2}{2} \int d^3 r d^3 r' \hat{\psi}^{\dagger}(\vec{r}) \hat{\psi}^{\dagger}(\vec{r}') G(\vec{r}, \vec{r}') \hat{\psi}(\vec{r}') \hat{\psi}(\vec{r}), \quad (14)$$

and

$$\vec{A}(\vec{r}) = \vec{A}(\vec{r}) i(\hat{a} - \hat{a}^{\dagger}). \quad (15)$$

We have introduced above the field operator  $\hat{\psi}^{\dagger}(\vec{r}) = (\hat{\psi}_{\uparrow}^{\dagger}(\vec{r}), \hat{\psi}_{\downarrow}^{\dagger}(\vec{r}))$  associated with the creation of conduction electrons in the black nanocircuit. The potential  $V_{\text{conf}}(\vec{r})$  can be treated on the same footing as the harmonic potential  $\Phi_{\text{harm}}(\vec{r})$ . The term  $\hat{H}_{\text{Coul}}$  describes Coulomb interactions

between electrons. This term depends on the function  $G$  because Coulomb interactions between the charges  $\alpha$  of the black nanocircuit are renormalized by the screening charges on the blue conductors. In equation (13), the vector potential  $\vec{A}(\vec{r})$  ensures the gauge invariance of the single electron term. For simplicity, equation (15) expresses  $\vec{A}(\vec{r})$  by using only one cavity mode, corresponding to the creation operator  $\hat{a}$ , but equations (12)-(15) can be generalized straightforwardly to the multimode case, either to take into account several cavity modes or to describe the cavity bare linewidth with a bosonic bath. The second line of equation (12) is a pairing term which describes superconducting correlations in the nanocircuit. This term must include a phase factor  $\Phi(\vec{r})$  which depends on the photonic operators, in order to ensure the gauge invariance of the Hamiltonian (see next section for details).

**3.15. Photonic pseudo-potential picture.** Different types of light-matter interaction appear in Hamiltonian (12). Indeed, equation (13) contains a linear term in  $\vec{\nabla}_{\vec{r}} \cdot \vec{A}(\vec{r})$  and a non-linear term in  $\hat{A}^2$ . It also contains the exponential of the phase factor  $\Phi(\vec{r})$  which is non-linear. The effect of the non-linear terms is not negligible, in principle (see appendix B of [80] for details). Therefore, in this section, we introduce a unitary transformation of the Hamiltonian  $\hat{H}_{\text{tot}}$  which simplifies the form of the light-matter interaction. For simplicity, we consider nanocircuits with standard dimensions and without loops, so that one can disregard magnetic effects induced by the photons. This means that one can use  $\vec{\nabla}_{\vec{r}} \wedge \vec{A} \simeq 0$  on the scale of the whole nanocircuit. This assumption is valid for all the mesoscopic QED devices studied experimentally so far, except [35]. The more general case will be discussed elsewhere. When  $\vec{\nabla}_{\vec{r}} \wedge \vec{A} \simeq 0$  it is possible to define a photonic pseudo-potential  $V_{\perp}(\vec{r})$  such that

$$\vec{\nabla}_{\vec{r}} \cdot V_{\perp}(\vec{r}) \simeq \omega_0 \vec{A}(\vec{r}) \quad (16)$$

and

$$\hat{\Phi}(\vec{r}) = e(\hat{a} - \hat{a}^{\dagger})V_{\perp}(\vec{r})/\omega_0. \quad (17)$$

Then, one can apply to Hamiltonian (12) the unitary transformation  $\tilde{H}_{\text{tot}} = \mathcal{U}^{\dagger} \hat{H}_{\text{tot}} \mathcal{U}$  with

$$\mathcal{U} = \exp\left(\frac{(\hat{a}^{\dagger} - \hat{a})\hat{\Psi}}{\omega_0}\right) \quad (18)$$

and

$$\hat{\Psi} = -e \int d^3r V_{\perp}(\vec{r}) \hat{\psi}^{\dagger}(\vec{r}) \hat{\psi}(\vec{r}). \quad (19)$$

This leads to the Hamiltonian

$$\tilde{H}_{\text{tot}} = H_0 + \hat{\Psi}(\hat{a} + \hat{a}^{\dagger}) + \omega_0 \hat{a}^{\dagger} \hat{a} \quad (20)$$

with

$$H_0 = \int d^3r \hat{\psi}^{\dagger}(\vec{r}) \tilde{h}_{\rho}(\vec{r}) \hat{\psi}(\vec{r}) + \hat{H}_{\text{Coul}} + (\hat{\Psi}^2/\omega_0) + \int d^3r \left( \Delta(\vec{r}) \hat{\psi}_{\uparrow}^{\dagger}(\vec{r}) \hat{\psi}_{\downarrow}^{\dagger}(\vec{r}) + \text{H.c.} \right) \quad (21)$$

and

$$\tilde{h}_{\rho}(\vec{r}) = -\Delta_{\vec{r}}/2m - e\Phi_{\text{harm}}(\vec{r}) - eV_{\text{conf}}(\vec{r}). \quad (22)$$

In the Hamiltonian of equation (20), the light-matter interaction is greatly simplified since it involves a single linear term in  $\hat{\Psi}(\hat{a} + \hat{a}^{\dagger})$ . Interestingly, this Hamiltonian bridges between cavity QED and circuit QED. Indeed, the dipolar electric approximation of cavity QED corresponds to a photonic potential which evolves linearly in space i.e.  $V_{\perp}(\vec{r}) = \vec{E}_0 \cdot \vec{r}$ , whereas circuit QED corresponds to a constant photonic potential inside each node of the circuit model.

**3.16. Anderson-like Hamiltonian for mesoscopic QED.** Since tunneling physics is at the heart of quantum transport, it is useful to re-express Hamiltonian (20) to describe tunneling explicitly. For this purpose, one needs to decompose the field operator  $\hat{\psi}^{\dagger}(\vec{r})$  associated with quasiparticle modes of the black circuit on the ensemble of the creation operators  $\hat{c}_n^{\dagger}$  for electrons in an orbital  $n$  with energy  $\varepsilon_n$  of a given circuit element (reservoir, dot,...). At lowest order in tunneling, one can use  $\hat{\psi}^{\dagger}(\vec{r}) = \varphi_n^* \hat{c}_n^{\dagger}$  [81]. Then, Hamiltonian (20) directly gives

$$\hat{H}_{\text{tot}}^{\text{tun}} = \hat{H}_0^t + \hat{h}_{\text{int}}(\hat{a} + \hat{a}^{\dagger}) + \omega_0 \hat{a}^{\dagger} \hat{a} \quad (23)$$

with

$$\hat{H}_0^t = \sum_n \varepsilon_n \hat{c}_n^{\dagger} \hat{c}_n + \sum_{n \neq n'} (t_{n,n'} \hat{c}_n^{\dagger} \hat{c}_{n'} + \text{H.c.}) \quad (24)$$

$$\hat{h}_{\text{int}} = \sum_n g_n \hat{c}_n^{\dagger} \hat{c}_n + \sum_{n \neq n'} (\gamma_{n,n'} \hat{c}_n^{\dagger} \hat{c}_{n'} + \text{H.c.}). \quad (25)$$

$$g_n = -e \int d^3r |\varphi_n(\vec{r})|^2 V_{\perp}(\vec{r}). \quad (26)$$

and

$$\gamma_{n',n} = -e \int d^3r \varphi_n^*(\vec{r}) \varphi_{n'}(\vec{r}) V_{\perp}(\vec{r}). \quad (27)$$

Above,  $\hat{H}_0^t$  is the Anderson-like Hamiltonian of the nanocircuit, with  $t_{n,n'}$  the tunnel coupling between orbitals  $n$  and  $n'$ , which is finite only if  $n$  and  $n'$  correspond to two orbitals in two different circuit elements coupled through a tunnel junction. The term  $\hat{h}_{\text{int}}(\hat{a} + \hat{a}^{\dagger})$  describes the interaction of the nanocircuit with the cavity. Cavity photons can have different effects. First, they can shift the energy of orbital  $n$  due to the term in  $g_n$ . In the limit where  $V_{\perp}(\vec{r})$  can be considered as constant inside a given circuit element,  $g_n$  can be considered to be the same for all the orbitals of this element (at zeroth order in tunneling). In this limit, the coupling of the cavity to the element can be seen as a capacitive coupling due to the finite capacitance between this element and the cavity central conductor. This recalls the case of a superconducting charge quantum bit in circuit QED, where the qubit island potential is modulated due to the capacitive coupling between the island and the cavity. In principle, cavity photons can also produce a direct coupling between two different orbitals of

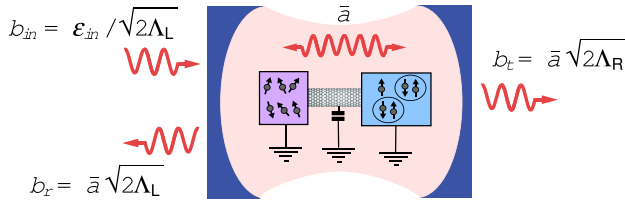


**Figure 5.** Representation of the input–output relations of circuit QED in the semiclassical limit.

the nanocircuit, due to the term in  $\gamma_{n',n}$ . This corresponds to two physically different situations. First, there can be photo-induced transition terms between two different orbitals of the same circuit element, which recalls the orbital transitions inside an atom, which are used in cavity QED. Second, there can also be a photo-induced tunneling term between two different circuit elements. Nevertheless, the terms  $\gamma_{n',n}$  are expected to be weak because  $\varphi_n(\vec{r})$  and  $\varphi_{n'}(\vec{r})$  have a small matrix element in the tunnel theory.

In this review, we will mainly discuss the effects of the  $g_n$  elements which are expected to be dominant in most mesoscopic QED devices, and have been sufficient so far to interpret experiments. For standard coplanar cavities similar to that of [26], the pseudo photonic potential  $V_{\perp}(\vec{r})$  typically varies by  $V_{\text{rms}} \simeq 1 \mu\text{eV} = 240 \text{ MHz}$  from the cavity central conductor to the ground plane, across a spatial gap of  $5 \mu\text{m}$ . From one nanocircuit site to another,  $V_{\perp}(\vec{r})$  can vary by a significant fraction of  $V_{\text{rms}}$ , especially if ac gates are fabricated to concentrate the cavity voltage drop between these sites. Consequently, the value of  $g_n$  can strongly depend on the orbital  $n$  considered. Even for a given quantum dot, the value of  $g_n$  can vary strongly from one orbital to the other due to variations in the spatial profile of  $\varphi_n(\vec{r})$ . For instance, in a single quantum dot with multiple gates made in a carbon nanotube,  $g_n/2\pi$  was found to vary from 55 MHz to 120 MHz [37]. This could mean that  $V_{\perp}(\vec{r})$  cannot be considered as homogeneous on the scale of this dot.

### 3.2. Semiclassical cavity response in the linear coupling regime

#### 3.2.1. Expression of the cavity photon amplitude.

So far, in mesoscopic QED, most experiments have focused on the modification of the cavity microwave transmission or reflection due to the presence of the nanocircuit. To describe such a measurement, one can use the general Hamiltonian

$$\hat{H} = \hat{H}_0 + \hat{h}_{\text{int}}(\hat{a} + \hat{a}^{\dagger}) + \omega_0 \hat{a}^{\dagger} \hat{a} + H_{\text{diss}} + i\hat{a}^{\dagger} \varepsilon_{\text{in}} e^{-i\omega_{\text{RF}} t} - i\hat{a} \varepsilon_{\text{in}}^* e^{i\omega_{\text{RF}} t}, \quad (28)$$

which is a generalization of equation (23). Above, we describe cavity dissipation with a bosonic bath

$$H_{\text{diss}} = \int d\epsilon \eta \left( \omega_{\epsilon} \hat{b}_{\epsilon}^{\dagger} \hat{b}_{\epsilon} + \beta \hat{b}_{\epsilon}^{\dagger} \hat{a} + \beta^* \hat{a}^{\dagger} \hat{b}_{\epsilon} \right) \quad (29)$$

with  $\hat{b}_{\epsilon}^{\dagger}$  the creation operator for a bosonic mode at energy  $\epsilon$ , and  $\eta$  the density of modes. For simplicity, we assume that the coupling constant  $\beta$  between the cavity and the bath is

energy-independent. This term was not included in equation (23), but it can be added by generalizing equations (15) and (18)<sup>3,4</sup>. We also use a drive term with amplitude  $\varepsilon_{\text{in}}$  which describes the effect of the continuous microwave tone which is injected at the input of the cavity. Following the discussion in section 3.1.6, we assume that the light–matter interaction is well approximated by

$$\hat{h}_{\text{int}} = \sum_n g_n \hat{c}_n^{\dagger} \hat{c}_n. \quad (30)$$

From equations (28) and (29), one has

$$\frac{d}{dt} \hat{a} = i[\hat{H}, \hat{a}] = -i\omega_0 \hat{a} - i\hat{h}_{\text{int}} - \varepsilon_{\text{in}} e^{-i\omega_{\text{RF}} t} - \Lambda_0 \hat{a} \quad (31)$$

with  $\Lambda_0 = \pi\eta |\beta|^2$  the cavity mode decay rate. Note that the full width at half maximum (FWHM) of the bare cavity transmission corresponds to the parameter  $\varkappa = 2\Lambda_0$  used in many studies. In most experiments performed so far, a large number of cavity photons has been used, i.e.  $\langle \hat{a}^{\dagger} \hat{a} \rangle > 10$ . In this case, it is sufficient to treat  $\hat{a}$  as a classical quantity i.e.  $\hat{a} \simeq \langle \hat{a} \rangle = a$ . In the case  $\omega_{\text{RF}} \simeq \omega_0$ , one can furthermore use the resonant approximation:

$$\langle \hat{a} \rangle \simeq \bar{a} e^{-i\omega_{\text{RF}} t}. \quad (32)$$

In the above,  $|\bar{a}|^2$  corresponds to the average cavity photon number  $\langle \hat{a}^{\dagger} \hat{a} \rangle$ . From the linear response theory one obtains

$$\begin{aligned} \langle \hat{c}_n^{\dagger} \hat{c}_n \rangle(t) &= p_n + \sum_{n'} g_{n'} \chi_{n,n'}(\omega_{\text{RF}}) \bar{a} e^{-i\omega_{\text{RF}} t} \\ &+ \sum_{n'} g_{n'} \chi_{n,n'}(-\omega_{\text{RF}}) \bar{a}^* e^{i\omega_{\text{RF}} t}. \end{aligned} \quad (33)$$

Here,  $\chi_{n,n'}(\omega_{\text{RF}})$  is by definition the charge susceptibility expressing how the occupation of level  $n$  responds at first order to a classical modulation of the energy of level  $n'$ , in stationary conditions. We denote by  $p_n$  the average occupation of state  $n$  for  $\hat{h}_{\text{int}} = 0$ . One has, in the framework of the linear response theory,

$$\chi_{n,n'}(t-t') = -i\theta(t) \left\langle \left[ \hat{c}_n^{\dagger}(t) \hat{c}_n(t), \hat{c}_{n'}^{\dagger}(t') \hat{c}_{n'}(t') \right] \right\rangle_{\hat{h}_{\text{int}}=0}, \quad (34)$$

<sup>3</sup> In principle, in the presence of a cavity bosonic bath, one has to include the dissipation term  $H_{\text{diss}}$  of equation (29) in the Hamiltonian (12). Then, in order to obtain the photonic pseudo-potential picture, it is still sufficient to use the transformation (18) if there is a very weak spatial overlap between the nanocircuit and the modes of the bosonic bath. The exact form for Hamiltonian (28) is then slightly more complicated than what is indicated in the main text, because the transformation of the term  $H_{\text{diss}}$  by (18) leads to an extra coupling term  $\int d\epsilon \eta \hat{V}(\beta \hat{b}_{\epsilon}^{\dagger} + \beta^* \hat{b}_{\epsilon}) / \omega_0$  between the electrons of the nanocircuit and the bosonic bath. One could expect an extra widening of the nanocircuit electronic levels by this term, with an order of magnitude  $\Lambda_0 (g_n / \omega_0)^2$ . However, in the experiments, one has  $g_n / \omega_0 \ll 1$  and  $\Lambda_0$  is very small in comparison with the intrinsic damping of the dot levels by for instance the metallic contacts. Therefore, equations (28) and (29) seem to be a good approximation for the description of cavity dissipation in the photonic pseudo-potential picture.

<sup>4</sup> The drive term in  $\varepsilon_{\text{in}}$  can be obtained by treating explicitly the classical part  $\langle \hat{b}_{\text{in}}^{\dagger} \rangle$  of the bosonic bath mode  $\hat{b}_{\text{in}}^{\dagger}$  excited by a microwave source.

where  $\langle \rangle_{\hat{h}_{\text{im}}=0}$  denotes the statistical averaging for  $g_n = 0$  for any  $n$ . Inserting equations (32) and (33) into equation (31), and keeping only resonant terms, one gets

$$\bar{a} = \frac{\varepsilon_{\text{in}}}{\omega_{\text{RF}} - \omega_0 + i\Lambda_0 - \Xi(\omega_{\text{RF}})} \quad (35)$$

with

$$\Xi(\omega_{\text{RF}}) = \sum_{n,n'} g_n g_{n'} \chi_{n,n'}(\omega_{\text{RF}}) \quad (36)$$

the global charge susceptibility of the nanocircuit. Note that in the general case the indices  $n, n'$  in equation (35) can belong to the nanoconductors as well as the fermionic reservoirs. From equation (35), the presence of the nanocircuit modifies the apparent frequency and linewidth of the cavity. For most of the experiments reported in the review, the cavity response is measured at  $\omega_{\text{RF}} = \omega_0$ . In the rest of this section, we will also assume that  $\Xi(\omega_0)$  can be considered as constant for  $\omega_0 - \Lambda_0 \lesssim \omega_{\text{RF}} \lesssim \omega_0 + \Lambda_0$ , which occurs for instance if the electronic relaxation rates in the nanocircuit are much larger than the photon relaxation rate  $\Lambda_0$ . In this case, the cavity frequency and linewidth shifts caused by the presence of the nanocircuit are, from equation (35),

$$\Delta\omega_0 = \text{Re}[\Xi(\omega_0)] \quad (37)$$

and

$$\Delta\Lambda_0 = -\text{Im}[\Xi(\omega_0)]. \quad (38)$$

Note that this type of measurement has been pioneered by works in which a coplanar waveguide resonator [82] or a lumped element resonator [83] was coupled to an array of  $10^5$  isolated mesoscopic rings. The resonator frequency and linewidth shifts revealed the global electric and magnetic response of the rings to the resonator field, at frequency  $\omega_0 \sim 350$  MHz. More recently, the admittance of a single double quantum dot was measured at frequencies  $\omega_0 < 400$  MHz by using a lumped element (L,C) resonator [20, 21]. One important advantage of the circuit QED architecture is the higher frequency of the cavity. One has typically  $\omega_0 \sim 5$  GHz, which is higher than the cryogenic temperatures obtained with a dilution fridge  $k_b T \simeq 25$  mK  $\simeq 0.5$  GHz. Therefore, the quantum regime with a low number of cavity photons is accessible. In this regime, the semiclassical approximation used in this section is no longer valid. However, understanding the semiclassical regime of mesoscopic QED is an important prerequisite to the realization of quantum experiments. Most experiments realized so far correspond to this regime and can be well understood with the semiclassical picture.

**3.2.2. Cavity signals from the input–output formalism.** Above, we have discussed how a nanocircuit induces modifications  $\Delta\omega_0$  and  $\Delta\Lambda_0$  of the cavity apparent frequency and linewidth. For a full description of a mesoscopic QED experiment, it is necessary to describe how one can measure these quantities. For that purpose, one has to take into account the existence of the input and output ports of the cavity, through which the cavity is excited and measured. These ports correspond to the pieces of waveguide connected capacitively to the cavity, on both sides of the cavity central conductor (see figure 1(a)). In

the semiclassical limit, the incident, transmitted and reflected photon fluxes in these ports can be characterized by complex amplitudes  $b_{\text{in}}$ ,  $b_t$  and  $b_r$ . We assume that the cavity is excited through its input port, which can be, for instance, the left port in figure 1. The transmission  $b_t/b_{\text{in}}$  of the cavity can be obtained experimentally by measuring the microwave amplitude  $b_t$  going out through the output port, which can be the right port in figure 1. In the semiclassical limit, the correspondence between the approach of section 3.2.1 and the input–output formalism of circuit QED [84] gives the relations of figure 5 between  $b_{\text{in}}$ ,  $b_{t(r)}$ ,  $\varepsilon_{\text{in}}$  and  $\bar{a}$  [37]. There,  $\Lambda_{L(R)}$  corresponds to the contribution of the left (right) port to the cavity linewidth, which implies  $\Lambda_L + \Lambda_R \leq \Lambda_0$ . From equation (35) and figure 5, the cavity microwave transmission can be expressed as

$$\frac{b_t}{b_{\text{in}}} = \frac{2\sqrt{\Lambda_L\Lambda_R}}{\omega_{\text{RF}} - \omega_0 + i\Lambda_0 - \Xi(\omega_{\text{RF}})}. \quad (39)$$

Hence, in the semiclassical linear limit, the cavity transmission amplitude is set by the charge susceptibility of the nanocircuit [36, 37, 48, 85, 133]. A similar result can be obtained for the cavity reflection amplitude. Note that above,  $b_t/b_{\text{in}}$  is expressed with the usual quantum mechanics convention for the definition of Fourier transforms, i.e.  $g(\omega) = \int_{-\infty}^{+\infty} dt g(t)e^{i\omega t}$ , which is used throughout this review. In order to interpret experiments, one has to take into account that microwave equipment uses the electrical engineering Fourier transform convention, which is complex conjugated to the former, so that  $(b_t/b_{\text{in}})^*$  is obtained experimentally.

In practice, the experimental signals which are directly measured are the transmission phase shift  $\Delta\varphi$  and amplitude shift  $\Delta A$  defined by

$$\frac{b_t}{b_{\text{in}}} = (A_0 + \Delta A)e^{i(\varphi_0 + \Delta\varphi)} \quad (40)$$

Using (37) and (38) valid for a poorly coherent nanocircuit, and assuming that  $\omega_{\text{RF}} = \omega_0$  and  $|\Delta\omega_0|, |\Delta\Lambda_0| \ll |\omega_0|, |\Lambda_0|$ , one finds that the cavity signals are directly related to the cavity parameters' shifts, i.e.

$$\Delta\varphi = \frac{\Delta\omega_0}{\Lambda_0} = \text{Re}[\Xi(\omega_0)] \frac{1}{\Lambda_0} \quad (41)$$

and

$$\Delta A = -\frac{\Delta\Lambda_0 A_0}{\Lambda_0} = \text{Im}[\Xi(\omega_0)] \frac{A_0}{\Lambda_0}, \quad (42)$$

so that  $\Delta\varphi$  and  $\Delta A$  correspond to the dispersive and dissipative parts of the signal. Beyond this limit, the experimental data can be understood by combining equations (39) and (40).

Depending on the regime of parameters fulfilled by the nanocircuit, and in particular the order of magnitude of the tunnel rates between the dots and reservoirs, different calculation techniques can be used to calculate  $\Xi(\omega_0)$ . We will discuss several possibilities in the coming sections. In this review, we will only consider cases where the summation on indices  $n$  and  $n'$  in equation (36) can be restricted to internal sites of the nanoconductor. This requires that the coupling between the cavity and the nanoconductor sites is much larger than the coupling

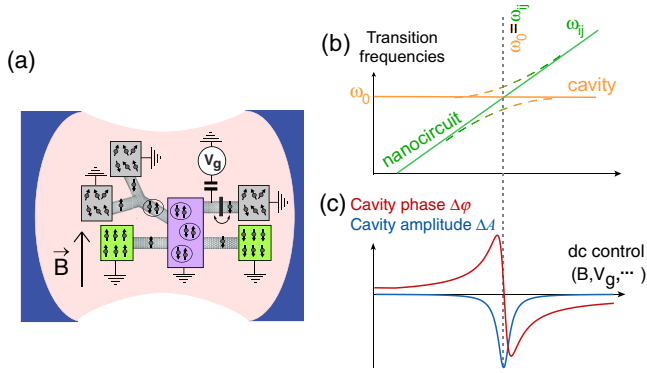


**Figure 6.** Principle of a cavity measurement at a constant frequency  $\omega_{\text{RF}} = \omega_0$ , in the presence of a nanocircuit with internal degrees of freedom, represented in panel (a). When the control parameters like a magnetic field  $B$  or a gate voltage  $V_g$ , are varied, a nanocircuit transition frequency can become resonant with the cavity as shown in panel (b). This gives variations of the cavity transmission phase and cavity transmission amplitude represented in panel (c).

between the cavity and the reservoirs. This is not obvious *a priori*, since the nanoconductor is much smaller than the reservoirs and thus tends to have a smaller capacitance towards the cavity resonator. However, this feature can be compensated by using for instance ac top gates which reinforce the coupling between the nanoconductor and the cavity. In this limit,  $\Xi(\omega_0)$  corresponds to the charge susceptibility of the nanoconductor at frequency  $\omega_0$ . In the opposite limit where the coupling between the cavity and the source/drain of the nanocircuit is dominant, it has been observed experimentally that the cavity signals essentially show replicas of the conductance signal [54].

## 4. Mesoscopic QED experiments in the artificial atom limit

### 4.1. Measuring the internal degrees of freedom of a nanocircuit with cavity photons

In this section, we consider a nanocircuit with a very small tunnel coupling to metallic reservoirs. Hence, the nanocircuit behaves as an artificial atom and a direct analogy with cavity or circuit QED experiments can be drawn. Assuming that the summation on index  $n$  in equation (30) can be restricted to sites which do not correspond to a reservoir, one gets

$$\Xi(\omega_{\text{RF}}) \simeq \sum_{ij} \frac{g_{ij}^2 (n_j - n_i)}{\omega_{\text{RF}} - \omega_{ij} + i\Gamma_{ij}}. \quad (43)$$

Above,  $\omega_{ij}$  is an internal transition frequency of the nanoconductor between states  $i$  and  $j$ ,  $\Gamma_{ij}$  is the decoherence rate associated to this transition, and  $n_i$  is the average occupation of state  $i$ . We will see later in a particular example how to derive this expression, which is valid for  $\Gamma_{ij} \ll k_B T$  and all transitions frequencies well separated (see section 4.2.2).

We now discuss a measurement of  $\Delta A$  and  $\Delta\varphi$  made with a constant cavity excitation frequency  $\omega_{\text{RF}} = \omega_0$ . In the absence of external dc bias voltages, one has necessarily  $\Delta A < 0$ , because the nanocircuit can only damp cavity photons. By combining equations (39), (40) and (43), one can see that the cavity signals are resonant for  $\omega_0 = \omega_{ij}$ . In a typical experiment, the

transition frequencies  $\omega_{ij}$  can be tuned with nanocircuit control parameters such as dc gate voltages or the external magnetic field. When these parameters are swept, the cavity signals provide a cut of the nanocircuit excitation spectrum at frequency  $\omega_0$ , as illustrated by figure 6. For well separated resonances,  $\Delta A$  presents a negative peak at  $\omega_0 = \omega_{ij}$  whereas  $\Delta\varphi$  presents a variation with a sign change at  $\omega_0 = \omega_{ij}$  (see figure 6(c)). Therefore, the excitation spectrum of the nanocircuit is more straightforwardly readable in the  $\Delta\Lambda_0$  signal, in principle.

For quantum information applications, the strong coupling regime between the nanocircuit and the cavity is intensively sought after. This regime corresponds to having one of the nanocircuit transitions  $i \leftrightarrow j$  such that  $g_{ij} > \Gamma_{ij}$ ,  $\Lambda_0$ . We will also assume below that the other nanocircuit transitions do not significantly affect the cavity. For the most simple characterization of the nanocircuit/cavity coupling, the nanocircuit is kept in its ground state ( $p_j = 1$ ,  $p_i = 0$ ). In these conditions, the cavity response is set by the charge susceptibility

$$\Xi(\omega_{\text{RF}}) \simeq \frac{g_t^2}{\omega_{\text{RF}} - \omega_{ij} + i\Gamma_2^*}, \quad (44)$$

with  $\Gamma_2^* = \Gamma_{ij}$  the decoherence rate of the resonant nanocircuit transition, and  $g_t$  its coupling to the cavity. In the strong coupling limit, the cavity resonance versus  $\omega_{\text{RF}}$  shows two peaks instead of the single peak of the weakly coupled regime, due to the strong hybridization of the cavity states with the nanocircuit states  $i$  and  $j$  (See figure 9(d)). This regime has already been reached, for instance with atomic cavity QED [86, 87], or isolated quantum dots in optical cavities [88, 89], or superconducting quantum bits coupled to microwave cavities [26]. It has also also been reached more recently in Mesoscopic QED, as will be discussed in section 4.2.3.

It is useful to define figures of merit to characterize the strength of a light/matter resonance. We first define the cooperativity

$$C_{e-\text{ph}} = g_t^2 / \Lambda_0 \Gamma_2^*. \quad (45)$$

From equation (39), in the resonant regime  $\omega_{ij} = \omega_0$ , this figure of merit indicates whether the cavity dissipation is dominated by the intrinsic cavity damping  $\Lambda_0$  ( $C_{e-\text{ph}} < 1$ ) or by the nanocircuit dissipation ( $C_{e-\text{ph}} > 1$ ). The cooperativity can also be used to express the lasing threshold  $C_{e-\text{ph}} \gtrsim 1/2$  to obtain a lasing effect with a single qubit in a cavity, in a situation where  $\omega_{ij} = \omega_0$ , and the qubit dephasing  $\Gamma_\varphi^*$  is much stronger than the qubit relaxation  $\Gamma_1$  ( $\Gamma_\varphi^* \gg \Gamma_1$  so that  $\Gamma_2^* = \Gamma_\varphi + (\Gamma_1/2) \simeq \Gamma_\varphi$ ) (see e.g. [158, 159]).

In the devices considered in the present review,  $\Lambda_0 \ll \Gamma_2^*$  is always fulfilled due to the high quality of the resonators used. In this context, the ratio<sup>5</sup>

$$Q_{e-\text{ph}} = \sqrt{1 + \sqrt{2} g_t / \Gamma_2^*} \quad (46)$$

is also instructive. For a resonant cavity/nanocircuit transition ( $\omega_{ij} = \omega_0$ ), and in the limit of a negligible bare cavity linewidth,

<sup>5</sup> To define  $Q_{e-\text{ph}}$  mathematically, we consider the resonant limit ( $\omega_{ij} = \omega_0$ ) with a negligible bare cavity linewidth ( $C_{e-\text{ph}} \gg 1$ ). Then, the threshold  $Q_{e-\text{ph}} = 1$  corresponds to having  $\partial^2(|b_t/b_{\text{in}}|)/\partial\omega_{\text{RF}}^2 = 0$  at  $\omega_{\text{RF}} = \omega_0$ , with  $|b_t/b_{\text{in}}|$  given by equation (39) with  $\Lambda_0 = 0$ .

**Table 1.** Measured performances for various mesoscopic QED setups in the artificial atom limit. From left to right, we give the geometry considered, the nature of the nanoconductor used, the degree of freedom placed in resonance with the cavity, the cavity design and material, the reference in which the experiment is reported, the corresponding figure in the review, the cavity frequency  $\omega_0$ , the quality factor  $Q_0 = \omega_0/2\Lambda_0$  of the cavity, the light–matter coupling  $g_r$  between the electronic transition considered and the cavity, the decoherence rate  $\Gamma_2^*$  of the transition coupled to the cavity, and the ratios  $Q_{e-ph} = \sqrt{1 + \sqrt{2}g/\Gamma_2^*}$  and  $C_{e-ph} = g^2/\Gamma_2^*\Lambda_0$ . We use the abbreviations N = normal metal, F = ferromagnet, S = superconductor. Note that the parameters  $\Gamma_2^*$  and  $\Lambda_0$  are not FWHM parameters. They are rather defined such that no factor 1/2 occurs in the damping terms of equations (39) and (44). Hence, the full width at half maximum (FWHM) of the bare cavity transmission corresponds to the parameter  $\varkappa = 2\Lambda_0$ . With other conventions, the numerical factors in the definition of  $Q_{e-ph}$  and  $C_{e-ph}$  can differ.

Geometry	Double dot material	Degree of freedom	Cavity design	References.	Figure	$\omega_0/2\pi$ (GHz)	$Q_0$	$2g_r/2\pi$ (MHz)	$\Gamma_2^*/2\pi$ (MHz)	$Q_{e-ph}$	$C_{e-ph}$
N/dot/dot/N	graphene	Charge	Al stripe	[98] <sup>6</sup>	×	6.24	1600	12.4	430	0.022	0.046
N/dot/dot/N	InAs nanowire	Charge	Nb stripe	[39] <sup>7</sup>	×	7.86	3930	32	1500	0.016	0.17
N/dot/dot/N	Carbon nanotube	Charge	Al stripe	[36]	8	6.72	3500	6.6	345	0.015	0.033
F/dot/dot/F	Carbon nanotube	Quasi-spin	Nb stripe	[34]	10	6.75	11 200	2.6	2.5	0.81	2.3
N/dot/S/dot/N	Carbon nanotube	Charge	Nb stripe	[31]	11	6.64	16 000	10	~2	3.9	60
N/dot/dot/N	GaAs/AlGaAs 2DEG	Charge	Al stripe	[38]	16	6.85	2060	22	250	0.068	0.29
N/dot/dot/N	GaAs/AlGaAs 2DEG	Charge	Al SQUID array	[32]	×	5.02	~400	238	93	2	25
N/dot/dot/N	Si/SiGe 2DEG	Charge	Nb stripe	[30] <sup>8</sup>	9	7.68	7460	13.4	2.6	4.0	34
S/atom/S	Al atomic contact	Andreev state	Nb stripe	[35]	×	10.1	2200	74	26	4.4	90

two resonance peaks are visible in the cavity response  $|b_t/b_{in}|$  as soon as  $Q_{e-ph} \geq 1$ . Below, we discuss various circuit geometries where the transition  $i \leftrightarrow j$  corresponds to charge, spin or electron/hole degrees of freedom. The values of  $C_{e-ph}$  and  $Q_{e-ph}$  obtained for in these different cases are presented in table 1.

#### 4.2. Charge double quantum dots with normal metal contacts

**4.2.1. Hamiltonian of the device.** The case of a double quantum dot embedded in a microwave cavity has received a lot of experimental attention [36, 51, 52, 56, 59, 60, 90–98]. The intrinsic level separation  $\Delta_o$  between the orbitals of one dot (see equation (1)) is usually very large in comparison with the other energy scales of the device. Therefore, it is sufficient to consider a single orbital with energy  $\varepsilon_{L(R)}$  in dot  $L(R)$ . These two orbitals are coupled with a hopping constant  $t$ . In practice, each dot is also contacted to a normal metal reservoir, which enables one to control and measure the double dot charge. One can use the energy diagram of figure 7, where the Fermi levels in the reservoirs are filled up to the Fermi energy  $E_F$  and the orbital levels of the two dots have an energy separation  $\varepsilon = \varepsilon_L - \varepsilon_R$ . This last parameter can be controlled with the gate voltages  $V_g^L$  and  $V_g^R$  shown in figure 8.

<sup>6</sup>The resonance corresponding to line 1 in figure S6e of the supplement of [98] has been used to extract the numbers shown in table 1. The corresponding cavity parameters have been taken from figure S6a.

<sup>7</sup>The decoherence rate  $\Gamma_2^*$  of the double dot was not given directly in [39]. Therefore, we have determined from the figure S5a of its supplement the cooperativity  $C_{e-ph}$ , by using the equality  $C_{e-ph} + 1 = \bar{a}_{OFF}/\bar{a}_{ON}$  with  $\bar{a}_{OFF}$  and  $\bar{a}_{ON}$  the cavity transmission amplitude when the double dot is off-resonant and on-resonant respectively [34]. Using the numbers  $\omega_0/2\pi = 7.86$  and  $\Lambda_0 = \varkappa/2 = 1$  MHz given in the supplemental, one gets  $Q_0 = 3930$ .

Then, using  $C_{e-ph} = g^2/\Gamma_2^*\Lambda_0$ , one gets  $\Gamma_2^* = 1.5$  GHz.

<sup>8</sup>We use a definition of the cooperativity  $C_{e-ph}$  which is different from [30] for consistency with the other references.

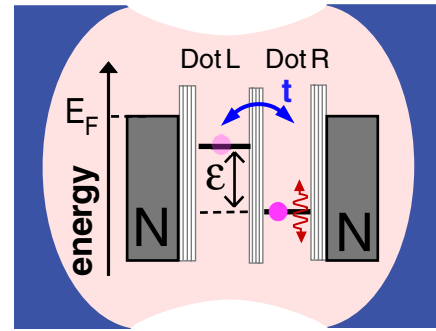


**Figure 7.** Schematic energy representation of a double quantum dot in a microwave cavity. The double dot orbitals in the left and right dots have energy separation  $\varepsilon$ , and are coupled with a hopping constant  $t$ . The normal metal reservoir states are filled up to the Fermi energy  $E_F$ . Here, we represent a case where only the right orbital energy level is modulated by the cavity electric field (red arrow).

It is possible to tune  $V_g^L$  and  $V_g^R$  such that there is a single electron in the double dot due to Coulomb blockade. In the spin-degenerate case, the spin degree of freedom can be disregarded to describe this situation since the two spin species play the same role and are not present simultaneously in the double dot. Therefore, the only internal degree of freedom relevant to describe the internal dynamics of the double dot in this limit is the left/right charge degree of freedom. In this framework, the double dot Hamiltonian writes

$$\hat{H}_0 = \frac{\varepsilon}{2}(\hat{c}_L^\dagger \hat{c}_L - \hat{c}_R^\dagger \hat{c}_R) + t\hat{c}_L^\dagger \hat{c}_R + t^* \hat{c}_R^\dagger \hat{c}_L + \hat{H}_{Coul} \quad (47)$$

where  $\hat{H}_{Coul}$  forbids the double occupation of the double dot. Using the basis of bonding and antibonding states of the double dot, one gets

$$\hat{H}_0 \simeq \frac{\omega_{DQD}}{2}(\hat{c}_-^\dagger \hat{c}_- - \hat{c}_+^\dagger \hat{c}_+) + \hat{H}_{Coul} \quad (48)$$

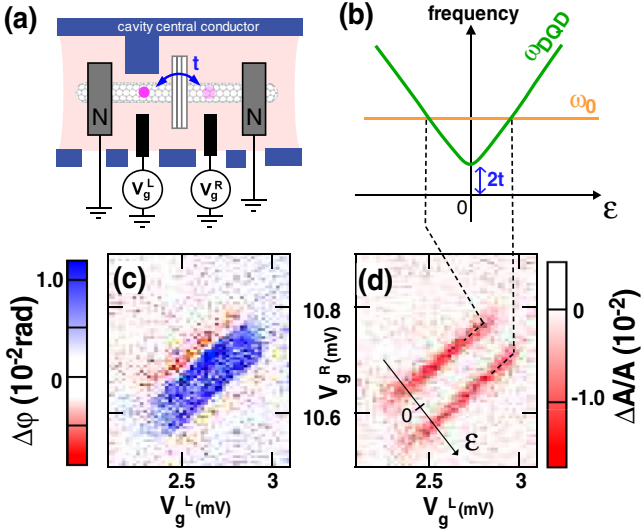


**Figure 8.** Response of a microwave cavity coupled to a double quantum dot with normal metal contacts. The device is represented schematically in panel (a). The energy levels in the left and right dots can be shifted using the gate voltages  $V_g^L$  and  $V_g^R$ . Using the simplified dispersion relation  $\omega_{\text{DQD}} = \sqrt{\varepsilon^2 + 4t^2}$  for the double quantum dot, the cavity and double dot are resonant twice when increasing  $\varepsilon$ , as shown by the dispersion curves of  $\omega_{\text{DQD}}$  and  $\omega_0$  in panel (b). These resonances are visible in the cavity phase signal of panel (c) as sign changes, and in the cavity dissipative signal of panel (d) as dissipation peaks. Adapted figure with permission from [36], Copyright (2014) by the American Physical Society.

with  $\omega_{\text{DQD}} = \sqrt{\varepsilon^2 + 4t^2}$  the double dot transition frequency. Above, we have used the creation operators

$$\hat{c}_+^\dagger = \cos[\theta/2]\hat{c}_L^\dagger + \sin[\theta/2]\hat{c}_R^\dagger \quad (49)$$

and

$$\hat{c}_-^\dagger = -\sin[\theta/2]\hat{c}_L^\dagger + \cos[\theta/2]\hat{c}_R^\dagger \quad (50)$$

for bonding and antibonding states in the dot, and the parameter  $\theta = \arctan[2t/\varepsilon]$ .

In most experiments designed so far, the samples have been designed with an asymmetric coupling of the two dots to the cavity, in order to modulate the parameter  $\varepsilon$  with the cavity electric field (see for instance figure 8(a)). In this case, following section 3.1.6, the interaction term between the double dot and the cavity can be expressed as

$$\hat{h}_{\text{int}}(\hat{a} + \hat{a}^\dagger) = (g_L \hat{c}_L^\dagger \hat{c}_L + g_R \hat{c}_R^\dagger \hat{c}_R) (\hat{a} + \hat{a}^\dagger) \quad (51)$$

with  $g_L \neq g_R$ . Using a rotating wave approximation, this term can be expressed as

$$\hat{h}_{\text{int}}(\hat{a} + \hat{a}^\dagger) \simeq g_t (\hat{a}^\dagger \hat{c}_-^\dagger \hat{c}_+ + \hat{a} \hat{c}_+^\dagger \hat{c}_-) \quad (52)$$

with

$$g_t = \frac{g_R - g_L}{2} \sin[\theta]. \quad (53)$$

This coefficient depends on the differential coupling  $g_R - g_L$  because the coupling to the cavity occurs through the modulation of the dot orbital detuning  $\varepsilon$ .

As we have seen in the previous section, in order to obtain the strong coupling regime, one needs to have a small enough  $\Gamma_2^*$ . The coherence of a charge double dot is mainly limited by charge noise due to charge fluctuators which move in the vicinity of the double dot. This induces fluctuations of the parameters which are electrically controlled, i.e.  $\varepsilon$  in the present case. This effect should be minimal at the charge noise sweet spot  $\varepsilon = 0$ , where  $\partial\omega_{\text{DQD}}/\partial\varepsilon = 0$ , similarly to what has been done for early days charge superconducting quantum bits—which are also affected by this problem [99]. Hence, it would be interesting to perform a systematic study of the figures of merit of the cavity/double dot resonance when the double dot parameters, and in particular  $\varepsilon$ , are varied.

In principle, the coupling of a double-dot dot to a microwave cavity can be mediated by other variables than  $\varepsilon$ , depending on the sample design. The first manipulations of the quantum state of a double dot were performed by modulating the parameter  $\varepsilon$  with a strong classical drive [22]. Recently, similar experiments were performed by modulating the interdot tunnel parameter  $t$  [71–73], following the theory proposal of [74]. One could push this idea further by building ac gates connecting the double dot barrier to the cavity central conductor, in order to modulate the interdot tunnel parameter  $t$  with the cavity electric field. In principle, this could enable one to obtain double dots with a better coherence, since the electric (and charge noise) control of the variable  $\varepsilon$  can be shunted, in this case. In section 4.4, we will discuss an alternative strategy to control electrically  $t$ , which involves using a superconducting contact.

**4.2.2. Master equation description.** This section shows how to calculate the cavity charge susceptibility  $\Xi(\omega_{\text{RF}})$  of the double dot when a microwave cavity is coupled to a single transition  $i \leftrightarrow j$  corresponding to the left/right charge degree of freedom of a double quantum dot. The dynamics of this mesoscopic QED device can be described by using a master equation approach (or Lindblad formalism) already widely used for cavity or circuit QED [75]. From equations (28), (47) and (52), one gets

$$\frac{d}{dt}\hat{a} = -i\omega_r\hat{a} - ig_t\hat{c}_-^\dagger\hat{c}_+ - \Lambda_0\hat{a} + \varepsilon_{\text{in}}e^{-i\omega_{\text{RF}}t} \quad (54)$$

$$\frac{d}{dt}\hat{c}_-^\dagger\hat{c}_+ = -i\omega_{\text{DQD}}\hat{c}_-^\dagger\hat{c}_+ + ig_t(\hat{n}_+ - \hat{n}_-)\hat{a} - \Gamma_2^*\hat{c}_-^\dagger\hat{c}_+ \quad (55)$$

with  $\Gamma_2^*$  the total decoherence rate of the double dot transition, which includes relaxation and dephasing effects. Importantly, the above equations are valid for  $\Gamma_2^* \ll k_B T$ . In the semiclassical limit with  $\omega_{\text{RF}} \simeq \omega_0$ , one can use equation (32) and the resonant expression

$$\hat{c}_-^\dagger\hat{c}_+ \simeq \langle \hat{c}_-^\dagger\hat{c}_+ \rangle_0 + \overline{\hat{c}_-^\dagger\hat{c}_+} e^{-i\omega_{\text{RF}}t} \quad (56)$$

Hence, equations (54) and (55) give

$$\bar{a} = \frac{\varepsilon_{\text{in}}}{\left(\omega_{\text{RF}} - \omega_0 + i\Lambda_0 - \frac{g_t^2(n_- - n_+)}{\omega_{\text{RF}} - \omega_{\text{DQD}} + i\Gamma_2^*}\right)} \quad (57)$$

with  $n_-$  and  $n_+$  the average occupation numbers of the bonding and antibonding states. A comparison with equation (35) gives

$$\Xi(\omega_{\text{RF}}) = \frac{g_T^2(n_- - n_+)}{\omega_{\text{RF}} - \omega_{\text{DQD}} + i\Gamma_2^*}. \quad (58)$$

The above equation corresponds to a well known result in the dispersive regime  $\omega_{\text{RF}} - \omega_{\text{DQD}} \gg \Gamma_2^*(V_g^L, V_g^R)$  where  $\Gamma_2^*$  can be disregarded (see for instance [76]). In this limit, depending on whether the nanocircuit is in the state  $+$  or  $-$ , the cavity shows a frequency pull  $\Delta\omega_0 = \pm g_T^2/(\omega_{\text{RF}} - \omega_{\text{DQD}})$ . This can be used to read out the state of the nanocircuit in a nondestructive way, since in this limit,  $\chi(\omega_{\text{RF}})$  accounts for second order processes which do not change the state of the nanocircuit. This method is widely used to read out the state of superconducting quantum bits [26]. In section 4.2, we consider double dots with no voltage bias, and we also assume that the dot levels are not resonant with the normal metal reservoirs, so that the electron which is trapped in the double dot cannot escape. We also assume that the power of the microwave tone applied to the cavity is too low to excite the transition between the bonding and antibonding states. In this case, at equilibrium, one has  $n_- = 1$  and  $n_+ = 0$ , which leads to equation (44).

#### 4.2.3. Experimental results.

**Weak coupling limit.** The resonance between a closed charge double-dot and a microwave cavity in the linear coupling regime has been measured by many groups, with various types of nanoconductor and grounded normal metal reservoirs. In all these experiments, the differential coupling  $g_R - g_L$  between the double dot and the cavity is reinforced thanks to a local ac gate connected only to one dot. First experiments have revealed a very weak light–matter coupling, i.e.  $Q_{e\text{-ph}} \ll 1$  (see table 1 for various examples). Figure 8 shows an example of experimental data obtained with a double dot made in a carbon nanotube [36], with an average photon number in the cavity  $\langle \hat{a}^\dagger \hat{a} \rangle \simeq 40$ . If  $2t > \omega_0$ , one has  $\omega_{\text{DQD}} > \omega_0$  for any value of  $\varepsilon$ , so that the double dot and cavity are always off-resonant and the signals  $\Delta\varphi$  and  $\Delta A$  show broad responses centered on  $\varepsilon = 0$  (not shown). For  $2t < \omega_0$ , two resonances between the cavity and the double dot are expected when  $\varepsilon$  varies, for  $\varepsilon = \pm\sqrt{\omega_0^2 - 4t^2}$  (see figure 8(b)). As expected from equation (58),  $\Delta\varphi$  shows two sign changes along the  $\varepsilon$  axis, corresponding to these two resonances (figure 8(c)), whereas  $\Delta A$  keeps a constant negative sign and shows two simple resonances (figure 8(d)). From the cavity signals of figure 8, one can determine  $(g_L - g_R)/2\pi = 3.3$  MHz and  $\Gamma_2^*/2\pi = 345$  MHz at  $\varepsilon = 0$ . With  $\Lambda_0 = 0.96$  MHz, this gives  $Q_{e\text{-ph}} = 0.015$  and  $C_{e\text{-ph}} = 0.033$ . Therefore, the strong coupling regime is far from being reached in this experiment.

In spite of a weak electron–photon coupling, it is possible to obtain interesting photon emission effects by applying a strong microwave drive to a double dot. This was shown recently with an InAs double dot. The same electron trapped in the double dot is repeatedly driven to the excited state by a microwave excitation with a strong amplitude which is off-resonant with the cavity and applied directly on the double dot gates. This generates a double dot population inversion.

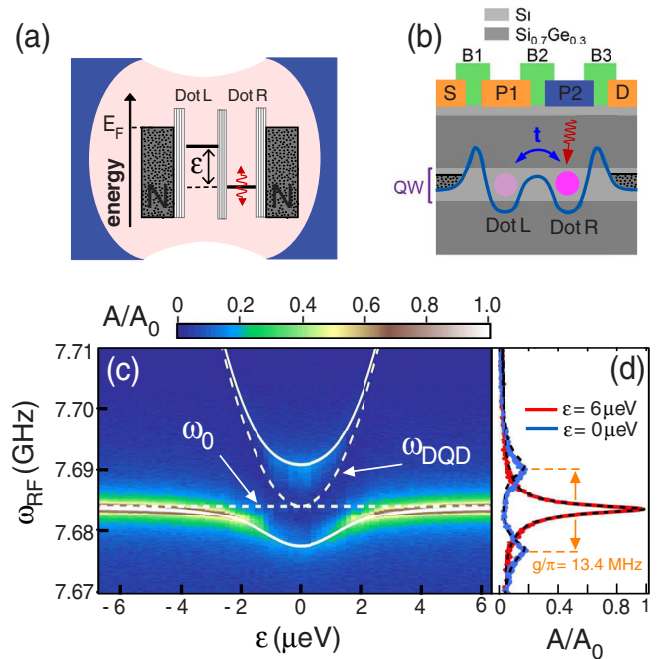


**Figure 9.** (a): Schematic representation of a double quantum dot with an orbital energy detuning  $\varepsilon$ , coupled to a microwave cavity. (b): Scheme of the cross-section through the DQD gates and Si/SiGe heterostructure used in [30] to implement the device of panel (a). The plunger gate P2 that is located above the quantum dot R is electrically connected to the central conductor of the superconducting coplanar cavity. An excess electron (magenta dot) is confined in the quantum well (QW) within the double well potential (blue line) created by the gate electrodes in green (c): Cavity transmission amplitude  $A/A_0$  as a function of  $\omega_{\text{RF}}$  and  $\varepsilon$  for  $2t = \omega_0 = 7.68$  GHz. The system eigenenergies for a coupling  $g = g_L - g_R = 0$  are represented over the data as white dashed lines. The calculated eigenenergies for  $g/2\pi = 6.7$  MHz are represented as solid lines. (d): Cavity signal  $A/A_0$  as a function of  $\omega_{\text{RF}}$  at  $\varepsilon = 6 \mu\text{eV}$  (blue line) and  $0 \mu\text{eV}$  (red line). The data for  $\varepsilon = 6 \mu\text{eV}$  show a cavity resonance splitting  $2g = 2\pi \times 13.4$  MHz characteristic of the strong coupling regime. Dashed lines are predictions from cavity input–output theory. Adapted from [30]. Reprinted with permission from AAAS.

which leads to cavity photon emission or absorption, with a rate which depends on the double dot and cavity dynamics, but also on the dissipation caused by phonons in the InAs nanowire [100].

**Strong coupling limit.** Very recently, the strong coupling regime was reached simultaneously in three experiments based on different types of charge double quantum dots [30–32]. In this regime, for a low number of photons  $\langle \bar{n} \rangle \rightarrow 0$ , the cavity transmission (or reflection) amplitude versus the frequency excitation  $\omega_{\text{RF}}$  shows a double peak, due to the strong hybridization between the cavity and the L/R charge degree of freedom of the double dot (see figure 9(d)). To reach this regime, the differential light–matter coupling  $g_L - g_R$  must be sufficiently large in comparison with the decoherence rate of the L/R degree of freedom, which is typically dominated by dephasing due to charge noise. In this case, the dephasing rate  $\Gamma_\varphi$  of the charge double dot takes the form [34]

$$\Gamma_\varphi \simeq \frac{\partial\omega_{\text{DQD}}}{\partial\varepsilon} E_c A + \frac{1}{2} \frac{\partial^2\omega_{\text{DQD}}}{\partial\varepsilon^2} E_c^2 A^2 \quad (59)$$

where  $E_c$  is the local charging energy of one dot (we disregard the mutual charging energy between the dots). Above,  $A$  is the dimensionless prefactor in the noise spectrum  $A^2/f$  which adds up to the reduced gate charge  $C_g^{L(R)} V_g^{L(R)}/e$  with  $C_g^{L(R)}$  the capacitance between dot  $L(R)$  and its gate voltage source with voltage  $V_g^{L(R)}$ . From equations (46), (53) and (59), in order to have  $Q_{e\text{-ph}} > 1$ , three different technical strategies are possible: either use a nanoconductor technology with an intrinsically lower charge noise (i.e. decrease  $A$ ) [30], or use a double dot with larger capacitances (i.e. decrease  $E_c$ ) in order to shunt the effect of charge noise [31], or change the cavity technology in order to increase the cavity electric field and thus the  $g_L - g_R$  factor [32]. These three strategies have already been implemented experimentally, as discussed in the paragraphs below. In all cases, using a device with  $\omega_0 = 2t$  should be advantageous, so that  $\Gamma_\varphi$  is only a second order effect in  $A$  when the device is tuned at the anticrossing between the cavity and the double dot (one has  $\varepsilon = 0$  and thus  $\partial\omega_{\text{DQD}}/\partial\varepsilon = 0$ ).

In [30], a double quantum dot in an undoped Si/SiGe heterostructure was used (see figure 9(b)). When the double dot is off resonant with the cavity, a single resonance is visible along the  $\omega_{\text{RF}}$  axis, which corresponds to the bare cavity resonance (see blue line in figure 9(c)). When  $\omega_0 = 2t$  is used, and when the double dot is tuned near its sweet spot ( $\varepsilon \sim 0$ ), the vacuum Rabi splitting is observed, i.e. a double cavity resonance is visible along the  $\omega_{\text{RF}}$  axis (see red line in figure 9(c)). In this device, the charge-photon coupling  $(g_L - g_R)/2\pi = 13.4$  MHz is comparable to what has been obtained with other charge double dots (see table 1). The microwave cavity is also similar to the ones used in previous experiments, with  $\Lambda_0 = 1.0$  MHz. The vacuum Rabi splitting is achieved thanks to an unusually small decoherence rate  $\Gamma_2^* = 2.6$  MHz of the left/right charge degree of freedom in the double dot. This gives light-matter coupling ratios  $Q_{e\text{-ph}} = 4$  and  $C_{e\text{-ph}} = 34$ . In the Si/SiGe two-dimensional structure used for this experiment, the dot charging energies are typically of the order of  $E_c \simeq 7$  meV [33]. In comparison, the GaAs/AlGaAs structure of [38] has smaller charging energies  $E_c \sim 1$  meV, but it is far from the strong coupling regime. This suggests that the low  $\Gamma_2^*$  value in [30] might be due to a much lower intrinsic charge noise in Si/SiGe devices. In agreement with this, in GaAs/AlGaAs devices, one of the smallest reported values of charge noise is [101] is  $A = 2.10^{-4}$ , whereas the values  $2.3 \cdot 10^{-6} < A < 1 \cdot 10^{-5}$  have been reported [102] for doped Si/SiGe heterostructures. Undoped Si/SiGe heterostructures might have an even lower charge noise [103]. The value of charge noise in Si/SiGe deserves a thorough investigation in order to confirm this picture.

Stockklauser *et al* [32] have used a GaAs/AlGaAs heterostructure similar to that in [38]. However, the coplanar waveguide architecture has been modified by replacing the central resonator of the cavity by an array of 32 superconducting quantum interference devices (SQUIDs). This

increases by a factor  $\sim 10$  the couplings  $g_{L(R)}$ . One has  $(g_L - g_R)/2\pi = 238$  MHz, and  $\Gamma_2^* = 93$  MHz which gives  $Q_{e\text{-ph}} = 2$  and  $C_{e\text{-ph}} = 25$ . These figures of merit are very close to those of [30]. However, they have not been obtained at the double dot sweet spot, since  $\omega_0 = 1.22 \cdot 2t$  was used. This could suggest that the above figures of merit are not the optimal ones for this setup. Interestingly, with the SQUID array architecture, the cavity frequency can be tuned by using an external magnetic field. However, the cavity decoherence rate is stronger with this architecture ( $\Lambda_0 = 6.2$  MHz).

Alternatively, [31] has reached the strong coupling regime to the left/right charge degree of freedom of a double dot by using a device with small charging energies. However, the double dot has a fundamentally different architecture in this experiment, since it comprises a superconducting contact, and since the coupling to the cavity photons seems to occur through the variable  $\varepsilon_L + \varepsilon_R$  instead of  $\varepsilon_L - \varepsilon_R$ . Therefore, we will discuss this experiment in section 4.5.

### 4.3. Mesoscopic QED with spins in quantum dot circuits

**4.3.1. Spin-photon coupling due to spin-orbit coupling.** The electronic spin degree of freedom draws a lot of interest in nanoconductors because it could be a good means to encode quantum information. Indeed, spins are expected to have a long coherence time in nanoconductors because they are more weakly coupled to their environment than charges. The counterpart of this immunity is that the natural magnetic coupling  $g_m$  between a spin and a standard coplanar microwave cavity is only a few 10Hz, which is not sufficient for manipulation and readout operations. It is possible to circumvent this difficulty by using a large number of spins, as demonstrated recently with several types of crystals coupled to coplanar microwave cavities [104–106]. However, in this case, the anharmonicity which is inherent in a two level system is lost, so that the spin ensemble can only be used as a quantum memory. To remain at the single spin level, it has been suggested to include in the microwave cavity a nanometric constriction to concentrate the cavity field, which would yield  $g_m \sim 10$  kHz [107, 108]. Alternatively, various theories have suggested to use a weak hybridization between the spin and charge degrees of freedom of a quantum dot circuit [9, 109–112], provided by a real or artificial spin-orbit coupling. To understand this effect, let us assume that the state of the dot circuit can be decomposed on a basis of pure spin eigenstates  $|\varphi_{n\uparrow}\rangle$  and  $|\varphi_{n\downarrow}\rangle$  with  $n \in \mathbb{N}$  an orbital index. In the presence of a spin-orbit coupling term the Hamiltonian of the dot circuit will be written:

$$\hat{H}_0^t = \sum_{n,\sigma} \left( E_n + \frac{E_z \sigma}{2} \right) |\varphi_{n\sigma}\rangle \langle \varphi_{n\sigma}| + \sum_{n,n'} (h_{mn'} |\varphi_{n'\downarrow}\rangle \langle \varphi_{n\uparrow}| + \text{H.c.}). \quad (60)$$

In the above,  $E_n$  is the orbital energy of state  $n$ ,  $E_z$  is the external Zeeman field applied to the circuit, and  $h_{mn'}$  corresponds to the matrix elements of the spin-orbit interaction on the basis of states  $|\varphi_{n\sigma}\rangle = c_{n\sigma}^\dagger |\emptyset\rangle$ . The photonic pseudo potential  $V_\perp$  is spin-conserving, so that the light-matter interaction given by equation (20) is

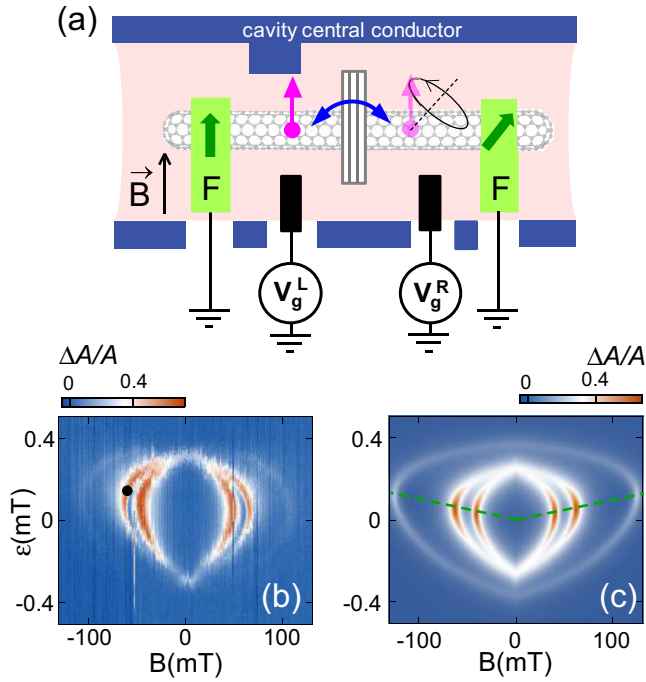


**Figure 10.** Response of a microwave cavity coupled to a double quantum dot with non collinear ferromagnetic contacts. The double dot is represented schematically in panel (a). The cavity dissipation of panel (b) displays various resonances which dependent on the orbital detuning  $\varepsilon$  of the double dot and the applied magnetic field  $B$ . This signal is reproduced theoretically in panel (c) (see text). The green dotted line corresponds to a sweet line with respect to charge noise. Adapted from [34]. Reprinted with permission from AAAS.

$$\hat{h}_{\text{int}} = \sum_{n,\sigma} V_{\perp}^{n,n'} |\varphi_{n'\sigma}\rangle \langle \varphi_{n\sigma}|. \quad (61)$$

Hence, at first order in spin–orbit coupling, the eigenstates

$$|\widetilde{\varphi}_{n\uparrow(\downarrow)}\rangle = |\varphi_{n\uparrow(\downarrow)}\rangle + \sum_{n'} \frac{h_{nn'}^*}{E_{n\uparrow(\downarrow)} - E_{n'\uparrow(\downarrow)}} |\varphi_{n'\downarrow(\uparrow)}\rangle \quad (62)$$

of  $H_0$  are coupled to the cavity with the matrix element

$$\begin{aligned} & \langle \widetilde{\varphi}_{n\downarrow} | \hat{h}_{\text{int}} | \widetilde{\varphi}_{n\uparrow} \rangle \\ &= \sum_{n'} \left( \frac{h_{nn'}}{E_n - E_{n'} + E_z} - \frac{h_{nn'}^*}{E_n - E_{n'} - E_z} \right) V_{\perp}^{n,n'}. \end{aligned} \quad (63)$$

One can imagine to build a qubit by using two states  $|\widetilde{\varphi}_{n\uparrow}\rangle$  and  $|\widetilde{\varphi}_{n\downarrow}\rangle$  which can be considered as quasi-spin states if the spin–charge hybridization is small. Due to this hybridization, this qubit will be sensitive to charge noise. Therefore, one has to choose a design which establishes a good compromise between having a small enough decoherence and a strong enough light–matter–coupling.

In principle, from equation (63), a single quantum dot with a natural Rashba or Dresselhaus spin–orbit coupling could already offer a spin–photon interaction. Indeed, the spin of a quantum dot was manipulated by using a large ac drive applied directly on the dot gate and coupled to the spin through the spin–orbit coupling [24, 39]. One can imagine replacing the direct ac drive by the cavity field. Then, the indices  $n, n'$  in

the above equations can correspond to the natural sub-bands in the dot spectrum. However, for most quantum dots, the spin–orbit interaction is too weak to enable the strong coupling regime with a single quantum dot circuit. For instance, for GaAs quantum dots, it has been shown theoretically that the effect of spin–orbit coupling is limited by the small spatial extension of the quantum dot [113–115]. As we will see in section 4.3.3, an alternative approach is to engineer extrinsically an artificial spin–orbit coupling by using a quantum dot circuit with ferromagnetic contacts, which induce local effective Zeeman fields such as those of equation (2). Then, it is not necessary to invoke the existence of several levels in each dot. For instance, in the case of a double quantum dot, the indices  $n, n'$  can be restricted to a pair of bonding and anti-bonding states, formed by the coherent coupling of left and right orbitals of the double dot. In principle, this should enable one to tune the value of the spin–orbit interaction, thanks to the electric control of the orbital energy detuning  $\varepsilon$ . Another interesting possibility could be to use designs which exploit stray fields from micromagnets [116, 117].

**4.3.2. Charge readout of spin-blockaded states in a double dot.** As shown in section 4.2, internal tunnel hopping of charges inside a double quantum dot modifies the cavity signals. This property can be used to detect with a dc current measurement the spin state of a pair of electrons trapped in a double quantum dot, thanks to a spin-rectification effect induced by Pauli spin blockade, which has been widely studied through current measurements [118]. This effect was recently exploited in a mesoscopic QED device, based on a singlet–triplet qubit in an InAs double quantum dot, with one electron in each dot [56]. The readout of this qubit requires discriminating the two states  $|S_{1,1}\rangle = (|L\uparrow, R\downarrow\rangle - |L\uparrow, R\downarrow\rangle)/\sqrt{2}$  and  $|T_0\rangle = (|L\uparrow, R\downarrow\rangle + |R\uparrow, L\downarrow\rangle)/\sqrt{2}$ . When the orbital detuning  $\varepsilon$  between the left and right dot is modulated by the cavity electric field, transitions to the state  $|L\uparrow, L\downarrow\rangle$  are possible only if the double dot initially occupies the state  $|S_{1,1}\rangle$ , due to the spin-conserving character of interdot tunneling. This leads to  $\Xi(\omega_{\text{RF}}) \neq 0$ . In contrast, if the double dot is in the state  $|T_0\rangle$ , one has  $\Xi(\omega_{\text{RF}}) = 0$  due to the Pauli exclusion principle. Therefore, the spin state of the double dot can be detected through the cavity signals. It is nevertheless important to point out that a direct spin–photon coupling was not implemented in the experiment of [56]. The state of the double dot was manipulated by applying a strong microwave drive directly to the dot gates, to rotate the spins thanks to spin–orbit coupling. The cavity was used only to perform the charge readout of the spin qubit. To date, no experiment has been able to detect a spin–cavity coupling caused by intrinsic spin–orbit coupling in a nanocircuit.

**4.3.3. Spin-photon coupling in a double quantum dot with non-collinear ferromagnetic contacts.** It was recently suggested that the coupling of equation (63) could be realized by using a double quantum dot with two ferromagnetic contacts magnetized in non-collinear directions [9], represented in figure 10(a). These contacts cause a spin-mixing of the double

dot eigenstates, which can be viewed as an artificial spin–orbit coupling. This effect occurs due to intradot effective Zeeman fields similar to those of equation (2). By tuning the orbital detuning  $\varepsilon$ , one can in principle control the degree of delocalization of the electron between the two dots, in order to tune the magnitude of the artificial spin–orbit interaction.

A first version of this device has been realized recently, by using a double quantum dot made in a single wall carbon nanotube on top of which two ferromagnetic PdNi contacts are deposited [34]. When the microwave transmission amplitude of the cavity is measured versus  $\varepsilon$  and the external magnetic field  $B$  applied to the double dot, three resonant lines appear (see figure 10(b)). Various features suggest that the spin degree of freedom is an important ingredient in this pattern. First, the resonances split and strongly move with the external magnetic field  $B$ , with a maximum of contrast/coherence for a finite value of  $B$ . Second, the black point of figure 10(b) corresponds to a coupling  $g_s = 1.3$  MHz and a double dot decoherence rate  $\Gamma_2^*/2\pi = 2.5$  MHz. This last number is about 1/200 of the charge decoherence rate determined for a similar carbon nanotube device (see section 4.2.3). One has  $Q_{e-ph} = 0.81$  which means that this device is almost in the strong coupling regime.

To understand the contribution of the spin degree of freedom to the cavity signals better, one can use equation (43) which is a generalization of equation (58), valid if the different transition frequencies  $\omega_{ij}$  of the nanocircuit are well separated. To calculate  $\omega_{ij}$  and the couplings  $g_{ij}$ , one has to use a double dot Hamiltonian which takes into account not only the existence of the left/right and spin degrees of freedom of the double dot, but also the K/K' local orbital degree in each dot (or valley degree of freedom), which is due to the fact that electrons can rotate clockwise or anticlockwise around the carbon nanotube. The linewidth of the resonances can be modeled by taking into account the effect of charge noise. This gives figure 10(c), which reproduces well the behavior of figure 10(b). The two strongest resonances mainly correspond to spin transitions with a conserved K/K' index. These two resonances are slightly split, due to a small lifting of the K/K' degeneracy. The third weaker resonance mainly corresponds to a transition where both the spin and the K/K' index are reversed. In figure 10(c), this transition is less visible than the two others because the K/K' degree of freedom is only weakly coupled to cavity photons, probably due to weak microscopic disorder in the carbon nanotube structure. However, this resonance is very interesting in the light of recent works which investigate the coupling between the valley degree of freedom of a silicon dot and a microwave cavity [128, 129].

Remarkably, the coherence (or, visually, the contrast) of the three transitions is maximal along the green dashed line in figure 10(c). This is because the derivative of the transition frequencies  $\omega_{ij}$  with respect to  $\varepsilon$  vanishes along this line, which is a charge noise sweet line. This behavior also occurs in the data, which confirms that charge noise is an important source of decoherence in this device. It may be possible to enhance these performances by reducing the spin–charge hybridization to decrease decoherence due to charge noise. It is expected that  $\Gamma_2^*$  will decrease more quickly than  $g_s$  with  $\varepsilon$ , so that the

strong coupling regime is accessible with this geometry, in principle [9].

**4.3.4. Spin–photon coupling in multiple particle devices with collinear fields.** Various theories have suggested coupling the spin degree of freedom to the cavity electric field by using two or three electron states in a quantum dot circuit. For that purpose, one can use a multi-quantum dot circuit with proper spin-symmetry breaking ingredients, in order to transduce the charge–photon into a spin–photon coupling. For instance, in a double dot with finite interdot hopping, the transition between the singlet and triplet spin states  $|S_{1,1}\rangle$  and  $|T_0\rangle$  is coupled to cavity photons due to the presence of a Zeeman field with constant direction but a different amplitude in the two dots [29, 119–121]. This field can correspond to an Overhauser field due to nuclear spins in a two-dimensional electron gas, or to stray fields from a ferromagnet. In the case of a triple quantum dot, it is possible to use three electron states from the ( $S = 1, S_z = 1/2$ ) subspace, with  $S$  the total spin of the dots, to define the resonant exchange qubit [123–125]. In this case, the spin–photon coupling can be obtained with a homogeneous Zeeman field if the spatial symmetry of the triple dot is adequately broken. Note that the above setups do not involve any real or effective spin–orbit interaction. On the contrary, they consider devices where the individual spin of electrons would be conserved in the single electron regime. At present, the multiparticle spin–photon coupling of [29, 119–125] is awaiting an experimental realization.

#### 4.4. Probing Andreev states with cavity photons

When superconducting elements are included in a nanocircuit, the electron and hole excitations become coupled by Andreev reflections, so that Andreev bound states appear inside the nanoconductors (see figure 2(c)). This superconducting proximity effect attracts much attention presently because it is at the heart of phenomena such as Majorana bound states in hybrid structures or Cooper pair splitting. Furthermore, Andreev bound states can appear on interfaces such as an atomic contact, for which the charge orbital confinement is not a relevant concept. One could hope that such states are weakly sensitive to charge noise and could be a good support of quantum information. It is therefore very interesting to investigate the properties of this degree of freedom with a microwave cavity, as suggested by [126]. In the presence of superconductivity, the Hamiltonian of the hybrid nanocircuit can be written as

$$\hat{H}_0^t = \sum_{\alpha} E_{\alpha} \gamma_{\alpha}^{\dagger} \gamma_{\alpha} \quad (64)$$

with  $E_{\alpha} > 0$  and  $\gamma_{\alpha}^{\dagger}$  a Bogoliubov–De Gennes excitation creation operator which is a superposition of  $\hat{c}_n^{\dagger}$  and  $\hat{c}_n$  operators. Hence, the interaction term with the cavity takes the general form [80]

$$\hat{h}_{\text{int}} = \sum_{\alpha} M_{\alpha\beta} \hat{\gamma}_{\alpha}^{\dagger} \hat{\gamma}_{\beta} + N_{\alpha\beta} \hat{\gamma}_{\alpha}^{\dagger} \hat{\gamma}_{\beta}^{\dagger} + N_{\alpha\beta}^{\dagger} \hat{\gamma}_{\alpha} \hat{\gamma}_{\beta}. \quad (65)$$

In the absence of magnetic coupling between the device and the cavity, the elements  $M_{\alpha\beta}$  and  $N_{\alpha\beta}$  can be expressed as

matrix elements induced by the cavity photonic pseudopotential between the wavefunctions associated to  $\hat{\gamma}_{\alpha(\beta)}^\dagger$  and  $\hat{\gamma}_{\alpha(\beta)}$  (see [80] for details). At zero temperature ( $T = 0$ ), equation (65) gives [49]

$$\chi(\omega_0) \simeq \frac{1}{2} \sum_{\alpha \neq \beta} \frac{|N_{\alpha\beta}|^2}{\omega_0 - E_\alpha - E_\beta + i0^+}. \quad (66)$$

Importantly, due to the Pauli exclusion principle, one has  $N_{\alpha\alpha} = 0$ , since a term in  $\hat{\gamma}_{\alpha}^\dagger \hat{\gamma}_{\alpha}^\dagger$  cannot occur in  $\hat{h}_{\text{int}}$ . Hence, from equation (66),  $\chi(\omega_0)$  does not involve transitions between electron and hole states associated with conjugated operators  $\hat{\gamma}_{\alpha}^\dagger$  and  $\hat{\gamma}_{\alpha}$  [49, 188]. This selection rule can be extended to a finite temperature ( $T \neq 0$ ) or a level broadening smaller than the inter-level separation [49]. Nevertheless, having a nanocircuit response at  $\omega_0 = 2E_\alpha$  is possible, provided there exists a state degeneracy  $E_\alpha = E_{\alpha'}$  in the nanocircuit so that a coefficient  $N_{\alpha\alpha'}$  comes into play [126], as observed in spin-degenerate superconducting atomic contacts [35]. In this experiment, an atomic contact between two superconductors was coupled to a microwave resonator through a superconducting loop. A light–matter coupling  $g = 74$  MHz and a decoherence rate  $\Gamma_2^*/2\pi = 26$  MHz were estimated inside a spin-degenerate Andreev doublet, which corresponds to  $Q_{\text{e-ph}} = 4.4$  and  $C_{\text{e-ph}} = 90$ . These good performances are probably related to a smaller sensitivity of atomic point contacts to charge noise.

Interestingly, devices have been built in which a microwave cavity is coupled to a superconducting circuit including a Josephson junction made out of a semiconducting nanowire quantum dot [57, 58]. The superconducting current in the Josephson junction is mediated by Andreev bound states inside the quantum dot. Since the spectrum of Andreev states is tunable via the dc gate of the dot, the critical current of the Josephson junction is electrically controllable. This can represent a technical advantage in comparison with usual magnetically tunable Josephson junctions made out of a SQUID. The nanowire junction is used to form the ‘Gatemon’ superconducting quantum bit, which involves a coupling between a microwave cavity and the superconducting phase difference between two metallic islands [57, 58]. This variable is a macroscopic collective degree of freedom of the superconducting circuit. Therefore, these devices belong more to the family of circuit QED devices than to the family of mesoscopic QED devices. This is why we will not discuss them further in this review.

#### 4.5. Double quantum dot with a central superconducting contact

Recently, the coupling scheme between a double quantum dot and a cavity was drastically modified by placing a superconducting contact between the two quantum dots instead of an insulating barrier, and two identical ac top gates on the two quantum dots [31] (see figure 11), instead of coupling asymmetrically the two dots to the cavity as done usually (see figure 1). In the symmetric coupling case of figure 11, the differential coupling  $g_L - g_R$  between the two dots and the

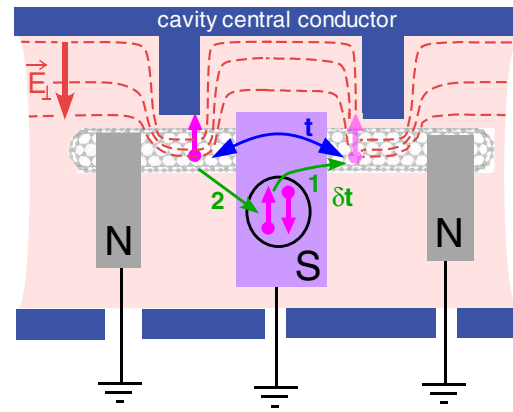


**Figure 11.** Scheme of a double quantum dot made in a carbon nanotube, with a central superconducting contact. Electrons can go from one dot to the other by direct tunneling through the nanotube section below the S contact (blue arrow), or by second order tunneling through the S contact (green arrows).

cavity is expected to be small. However, anticrossings were observed in the cavity response for a low number of photons in the cavity. These anticrossings can be switched on/off with the double dot gate voltages, and they vanish when the photon number is large so that the double dot transitions are saturated. This suggests that the cavity anticrossings are due to a strong coupling between the cavity and the double dot. A fitting of these anticrossings yields a coupling  $g_t = 10$  MHz and a decoherence rate  $\Gamma_2^*/2\pi \sim 2$  MHz which corresponds to  $Q_{\text{e-ph}} = 3.9$  and  $C_{\text{e-ph}} = 60$ .

This result may seem surprising, since a standard coupling to the left/right charge degree of freedom through the  $\varepsilon$  variable is unlikely for a small  $g_L - g_R$ . However, two ingredients can help in understanding the behavior of the setup. First, due to the superconducting gap, direct dissipative tunneling between the dot and the superconductors is forbidden, but second order tunnel processes from one dot to the other are allowed. This gives a renormalization  $\delta t$  of the tunnel coupling between the two dots which depends on the average orbital energy  $(\varepsilon_L + \varepsilon_R)/2$ . This last parameter is well coupled to cavity photons even when  $g_L = g_R$ . A coupling between the left/right degree of freedom of the double dot and the cavity photons can thus be restored. Second, there is a large capacitance between the dots and the ac top gates, so that the dot charging energies are decreased by a factor  $\sim 10$  (determined from conductance measurements) in comparison with the experiment of figure 8. This strongly reduces the sensitivity of the device to charge noise. This strategy is reminiscent of the strategy developed for the Transmon superconducting quantum bit. In this device, a very large charging energy is used to flatten the dispersion of the energy bands with gate voltages, and reduce the sensitivity to charge noise [127].

#### 4.6. Comparison between the different systems and conclusion

Table 1 presents a comparison of the performances of the different mesoscopic devices used to far to implement artificial atoms in a cavity. Impressive progresses are already visible

since the publication of the first experiments in [51, 54]. To summarize, charge and spin states in a double quantum dot, and Andreev bound states in atomic contacts have been strongly coupled to cavity photons. First experimental results are also available regarding the local orbital degree of freedom in a quantum dot, for Si/SiGe heterostructures [129], and carbon nanotube devices [34]. Other configurations have been proposed theoretically, which lack experimental realization at present. For instance, it has been suggested to use multiparticle spin states in devices with no spin-orbit coupling [29, 119–125]. It could also be interesting to use Shiba states which are Andreev states in the presence of a magnetic impurity or strong Coulomb interaction in a quantum dot [130]. Interestingly, several theoretical works have proposed manipulation protocols which circumvent at least partially the imperfections of mesoscopic QED devices, and in particular a limited coherence [112, 121, 131].

## 5. Mesoscopic QED experiments beyond the artificial atom limit

In the previous sections, we have shown that cavity photons are a powerful probe for the internal dynamics of a nanoconductor. The present section will show that a microwave cavity is also a very interesting tool to study the dynamics of tunneling between a nanoconductor and a metallic reservoir. The interplay between electron tunneling to reservoirs and the light-matter coupling leads to a very rich phenomenology [132–139], whose experimental investigation with microwave cavities has recently started.

### 5.1. Keldysh expression of the charge susceptibility of a nanocircuit

In section 4, the nanocircuit charge susceptibility  $\Xi$ , which sets the cavity signals in the linear semiclassical limit, was evaluated without taking into account explicitly tunnel processes towards the fermionic reservoirs of the nanocircuit. Hence, it is useful to introduce a more general calculation method for  $\Xi$ . For simplicity, we will assume that the coupling of the cavity to the fermionic reservoirs of the nanocircuit is negligible. In case of a quantum dot circuit, the cavity electric field simply modulates the potential of some quantum dots  $n$  with a coupling constant  $g_n$ , like in equations (28) and (30). Alternatively, in case of a one-dimensional conductor, a coarse grain description into sites with an index  $n$  can be used [49]. Then, in the semiclassical limit, the cavity signals (37) and (38) are set by the nanocircuit charge susceptibility  $\Xi(\omega_0)$ , defined by equations (34) and (36). Disregarding Coulomb interactions in the dots/sites, this quantity can be expressed by using the Keldysh formalism as

$$\Xi(\omega_0) = -i\text{Tr}\left[\int \frac{d\omega}{2\pi} \mathcal{C}(\omega) \mathcal{G}^r(\omega) \Sigma^<(\omega) \mathcal{G}^a(\omega)\right] \quad (67)$$

with

$$\mathcal{C}(\omega) = \hat{T} (\mathcal{G}^r(\omega + \omega_{\text{RF}}) + \mathcal{G}^a(\omega - \omega_{\text{RF}})) \hat{T}. \quad (68)$$

Here,  $\mathcal{G}^r(\omega)$  and  $\mathcal{G}^a(\omega) = (\mathcal{G}^r(\omega))^\dagger$  are the retarded and advanced Greens' functions of the dots or nanocircuit internal sites. These Green's functions have a matrix structure with elements  $\mathcal{G}_{B,A}^r(\omega) = \int_{-\infty}^{+\infty} dt \mathcal{G}_{B,A}^r(t) e^{i\omega t}$  with

$$\mathcal{G}_{B,A}^r(t) = -i\theta(t) \langle \{B(t), A(t=0)\} \rangle_{\hat{H}_{\text{int}}=0}. \quad (69)$$

Here,  $A, B$  are quasiparticle creation and annihilation operators inside a site  $n$  of the nanoconductor, and  $\langle \rangle_{\hat{H}_{\text{int}}=0}$  denotes an average calculated with the light-nanocircuit interaction turned off. The matrix  $\hat{T}$  is a diagonal matrix which corresponds to  $\text{diag}(g_n, -g_n)$  in the orbital block  $(n, n)$ . The derivation of equation (67) is given in appendix A. The matrix structure of  $\mathcal{G}^{r(a)}$  takes into account the sites and spin degrees of freedom of electrons and also the electron/hole degree of freedom if the nanocircuit includes superconducting elements (a few examples of  $\mathcal{G}^{r(a)}$  will be presented in the next sections). The self energy  $\Sigma^<(\omega)$  has a matrix structure similar to  $\mathcal{G}^{r(a)}$ , and it involves Fermi occupation factors of the fermionic reservoirs. The tunnel rates to the reservoirs affect the values of both  $\mathcal{G}^{r(a)}$  and  $\Sigma^<(\omega)$ , as we will see in various examples in the next sections. One advantage of the Keldysh approach is that it is very general. It can be used to describe the presence of many different types of reservoirs, such as normal metals, superconductors or ferromagnets, with possibly finite bias voltages leading to non-equilibrium transport effects. It also takes properly into account internal hopping between neighboring dots or sites, which leads to the internal transitions discussed in section 4. For instance, appendix B shows how to recover an expression of the charge susceptibility of a closed non-interacting double quantum dot similar to equation (58), by using equation (67). Other examples of use of equation (67) are given in sections 5.2, 5.3 and 5.5.3.

### 5.2. Effective admittance of a single quantum dot with normal metal contacts

The simplest possible example of quantum dot circuit which can be coupled to a microwave cavity is a single level quantum dot with a normal metal reservoir. This situation has been studied experimentally with carbon-nanotube quantum dots [37, 54]. It is possible to control electrically the energy detuning  $\varepsilon_d$  between the dot level and the Fermi energy of the reservoir (see figure 12(a)). The signals  $\Delta\varphi$  and  $\Delta A$  were measured as a function of  $\varepsilon_d$  for several dot levels with a different tunnel rate  $\Gamma_N$  between the dot and the normal metal reservoir (see figure 12, bottom panels, which represents the opposites of  $\Delta A$  and  $\Delta\varphi$ ). For  $\omega_0 \ll \Gamma_N$ , the  $\Delta A$  signal is very small while  $\Delta\varphi$  is always negative with a minimum at  $\varepsilon_d = 0$  (see figure 12(A)). For  $\omega_0 \gg \Gamma_N$ ,  $\Delta A$  seems globally larger but negative in any case, whereas  $\Delta\varphi$  changes sign and becomes positive around  $\varepsilon_d = 0$  (see figure 12(C)).

To understand this behavior, one can model the device with Hamiltonian (28) with

$$\hat{H}_0^t = \varepsilon_d \hat{c}_{d\sigma}^\dagger \hat{c}_{d\sigma} + \sum_{k,\sigma} \left( t \hat{c}_{k\sigma}^\dagger \hat{c}_{d\sigma} + t^* \hat{c}_{d\sigma}^\dagger \hat{c}_{k\sigma} \right) \quad (70)$$

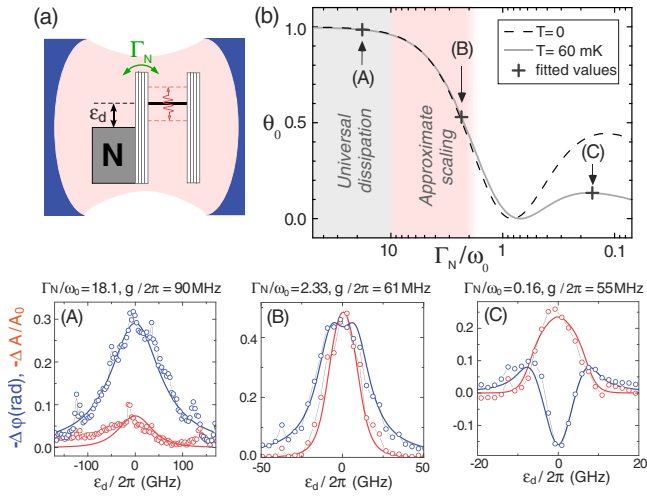


**Figure 12.** (a) Scheme of a microwave cavity coupled to a single quantum dot with a normal metal reservoir. (A)–(C): microwave response of the cavity versus the energy detuning  $\varepsilon_d$  between the dot orbital and the Fermi level of the reservoir, for various values of the tunnel rate  $\Gamma_N$  to the reservoir. Note that we represent the opposites of  $\Delta A$  and  $\Delta\varphi$ . The symbols are data and the lines are the theory discussed in the main text (b) Ratio  $\theta_0$  corresponding to the theory curves in panels (A)–(C). Adapted figure with permission from [37], Copyright (2016) by the American Physical Society.

and

$$\hat{h}_{\text{int}} = g\hat{c}_{d\sigma}^\dagger\hat{c}_{d\sigma}. \quad (71)$$

Here,  $t$  is the tunnel hopping parameter between the dot and the reservoir, and  $g$  the coupling of the dot level to cavity photons. The spin index is  $\sigma \in \{\uparrow, \downarrow\}$ . The tunnel rate between the dot and the reservoir can be expressed as  $\Gamma_N = 2\pi|t|^2$ . One can use the non-interacting Keldysh formalism of section 5.1 to calculate the charge susceptibility  $\Xi(\omega_0)$  which corresponds to equations (70) and (71). Here, we define

$$\mathcal{G}^r(\omega) = \begin{bmatrix} \mathcal{G}_{\hat{c}_{d\uparrow}, \hat{c}_{d\uparrow}^\dagger}^r & \mathcal{G}_{\hat{c}_{d\uparrow}, \hat{c}_{d\downarrow}^\dagger}^r \\ \mathcal{G}_{\hat{c}_{d\downarrow}, \hat{c}_{d\uparrow}^\dagger}^r & \mathcal{G}_{\hat{c}_{d\downarrow}, \hat{c}_{d\downarrow}^\dagger}^r \end{bmatrix}. \quad (72)$$

Equation (70) then gives

$$\mathcal{G}^r(\omega) = \frac{1}{\omega - \varepsilon_d + i\Gamma_N} \check{\mathbb{I}} \quad (73)$$

and

$$\check{\Sigma}^<(\omega) = i\Gamma_N f(\omega) \check{\mathbb{I}} \quad (74)$$

with  $f(\omega) = 1/(1 + \exp[\omega/k_B T])$  and  $\check{\mathbb{I}}$  the identity matrix in spin space. In this diagonal case, it is possible to reduce the number of Green's functions in expression (67) by using the identity

$$\mathcal{G}^r(\omega)\mathcal{G}^r(\omega - \omega_0) = \frac{\mathcal{G}^r(\omega - \omega_0) - \mathcal{G}^r(\omega)}{\omega_0}. \quad (75)$$

This leads to the result

$$\Xi(\omega_0) = \frac{G_{\text{ac}}(\omega_0)}{i\omega_0} \quad (76)$$

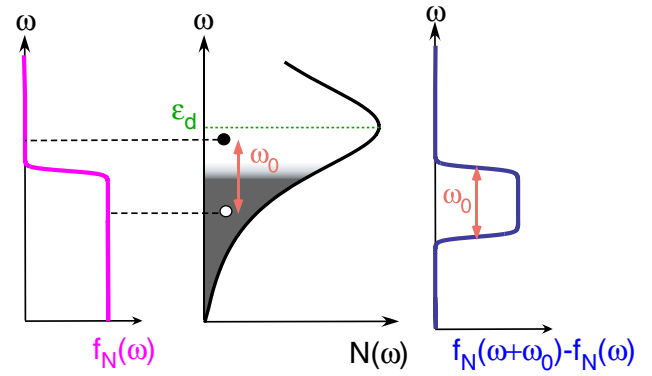


**Figure 13.** Plot of the Fermi factor  $f_N(\omega)$ , the dot density of states  $N(\omega) = -\text{Im}[\mathcal{G}^r(\omega)]/\pi$  dressed by tunneling to the reservoir, and the fermi factor difference  $f_N(\omega) - f_N(\omega - \omega_0)$ . The cavity with frequency  $\omega_0$  can induce the formation of electron-hole pairs in  $N(\omega)$  if the factor  $f_N(\omega) - f_N(\omega - \omega_0)$  is finite.

with

$$G_{\text{ac}}(\omega_0) = -ig^2\Gamma_N \int \frac{d\omega}{2\pi} \mathcal{G}^a(\omega - \omega_0)\mathcal{G}^r(\omega)(f(\omega) - f(\omega - \omega_0)). \quad (77)$$

Since the current through the tunnel junction corresponds to the time derivative of the charge on the dot,  $G_{\text{ac}}(\omega_0)$  naturally corresponds to the admittance of the dot. Interestingly, the interpretation of the expression (77) is straightforward:  $G_{\text{ac}}$  is due to the creation of electron hole pairs at energies  $\omega$  and  $\omega + \omega_0$  respectively, in the density of states (DOS) of the dot broadened by  $\Gamma_N$ . This creation is possible if the state at frequency  $\omega + \omega_0$  has a low occupation probability whereas the other state at  $\omega$  has a high occupation probability. This is taken into account by the difference of fermi factors in equation (77) (see figure 13).

Using equation (76), it is possible to reproduce quantitatively, the data of figures 12(A)–(C). In particular, the sign change in  $\Delta\omega_0$  when  $\Gamma_N$  decreases can be reproduced. Physically, for large tunnel rates  $\Gamma_N \gg \omega_0$ , the dot is able to absorb or emit electrons very quickly in response to the modulation of its potential by the cavity field. The dot thus behaves as an effective capacitor. Considering the cavity as a (L,C) resonator in parallel with this effective capacitor, this gives  $\Delta\omega_0 < 0$ . This behavior can be reproduced with a simple quasi-static model. In the semiclassical and resonant limit with  $\omega_0 \ll \Gamma_N$ , one has  $\langle \hat{c}_d^\dagger \hat{c}_d \rangle = n_d + (\partial n_d / \partial \varepsilon_d) \bar{a} e^{-i\omega_{\text{RF}} t}$ , with  $n_d$  being the average equilibrium value of  $\hat{c}_d^\dagger \hat{c}_d$  for  $g = 0$ , because the dot charge has the time to reach its equilibrium value at each time. Therefore, one has

$$\Xi(\omega_0 \ll \Gamma_N) = g\partial n_d / \partial \varepsilon_d. \quad (78)$$

Hence, from equations (37) and (38), one gets a cavity frequency shift  $\Delta\omega_0 = g^2 \partial n_d / \partial \varepsilon_d < 0$  which is minimum for  $\varepsilon_d = 0$ , in full agreement with figure 12 A. In contrast, for small tunnel rates  $\Gamma_N < \omega_0$ , there is a lagging effect in the charge current because the charge of the dot cannot follow instantaneously the level oscillation caused by the cavity field.

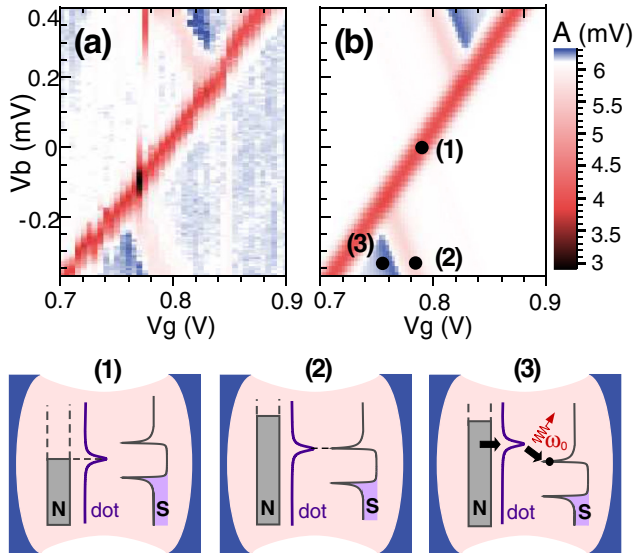


**Figure 14.** (a) Microwave transmission amplitude measured for a cavity coupled to a superconductor/quantum dot/normal metal bijunction. The white shade corresponds to the reference amplitude  $A_0 = 6.1$  mV and the blue and red shades to  $\Delta A > 0$  and  $\Delta A < 0$  respectively. (b) Similar quantity, calculated with the Keldysh approach (see text). Bottom panels: Scheme of the bijunction in different configurations: in (1), the dot level is resonant with the Fermi level of the normal metal, in (2), the dot level is resonant with a BCS peak of the superconductor, and in (3), the dot level has an energy higher than a BCS peak by  $\omega_0$ , which enables photo-assisted tunneling. Adapted figure with permission from [37], Copyright (2016) by the American Physical Society.

Hence, the dot has an inductive behavior which naturally leads to  $\Delta\omega_0 > 0$  (see figure 12(C)). Note that this capacitive to inductive cross-over has also been observed in [90].

The dissipative part of the cavity response in figure 12 might seem less interesting since it displays no sign change. However, many theoretical studies on the charge relaxation resistance in single quantum dots reveal a surprising universal charge relaxation resistance. This effect was first predicted by Markus Büttiker two decades ago [146, 147] for a non-interacting quantum dot tunnel contacted to a normal metal reservoir and capacitively coupled to an ac voltage source with frequency  $\omega_0$ . In this case, for low frequencies  $\omega_0 \ll \Gamma_N$ , the quantum dot circuit is expected to behave like a  $(R, C)$  circuit with a constant resistance  $R$ , independently of the circuit parameters. One can recover this result from equation (77). More precisely, in the limit  $\omega_0 \ll \Gamma_N$ , one finds that  $G_{ac}(\omega_0)$  can be written in the form  $G_{ac}(\omega_0) = i\omega_0 C + RC^2\omega_0^2 + o(\omega_0^3)$ , which corresponds to the expansion of the admittance of a  $(R, C)$  circuit at low frequency with [146, 147]

$$R = \frac{\pi \hbar}{4 e^2} \quad (79)$$

independently of the circuit parameters  $\varepsilon_d$  and  $\Gamma_N$ . From equations (37) and (38) and (76), for the device of figure 12(a), the universality of the charge relaxation resistance is equivalent to having a ratio

$$\theta = \frac{\pi}{4e^2 R} = \frac{\pi \omega_0 (\Delta\omega_0)^2}{2 g^2 \Delta\Lambda_0} \quad (80)$$

equal to 1 for any value of  $\varepsilon_d$ . Remarkably, this implies that the variations of  $(\Delta\omega_0)^2$  and  $\Delta\Lambda_0$  with  $\varepsilon_d$  should be similar since  $\theta$  and  $R$  should not depend on  $\varepsilon_d$ .

The value  $R = \pi\hbar/2e^2$  was experimentally confirmed for a two dimensional electron gas structure subject to a high magnetic field measured without a cavity, through a direct ac conductance measurement [140]. In this case, a similar phenomenology is expected, with  $\Xi$  divided by a factor of 2 and  $R$  multiplied by a factor of 2 due to the lifting of the spin degeneracy. However, the independence of  $R$  from  $\varepsilon_d$  could not be checked in this experiment. The data of figure 12 are consistent with this behavior, since they can be fitted by the equations (39), (67) and (73)–(77) (see full lines), which give equation (79) in the limit  $\omega_0 \ll \Gamma_N$ . Figure 12(b) shows the values of  $\theta$  calculated from this theory at  $\varepsilon_d = 0$  for the three resonances of the bottom panels. This shows that a broad range of frequency regimes could be addressed with this sample. The universality of  $R$  is expected in the gray area of figure 12(b) where  $\omega_0 \ll \Gamma_N$ . In the pink area of figure 12(b), one expects  $R < 1$ . The absolute value of  $R$  could not be measured in [37], but it was found that, in the pink area, the curves  $(\Delta\omega_0)^2$  and  $\Delta\Lambda_0$  versus  $\varepsilon_d$  show similar variations (see [37] for details). The scaling of the  $(\Delta\omega_0)^2$  and  $\Delta\Lambda_0$  curves in the gray area could not be studied accurately due to experimental noise. A further investigation of this regime would be very interesting.

Surprisingly, the data of figure 12 could be interpreted with a non-interacting theory, although Coulomb blockade was visible in finite bias voltage measurements (not shown). Hence, it would be interesting to understand to what extent the universality of the charge relaxation resistance is robust to interactions [141–145]. There is not yet a full consensus on this question, and the answer could depend on the regime of parameters considered. Mesoscopic QED experiments provide a new tool to study this question.

### 5.3. Photon emission by a superconductor/quantum dot interface

So far, we have discussed configurations in which the nanocircuit embedded in the microwave cavity is not voltage biased. However, the combination of the light–matter interaction and the out-of-equilibrium dynamics in a voltage-biased nanocircuit can lead to unique features. This is well illustrated by the case of a superconductor/quantum dot/normal metal bijunction embedded in a microwave cavity. Figure 14(a) shows the cavity dissipative signal  $\Delta A$  versus the gate voltage  $V_g$  of the dot, which shifts the energy level  $\varepsilon_d$ , and versus the finite bias voltage  $V_b$  applied to the normal metal contact. An area with  $\Delta A > 0$  appears (see blue area in figure 14(a)). This suggests that the bijunction emits photons for some regimes of parameters.

In order to understand this behavior, one can use again expression (67). To take into account the presence of superconducting correlations in the device, one can use the dot Green's function

$$\check{G}^{r(a)} = \begin{bmatrix} \mathcal{G}_{\hat{c}_{d\uparrow}, \hat{c}_{d\uparrow}^\dagger}^{r(a)} & \mathcal{G}_{\hat{c}_{d\uparrow}, \hat{c}_{d\downarrow}}^{r(a)} \\ \mathcal{G}_{\hat{c}_{d\downarrow}, \hat{c}_{d\uparrow}^\dagger}^{r(a)} & \mathcal{G}_{\hat{c}_{d\downarrow}, \hat{c}_{d\downarrow}^\dagger}^{r(a)} \end{bmatrix} \quad (81)$$

where  $\hat{c}_{d\sigma}^\dagger$  creates an electron with spin  $\sigma$  on the dot. One finds

$$\check{G}^r(\omega) = \begin{bmatrix} \omega - \varepsilon_d + i\frac{\Gamma_N}{2} & 0 \\ 0 & \omega + \varepsilon_d + i\frac{\Gamma_N}{2} \end{bmatrix} + i\frac{\Gamma_S}{2} \begin{bmatrix} G_\omega & F_\omega \\ F_\omega & G_\omega \end{bmatrix}. \quad (82)$$

Here,  $\Gamma_{N(S)}$  is the bare tunnel rate between the dot and the normal (superconducting) reservoir. The presence of superconducting correlations in the superconducting reservoir is described by the functions  $G_\omega = -i(\omega + i\frac{\Gamma_n}{2})/D_\omega$ , and  $F_\omega = i\Delta/D_\omega$  with  $D_\omega = \sqrt{\Delta^2 - (\omega + i\frac{\Gamma_n}{2})^2}$  and  $\Delta$  the gap of the superconductor. The parameter  $\Gamma_n$  accounts for a broadening of the BCS peaks in the DOS of the superconductor, which is observed experimentally. In the absence of superconductivity ( $\Delta = 0$ ), one has  $G_\omega = 1$  and  $F_\omega = 0$  so that the off-diagonal part of the Green's function, which describes the presence of superconducting correlations in the dot, vanishes. The self-energy  $\check{\Sigma}^<(\omega)$  corresponding to equation (82) is given in [37]. Using the above theory, equation (67) gives the results of figure 14(b), which reproduce closely the data of figure 14(a). The line marked with the circle (1) corresponds to a resonance between the dot orbital and the Fermi level in the normal metal, whereas the circle (2) corresponds to a resonance between the dot level and a BCS peak in the superconducting reservoir. The  $\Delta A > 0$  effect is due to inelastic tunneling from the dot level to one BCS peak, which triggers the emission of a cavity photon, as represented in figure 14.

It is interesting to evaluate the performance of the device of figure 14 as a photon emitter. In order to evaluate the emission rate  $\Gamma_e$  of photons in the cavity by the quantum dot circuit, one needs to calculate the time evolution of the average number of cavity photons  $\langle \hat{a}^\dagger \hat{a} \rangle = |\bar{a}|^2$ . By combining equations (31), (32) and the top left equation of figure 5, one gets

$$\frac{\partial |\bar{a}|^2}{\partial t} = \Gamma_e - 2\Lambda_0 |\bar{a}|^2 - \sqrt{2\Lambda_L} (\bar{a}b_{in}^* + b_{in}^*\bar{a}) \quad (83)$$

with

$$\Gamma_e = ig \left( \langle \hat{c}_{d\uparrow}^\dagger \hat{c}_{d\uparrow} \rangle + \langle \hat{c}_{d\downarrow}^\dagger \hat{c}_{d\downarrow} \rangle \right) (\bar{a}e^{-i\omega_{RF}t} - \bar{a}^*e^{i\omega_{RF}t}) \quad (84)$$

the emission rate of photons inside the cavity by the nanocircuit. This rate can be simplified by eliminating fast oscillating terms which do not contribute significantly to photon emission. Using the linear response expression

$$\sum_{\sigma} \langle \hat{c}_{d\sigma}^\dagger \hat{c}_{d\sigma} \rangle (t) = \Xi(\omega_{RF}) \bar{a} e^{-i\omega_{RF}t} + \Xi(-\omega_{RF}) \bar{a}^* e^{i\omega_{RF}t} \quad (85)$$

with  $\Xi(-\omega_{RF}) = \Xi(\omega_{RF})^*$ , we get

$$\Gamma_e = 2 \text{Im}[\Xi(\omega_{RF})] |\bar{a}|^2. \quad (86)$$

From equation (38) and (42), this can be expressed in terms of the experimental signals as:

$$\Gamma_e = 2 \frac{\Delta A \Lambda_0}{A_0} \langle \hat{n} \rangle. \quad (87)$$

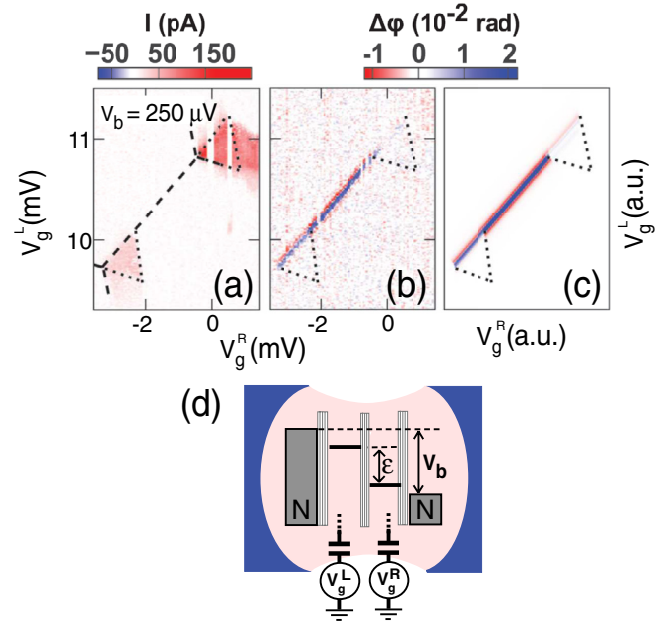


**Figure 15.** (a) dc current through a carbon-nanotube double quantum dot versus the gate voltages  $V_g^L$  and  $V_g^R$  for a finite bias voltage  $V_b = 250 \mu\text{V}$ . (b) Corresponding cavity signal  $\Delta\varphi$  (c) Theoretical predictions for  $\Delta\varphi$ , obtained with equation (58) and a master equation calculation of  $n_+$  and  $n_-$  at zeroth order in  $g_t$ . Adapted figure with permission from [36], Copyright (2014) by the American Physical Society.

The data of figure 14 were measured with an average photon number  $\langle \hat{a}^\dagger \hat{a} \rangle \sim 120$  in the cavity. The calibration of the experiment also gives  $\Lambda_0 \sim 2\pi \times 0.26$  MHz and  $A_0 \sim 6.1$  mV. The area with  $\Delta A > 0$  in figure 14 corresponds to  $\Delta A/A_0 \simeq 0.03$ . From equation (87), this gives  $\Gamma_e \sim 2\pi \times 2$  MHz, which corresponds to an inelastic current of the order of 0.3 pA. This current was not detectable in the experiment because of current noise.

#### 5.4. Voltage-biased double quantum dot in a cavity

**5.4.1. Probing out-of-equilibrium double dot populations with a microwave cavity.** From equation (58), current transport in the double dot can modify the cavity signals by modifying the populations  $n_-$  and  $n_+$  of the bonding and antibonding states. The transport configuration can be tuned electrically through the double dot gate voltages  $V_g^L$  and  $V_g^R$  and source-drain bias voltage  $V_b$ . Figure 15 presents results obtained with a carbon nanotube double quantum dot with a finite Coulomb interaction [36]. As observed usually, the current  $I$  through the double dot is finite only inside some triangles in the  $V_g^L - V_g^R$  plane where the bonding or antibonding states are inside the transport window opened by the source-drain voltage  $V_b$  (figure 15(a)). The cavity signal  $\Delta\varphi$  is maximum along the line  $\varepsilon = 0$  where  $\omega_{\text{DQD}} - \omega_0$  is minimum (figures 15(b)), and it takes a different value along the transport triangles, because the populations of  $n_-$  or  $n_+$  are modified by transport. In figure 15(c), this behavior is well reproduced by using equation (58), with  $n_-$  and  $n_+$  calculated with a master equation approach at lowest order in the light-matter coupling ( $g_t = 0$ ) (see details in

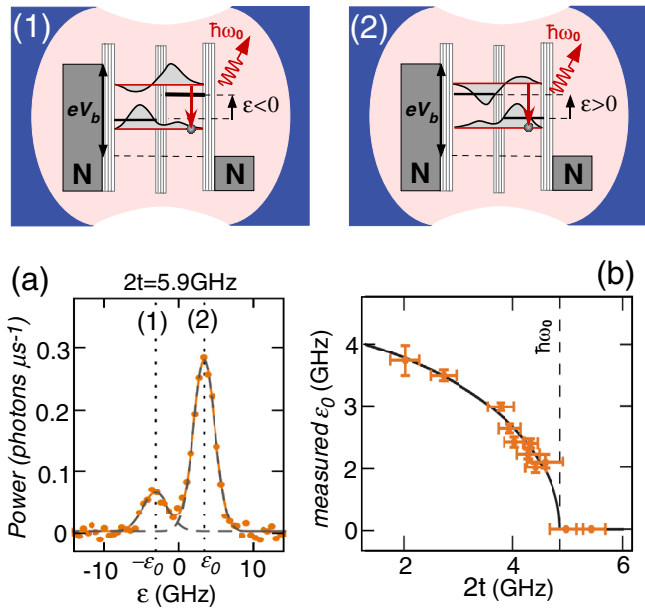


**Figure 16.** Top panels: scheme of a double dot subject to a finite bias voltage  $V_b$ , with a negative orbital detuning ( $\epsilon < 0$ , panel (1)) or a positive orbital detuning ( $\epsilon > 0$ , panel (2)). Bottom panels: measurements performed with a GaAs/AlGaAs heterostructure. (a) Number of photons  $P$  emitted by the cavity per unit time versus the orbital detuning  $\epsilon$ . The dotted lines corresponds to the situations depicted in panels (1) and (2). (b) Resonant detuning  $\epsilon_0$  measured for different values of interdot coupling  $t$ . The dots/squares are data points and the full lines a theory based on a master equation approach. Reprinted adaptation with permission from [38], Copyright (2015) by the American Physical Society.

[36]). In the regime  $\Gamma_{L(R)} \ll k_b T$ , this approach is sufficient to take into account Coulomb blockade, which essentially affects the structure of the nanocircuit state space and tunnel rates. The inclusion of Coulomb interactions in the Keldysh formalism is a more complex task [148]. Note that however, in the non-interacting case, the Keldysh approach also reproduces well the fact that  $\Delta\varphi$  is affected by current transport through a modification of  $n_- - n_+$  (see appendix B). Remarkably, the dc current through the double dot and the cavity signals are qualitatively different, since the cavity signals directly probe  $n_- - n_+$  whereas the current  $I$  is a more complex combination of  $n_-$ ,  $n_+$  and the double dot parameters. Therefore, the simultaneous study of the two signals can again enable a more accurate characterization of the double dot parameters.

**5.4.2. Photon emission below the lasing threshold.** The splitting between the bonding and antibonding states of the double dot can become resonant with the cavity if  $\epsilon$  is tuned properly. In this regime, it is possible to obtain photon emission due to the dc voltage bias. This phenomenon has been investigated in two dimensional electron gas structures and semiconducting nanowires [38, 39]. In [38], the number  $P$  of photons emitted by the cavity per unit time was measured as a function of the double dot detuning  $\epsilon$  for a constant interdot detuning  $t$  (see figure 16(a)). For  $2t > \omega_0$ , two resonances appear in  $P$ , for orbital detunings  $\epsilon = \pm\epsilon_0$  with  $\epsilon_0 = \sqrt{\omega_0^2 - 4t^2}$ . The resonance for  $\epsilon < 0$  is less pronounced than the resonance for

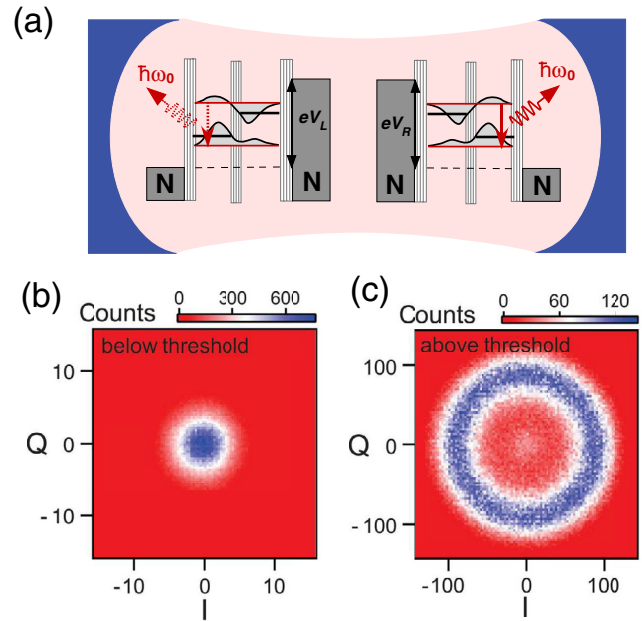


**Figure 17.** (a): Scheme of a microwave cavity coupled to two double quantum dots. (b) Measured  $I$ - $Q$  tomography of a cavity output field, in the presence of two InAs nanowire double dots, when one double dot is resonant with the cavity and the other off resonant. (c) Measured  $I$ - $Q$  tomography of the cavity output field when the two double dots are resonant with the cavity. Adapted from [40]. Reprinted with permission from AAAS.

$\epsilon > 0$  because it requires that the electrons tunnel from the left reservoir to an antibonding state which has little extension on the left dot (see figure 16(1)). Figure 16(b) shows the measured value of  $\epsilon_0$  versus  $t$ , which can be tuned via gate voltages in two dimensional electron gas structures. As expected,  $\epsilon_0$  vanishes for  $2t > \omega_0$ , because it is not possible to satisfy the resonant condition  $\omega_{\text{DQD}} = \omega_0$  in this case. In this limit, the cavity shows a single resonance centered on  $\epsilon = 0$  (not shown). The light-matter coupling in this experiment can be estimated from the parameters  $g/2\pi = 11$  MHz,  $\Gamma_2^*/2\pi = 250$  MHz and  $\Lambda_0 = 1.7$  MHz, which corresponds to  $Q_{e-\text{ph}} = 0.068$  and  $C_{e-\text{ph}} = 0.29$ . The data were interpreted with a master equation approach similar to that of [36] (see section 5.4.1). In the out-of-equilibrium regime, the rate of photon emission in the cavity by the double dot is  $\Gamma_e \sim 2\pi \times 0.3$  MHz. This number is similar to the performances obtained with the normal metal/dot/superconductor bijunction of section 5.3.

**5.4.3. Photon emission above the lasing threshold.** In principle, when a double dot with  $\Gamma_\varphi^* \gg \Gamma_1$  is resonant with a cavity ( $\omega_{ij} = \omega_0$ ), it is possible to obtain a lasing effect, which corresponds to an emission of a coherent microwave radiation by the double dot, if  $C_{e-\text{ph}} \gtrsim 1/2$  [149–156]. When  $C_{e-\text{ph}} < 1/2$ , it is possible to reach the lasing regime by coupling several double quantum dots to the cavity. This was recently realized with two double dots made in InAs nanowires [40, 41]. Figure 17 shows the in-phase and quadrature phase components  $I$  and  $Q$  of the output field of the cavity, measured when only one of the dots fulfills  $\omega_{\text{DQD}} = \omega_0$  (panel (b)) or when the two dots satisfy  $\omega_{\text{DQD}} = \omega_0$  (panel (c)). In the first case, the cavity

photons show a thermal distribution, because the device is below the lasing threshold. In the second case, the ‘ring’ in the tomography reveals a coherent photonic emission, because the device is above the lasing threshold. An average photon number in the cavity  $\langle \hat{a}^\dagger \hat{a} \rangle \simeq 8000$  is estimated in this last case. The rate of photon emission by the double dot can be estimated as  $\Gamma_e \simeq \langle \hat{n} \rangle \omega_0 / 2Q_0 = 10$  GHz, which is significantly larger than in [37, 38]. Charge noise limits the maser linewidth. However, a linewidth narrowing by more than a factor of ten can be obtained by using a microwave input tone that stabilizes the frequency of laser emission by triggering stimulated emission [41]. This technique is known as injection locking in the field of conventional lasers [157]. Note that in the lasing regime, the linear theory of section 3.2 fails. We refer interested readers to [159] for a simple theoretical description of this limit. Interestingly, there is a close analogy between the lasing effect produced in a microwave cavity by an out-of-equilibrium quantum dot, and that obtained with a Josephson superconducting transistor with a finite voltage bias [160]. In this second case, the lasing transition corresponds to a change in the number of Cooper pairs inside a superconducting island. In [160], a photon emission rate inside the cavity  $\Gamma_e \simeq 2$  GHz has been obtained, which is comparable to the performance of [41].

### 5.5. Characterizing exotic condensed matter systems with a microwave cavity

In the previous sections, we have considered relatively simple situations with nanocircuits made out of only one or two dots and fermionic reservoirs, in the non-interacting regime or in the Coulomb blockade regime. However, this section shows that the use of more complex circuits, possibly with many-body correlations, enables one to study non-trivial quantum transport effects or condensed matter problems in a new way. Cavity photons appear as a new tool which can give qualitatively different information on exotic excitations in a nanocircuit, in comparison with traditional dc transport measurements. With mesoscopic QED devices, it is possible to measure dc currents through the nanostructure and the microwave cavity response simultaneously. The joint study of these two non-equivalent signals is particularly informative, as we will see below.

**5.5.1. Kondo quantum dots.** The Kondo effect has been observed experimentally since the 30s (see for instance [161]). Although the resistivity of bulk metals is expected to decrease with temperature, for some metals containing a small amount of magnetic impurities an increase was observed below the Kondo temperature  $T_K$ . Thirty years later, Kondo suggested that this behavior is due to spin-flip scattering processes between the itinerant electrons of the metal and the magnetic impurities [162]. These processes give birth to a Kondo cloud, which screens the spins of the impurities and reduces the conductivity of the metal.

More recently, it was shown that quantum dots can also be used to study the Kondo effect if they are subject to a strong Coulomb interaction [163–165]. In this case, the spin-flip

scattering processes give rise to an increase of the dot zero-bias conductance. This effect depends on the value of the charging energy  $U$  to add a second electron in a dot level. If  $U$  is large, and the dot orbital energy  $\varepsilon_d$  fulfills  $-U < \varepsilon_d < 0$ , there can only be a single electron in the dot orbital, whose electronic spin simulates a local magnetic impurity. Then, if the dot is coupled to normal metal contacts with a high enough tunnel rate  $\Gamma_N$ , the local spin in the dot can fluctuate due to even order tunnel processes, which change the dot spin but not its charge. These processes involve intermediate virtual dot states with a different charge (dot orbital empty or doubly occupied), which are energetically forbidden but quantum mechanically allowed for a very short amount of time  $\sim \hbar/U$ . Therefore, the Kondo effect should remain transparent to a microwave cavity which is only sensitive to charge fluctuations at frequencies  $\omega \lesssim \omega_0$ . Importantly, this test requires that the cavity is mainly coupled to the dot level, so that the cavity signals are set by the dot charge susceptibility. Conversely, if the cavity modulates the potentials of the source and drain reservoirs asymmetrically, the cavity signals can reveal resonances similar to the Kondo conductance peak, as found experimentally in [54, 166].

The charge susceptibility of a Kondo dot has been studied recently in a carbon nanotube quantum dot coupled to the cavity through the dot energy level alone [167]. Both the Kondo regime and the Coulomb blockade regime have been studied with the same sample. In the Coulomb blockade regime, the conductance peaks through the dot are also visible in the cavity signals because they correspond to real charge fluctuations which are visible by cavity photons. However, in the Kondo regime, the low energy Kondo peaks are visible in the dot conductance but not in the cavity signals. Hence, the Kondo effect corresponds to conduction through essentially frozen charges in the dot (for a detector with a frequency cutoff  $\omega_0 \ll T_K$ ). This illustrates the decoupling of the spin and charge dynamics in the Kondo effect.

**5.5.2. The Cooper pair splitter.** The spatial separation of spin-entangled electrons from a Cooper pair is an interesting goal in the context of quantum computation and communication. In principle, a Cooper pair beam splitter (CPS) connected to a central superconducting contact and two outer normal metal (N) contacts could facilitate this process [10]. The spatial splitting of Cooper pairs has been demonstrated experimentally from an analysis of the CPS average currents, current noise, and current cross-correlations, in devices made out of a carbon nanotube [168–173] or a semiconducting InAs quantum wire [174]. However, new tools appear to be necessary to investigate further the Cooper pair splitting dynamics, and in particular its coherence, which has not been demonstrated experimentally so far in the N/dot/S/dot/N geometry. This coherence has two intimately related aspects: the coherence of Cooper pair injection and the conservation of spin entanglement. The first aspect is due to the fact that Cooper pair injection into the CPS is a coherent crossed Andreev process, which produces a coherent coupling between the initial and final states of the Cooper pair in the superconducting contact and the double dot. In this context, coupling the CPS to a

microwave cavity would be very interesting because it would enable one to perform the spectroscopy of the CPS and identify anticrossings in the CPS spectrum, which are due to the coherence of the injection process [43]. Detecting the conservation of spin entanglement represents an even greater challenge. In principle, microwaves couple to transitions between the states of the CPS with matrix elements which keep signatures of the coherent superposition of spin states displayed by a singlet state. Therefore, a microwave cavity could help to characterize split singlet states [42]. Interestingly, a supercurrent was recently observed in Josephson junction made out of two self-assembled quantum dots coupled in parallel to two superconducting contacts [175]. The observation of a supercurrent necessarily implies a non-dissipative and thus coherent pair injection process. However, even in this case, the use of a microwave cavity would be very interesting to characterize the device further, i.e. perform its spectroscopy and check whether the coherent Cooper pair injection really goes together with a spin-entangled double dot state.

**5.5.3. Majorana nanocircuits.** Majorana quasiparticles are among the most intriguing excitations predicted in condensed matter physics [176]. By definition, the creation operator  $m^\dagger$  of a Majorana quasiparticle is self adjoint, i.e.  $m^\dagger = m$ . This property offers possibilities of non-Abelian statistics [177] and topologically protected quantum computation [178] in condensed matter systems. It has been found that different types of hybrid electronic circuits could enclose Majorana quasiparticles. In particular, hybrid structures combining a semiconducting nanowire in contact with a superconductor raise a lot of attention [179–185]. It has been predicted that in some situations a single pair of overlapping Majorana bound states ( $\hat{m}_L, \hat{m}_R$ ) could appear inside a semiconducting nanowire, with an overlap which can be switched off with an external magnetic field or a gate voltage, in order to obtain two isolated Majorana bound states [186, 187]. Recently, pairs of conductance peaks with a splitting oscillating and decaying with the magnetic field were observed, in striking agreement with these predictions [183, 184]. However, so far, mainly dc conductance measurements have been used, which reveal essentially the DOS of the nanowire. This gives only a very indirect access to the property  $m^\dagger = m$ . A microwave cavity could represent an interesting tool to test this property more directly, since the self-adjoint property affects the structure of the light–matter coupling. Here, we will mainly focus on the proposal of [49], which considers a nanowire contacted to a superconducting contact and two normal metal tunnel probes (figure 18(a)). In practice, it is possible to measure  $\Delta\Lambda_0$  from the cavity response and the DOS of the nanowire simultaneously by using the tunnel probes. The Keldysh theory was used to calculate these two quantities, by using a coarse grained description of the nanowire (see equation (67) and figures 18(b) and (c)). To understand how a Majorana pair affects physical signals, it is convenient to reexpress the degree of freedom associated with the Majorana pair by defining an ordinary fermion operator  $\hat{\gamma}_1^\dagger = (\hat{m}_L - i\hat{m}_R)/\sqrt{2}$  which fulfills  $\{\hat{\gamma}_1^\dagger, \hat{\gamma}_1^\dagger\} = 1$ . At low energies, in the subspace spanned by  $\hat{\gamma}_1^\dagger$ , one gets the nanocircuit Hamiltonian (23) with

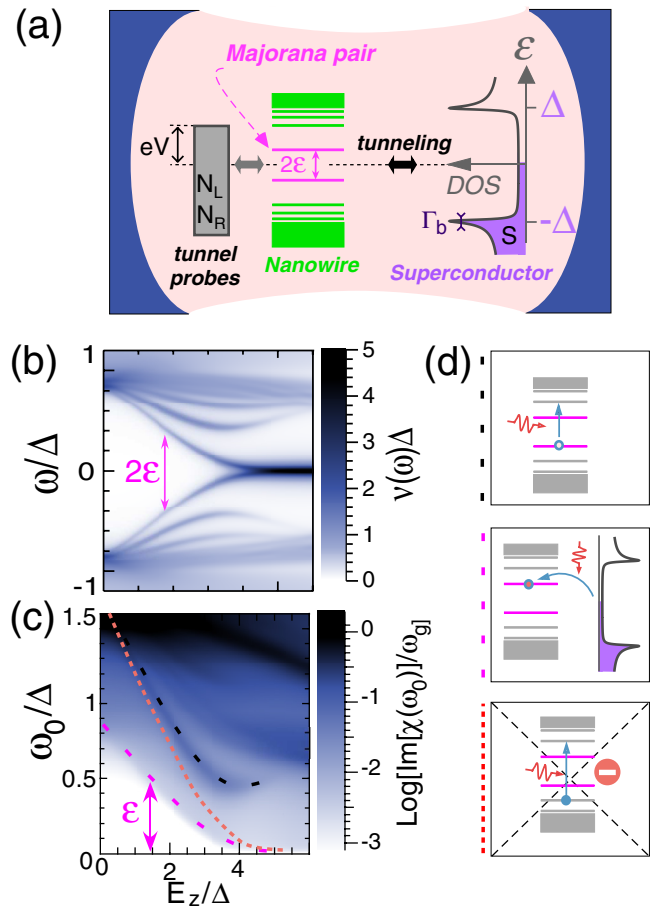


**Figure 18.** (a) Energetic scheme of a Majorana nanowire coupled to a microwave cavity. The energy levels in the Majorana nanowire (green and pink lines) are coupled to a superconducting contact (in purple) and two normal metal contacts (in grey). The Majorana doublet in pink has an energy splitting  $2\varepsilon$ . (b) Calculated density of states in the nanowire. (c) Calculated microwave response of the cavity coupled to the nanowire. (d) Schemes of the processes contributing to the resonances highlighted with the dashed lines in panel (c) (see main text). Adapted from [49], Copyright (2017) by the American Physical Society.

$\hat{H}_0 = \varepsilon\hat{\gamma}_1^\dagger\hat{\gamma}_1$  and  $\hat{h}_{\text{int}} = \beta\hat{\gamma}_1^\dagger\hat{\gamma}_1$  (with the conventions of equations (64) and (65), one has  $\varepsilon = E_1$  and  $\beta = M_{11}$ ). This means that the Majorana pair corresponds to a fermionic state which can be split into two fully independent parts for  $\varepsilon = 0$ . In the simplest situation, when the nanowire is driven to its topological phase,  $\varepsilon$  tends to zero, by showing or not an oscillatory behavior, depending on the length of the nanowire. The electron–hole conjugated pair ( $\hat{\gamma}_1^\dagger, \hat{\gamma}_1$ ) appears in the DOS of the nanowire as a pair of resonances at  $\varepsilon$  and  $-\varepsilon$  (see figure 18(b)). However, no transition should be visible in the cavity signals at  $\omega_0 = 2\varepsilon$  because from equation (66), the cavity photons cannot induce transitions between a pair of electron–hole conjugated states (see figure 18(c)). Nevertheless, the light–Majorana coupling has physical consequences, since it can induce a step at  $\omega_0 = \varepsilon$  in the  $\Delta\Lambda_0$  signal. This feature is due to photo-assisted tunneling between the Majorana pair and the residual zero-energy DOS in the imperfect superconducting reservoir. It can be used to check that the low-energy doublet is well coupled to cavity photons, so that

the absence of a cavity resonance at  $\omega_0 = 2\varepsilon$  is not due to  $\beta = 0$ . Then, the simultaneous presence[absence] of the step at  $\omega_0 = \varepsilon[2\varepsilon]$  would represent a good indication that the low energy doublet in the nanowire results from the combination of a non-degenerate electron–hole pair, which is a natural precursor for a Majorana pair. Importantly, this information cannot be directly obtained from the DC current. Importantly, this protocol requires measuring the cavity response and the dc current through the tunnel probes simultaneously. Although the spectroscopic measurement described above is probably the most straightforward measurement to perform with a cavity, many other effects are expected by combining Majorana fermions and cavities. Hence, the direct electric coupling between Majorana bound states and cavity photons has raised a lot of attention recently [44–48]. The indirect coupling of Majorana fermions to cavities through a superconducting quantum bit also raises interest for quantum computation purposes [188–196].

## 6. Conclusion and perspectives

In this review, we have shown that a microwave cavity represents a powerful tool to investigate the properties and dynamics of electrons in a hybrid nanocircuit. In the linear-coupling regime, the microwave cavity gives access to the charge susceptibility of the nanocircuit, which can be used to understand most mesoscopic QED experiments realized so far. First, many different types of electronic degrees of freedom can be coupled coherently or strongly to cavity photons. In particular, we have reviewed several promising experiments in which cavity photons are strongly or coherently coupled to the charge [30–32] or spin [34] of a double dot or Andreev states [35] in an atomic contact. The investigation of the coherent dynamics of these degrees of freedom now seems accessible [35]. Second, microwave cavities give new access to the tunneling dynamics of electrons between a dot and fermionic reservoirs. In equilibrium conditions, the charge relaxation dynamics caused by a fermionic reservoir can be studied with a high sensitivity. A first experiment seems consistent with a non-interacting theory which suggests the universality of the charge relaxation resistance in the adiabatic regime [37]. However, further study is required in the interacting case, where a rich phenomenology is expected. In out-of-equilibrium conditions, there exists several means to obtain photon emission, by using inelastic tunneling between a quantum dot and a reservoir with an energy-dependent DOS [37], or by using inelastic tunneling between two different quantum dots [38–41]. It was possible to obtain the lasing emission of a coherent photon field by coupling several voltage-biased double dots to a microwave cavity [40]. Finally, mesoscopic QED represents a new tool to study exotic condensed matter states, as shown by a recent experiment for a quantum dot in the Kondo regime [167]. Recent theory proposals also suggest to study split Cooper pairs [42, 43] and Majorana bound states with a microwave cavity [44–49].

One interesting feature of mesoscopic QED is that many geometries can be realized thanks to the versatility of nanofabrication techniques. Furthermore, many different experimental

protocols are possible thanks to the control on the nanocircuit dc bias and the microwave supply and detection. Therefore many situations can be investigated. There are many possible research directions in continuation of the works mentioned in this review:

- Most of the experiments performed so far have been realized with a large number of photons, i.e.  $\langle \hat{a}^\dagger \hat{a} \rangle > 10$ , such that a semiclassical description of the cavity response is sufficient to understand the measurements. The  $\langle \hat{a}^\dagger \hat{a} \rangle \sim 1$  regime has been used very recently for the study of the strong nanocircuit/cavity coupling, in the stationary regime where the cavity response versus the excitation frequency shows a characteristic splitting [30–32]. Many other quantum phenomena are expected for  $\langle \hat{a}^\dagger \hat{a} \rangle \sim 1$ , especially in the time domain, by analogy with circuit QED experiments with superconducting quantum bits, and beyond if quantum transport to the reservoirs is involved. It is one of the main goals of mesoscopic QED to explore this possibility.
- The nonlinear regime, where multi-photon emission or absorption by the nanocircuit is possible, is a particularly interesting regime [156], [217–219]. This regime can be obtained by increasing the amplitude of the cavity microwave drive or the intensity of the light–matter interaction.
- In this review, we have essentially discussed how to use a microwave cavity to characterize the properties of a nanocircuit. One could also study how to use a nanocircuit to prepare non-classical photonic states other than the coherent field already obtained through the lasing effect [133]. For instance, squeezed cavity states can be prepared using a non-linear light–matter interaction [47, 197]. In this context, cavity state tomography and photon statistics would represent important quantities to explore [198]. So far, the cavity state tomography has been performed only in the presence of two double quantum dots in the lasing regime [40].
- Placing several nanocircuits in a microwave cavity would enable one to study a large variety of effects involving interaction between nanocircuits mediated by cavity photons [199–203]. First experiments have already been realized with carbon nanotubes and graphene [54, 97, 122].
- One could go further in the hybridization of devices by coupling both a quantum dot circuit and a superconducting quantum bit to a microwave cavity [204, 205]. The use of the superconducting quantum bit could, for instance, give further access to the electronic dynamics in the nanocircuit.
- Finally, it would be interesting to transpose mesoscopic QED to other types of cavities. First, one could imagine coupling nanocircuits to terahertz cavities. This would give photonic access to other energy scales, such as the charging energy of a Coulomb blockaded quantum dot. Second, the behavior of quantum dot circuits coupled to optical cavities is discussed theoretically in [206–215]. The fabrication of such devices is extremely challenging, but this could reveal effects related to the polarization of light. With the coplanar cavities considered in this review, these effects are irrelevant because the microwave field profile is set by the shape of the microwave cavity.

To conclude, mesoscopic QED experiments open a new avenue to investigate light–matter interaction under a different perspective. Many research directions are possible for the future development of this field.

## Acknowledgments

We would like to thank François Mallet and Zaki Leghtas for fruitful discussions. This work was financed by the ERC Starting grant CirQys and the EU FP7 Project No. SE2ND[271554].

## Appendix A. Nanocircuit charge susceptibility with the Keldysh formalism

In this appendix, we show how to predict the charge dynamics of a generic nanocircuit which encloses a nanoconductor, assuming that the coupling of the nanocircuit reservoirs to the cavity electric field can be disregarded. The nanoconductor can be decomposed into  $N$  sites with an index  $n$  or  $m$ . For the sake of generality, we do not specify the Hamiltonian  $\hat{H}_0^t$  of the nanocircuit, which is expressed in terms of electronic creation and annihilation operators  $c_{n\sigma}^\dagger$  and  $c_{n\sigma}$  for an electron with spin  $\sigma$  in site  $n$ . In the semiclassical limit and in the framework of the resonant approximation of section 3.2.1, one can use an Hamiltonian ac excitation term

$$H_{ac}(t) = \sum_{n,\sigma} g_n c_{n\sigma}^\dagger c_{n\sigma} \bar{a} e^{-i\omega_{RF}t} \quad (\text{A.1})$$

to account for the semiclassical drive of the nanocircuit by cavity photons. In the Keldysh formalism, the dynamics of the nanocircuit can be described by using retarded, advanced, and lesser Green's functions  $G^c(\omega)$  with  $(\alpha \in \{r, a, <\})$  [216]. These Green's function have a matrix structure which encloses  $N \times N$  site sub-blocks  $G^{nm,c}(\omega)$  whose structure depends on the problem considered. For instance, in the presence of superconductivity and a single spin quantization axis, one can use Green's functions with the Nambu structure:

$$G^{nm,\alpha} = \begin{bmatrix} G_{c_{n\uparrow},c_{m\uparrow}}^\alpha & G_{c_{n\uparrow},c_{m\downarrow}}^\alpha \\ G_{c_{n\downarrow},c_{m\uparrow}}^\alpha & G_{c_{n\downarrow},c_{m\downarrow}}^\alpha \end{bmatrix} \quad (\text{A.2})$$

with

$$G_{BA}^r(t) = -i\theta(t) \langle \{B(t), A(t=0)\} \rangle \quad (\text{A.3})$$

$$G_{BA}^a(t) = i\theta(-t) \langle \{B(t), A(t=0)\} \rangle \quad (\text{A.4})$$

$$G_{BA}^<(t) = i \langle B(t=0)A(t) \rangle. \quad (\text{A.5})$$

Here, one must calculate the statistical average  $\langle \rangle$  using the time-dependent Hamiltonian  $\hat{H}_0^t + H_{ac}(t)$ . Since  $\langle c_{n\sigma}^\dagger(t)c_{n\sigma}(t) \rangle = -iG_{c_{n\sigma},c_{n\sigma}}^<(t,t)$ , one can obtain the nanocircuit charge response by calculating  $G^<(t,t)$ . Below, we perform this calculation at first order in  $\bar{a}$  in order to obtain the

linear charge susceptibility of the nanocircuit. The first order perturbation theory in  $\bar{a}$  gives

$$G^{r(a)}(t,t') = \mathcal{G}^{r(a)}(t,t') + \int dt_2 \mathcal{G}^{r(a)}(t,t_2) \hat{E}_{ac}(t_2) \mathcal{G}^{r(a)}(t_2,t') \quad (\text{A.6})$$

with

$$\hat{E}_{ac}(t) = \bar{a} \sum_n g_n \hat{\tau}_n e^{-i\omega_{RF}t}. \quad (\text{A.7})$$

Here,  $\mathcal{G}^{r(a)}(t,t')$  is the Green's function solution of the problem for  $\bar{a} = 0$ . Examples of expressions of  $\mathcal{G}^{r(a)}$  are given in sections 5.2 and 5.3. The matrix  $\hat{\tau}_n$  is a diagonal matrix which corresponds to  $\text{diag}(g_n, -g_n)$  in the orbital block  $(n,n)$  and is zero otherwise. The combination of equations (A.6) and (A.7) gives

$$G^{r(a)}(t,t') = \int \frac{d\omega}{2\pi} e^{-i\omega(t-t')} \mathcal{G}^{r(a)}(\omega) \left( 1 + \hat{\tau} \mathcal{G}^{r(a)}(\omega - \omega_{RF}) e^{-i\omega_{RF}t} \right). \quad (\text{A.8})$$

From the Langreth theorem [216] one has

$$G^<(t,t') = \int \int dt_1 dt_2 G^r(t,t_1) \Sigma^<(t_1,t_2) G^a(t_2,t') \quad (\text{A.9})$$

with

$$\Sigma^<(t_1,t_2) = \int \frac{d\omega}{2\pi} e^{-i\omega'(t_1-t_2)} \Sigma^<(\omega). \quad (\text{A.10})$$

The smaller self energy  $\Sigma^<(\omega)$  of the discrete levels due to the presence of the reservoirs can be expressed by following standard Keldysh rules (see e.g. section 5.2 and [37] for examples). By combining equations (A.6) and (A.9), in the non-interacting case, one gets at first order in  $\bar{a}$ :

$$G^<(t,t) = \int \frac{d\omega}{2\pi} \mathcal{D}(\omega) + \bar{a} e^{-i\omega_{RF}t} \sum_n \int \frac{d\omega}{2\pi} \mathcal{G}^r(\omega) g_n \hat{\tau}_n \mathcal{D}(\omega + \omega_{RF}) + \bar{a} e^{-i\omega_{RF}t} \sum_n \int \frac{d\omega}{2\pi} \mathcal{D}(\omega) g_n \hat{\tau}_n \mathcal{G}^a(\omega + \omega_{RF}) \quad (\text{A.11})$$

with

$$\mathcal{D}(\omega) = \mathcal{G}^r(\omega) \Sigma^<(\omega) \mathcal{G}^a(\omega). \quad (\text{A.12})$$

One can identify the charge susceptibility  $\chi_{nm}(\omega_0)$  of site  $n$  in response to an excitation at site  $m$  by comparing the equation

$$Q_n(t) = ie \text{Tr}[\hat{\tau}_n G^<(t,t)] - e \quad (\text{A.13})$$

which is due to the definition of  $G^<$  and the equation

$$Q_n(t) = \bar{Q}_n - e \sum_m \bar{a} g_m e^{-i\omega_{RF}t} (\chi_{nm}(\omega_{RF})) \quad (\text{A.14})$$

which defines  $\chi_{nm}$ , with  $\bar{Q}_n$  the average charge in dot  $n$ . In equation (A.13), the  $-e$  term is due to the fact that the Greens functions are defined in the Nambu space in the particular case of equation (A.2). Using the cyclic invariance of the trace, one finds

$$\begin{aligned} \chi_{nm}(\omega_{\text{RF}}) = & -i \int \frac{d\omega}{2\pi} \text{Tr}[\hat{\tau}_n \mathcal{G}^r(\omega + \omega_{\text{RF}}) \hat{\tau}_m \mathcal{D}(\omega)] \\ & - i \int \frac{d\omega}{2\pi} \text{Tr}[\hat{\tau}_m \mathcal{G}^a(\omega - \omega_{\text{RF}}) \hat{\tau}_n \mathcal{D}(\omega)]. \end{aligned} \quad (\text{A.15})$$

This leads to equation (67) of the main text, with  $\hat{T} = \sum_n g_n \hat{\tau}_n$ . Note that a similar derivation can be performed without using the Nambu space in the case of a problem without superconductivity, or by using an extended Nambu space if the nanocircuit includes non-homogeneous magnetic fields which induce spin rotations (see [49]). In this case, equation (67) still holds provided the matrix  $\hat{T}$  is defined consistently with the structure of the Green's functions.

## Appendix B. Non-interacting double dot with the Keldysh non-interacting description

In this appendix, we show in the simple example of a non-interacting double quantum dot with two grounded normal metal reservoirs (see figure 7) that the Keldysh approach of section 5.1 leads to a nanocircuit charge susceptibility  $\Xi(\omega)$  which can account simultaneously for internal transitions inside a nanoconductor, and tunneling between the nanoconductor and fermionic reservoirs. For simplicity, we disregard the spin degree of freedom. The double dot Hamiltonian is

$$\begin{aligned} \hat{H}_0 = & \varepsilon_L \hat{c}_L^\dagger \hat{c}_L + \varepsilon_R \hat{c}_R^\dagger \hat{c}_R + t \hat{c}_L^\dagger \hat{c}_R + t^* \hat{c}_R^\dagger \hat{c}_L \\ & + \sum_{\alpha \in \{L,R\}} \varepsilon_{\alpha k} \hat{c}_{\alpha k}^\dagger \hat{c}_{\alpha k} + t_N \left( \hat{c}_{\alpha k}^\dagger \hat{c}_\alpha + \hat{c}_\alpha^\dagger \hat{c}_{\alpha k} \right). \end{aligned} \quad (\text{B.1})$$

Here,  $\hat{c}_\alpha^\dagger$  is the creation operator for an electron in the dot  $\alpha \in \{L, R\}$ . The operator  $\hat{c}_{\alpha k}^\dagger$  creates an electron in the state  $k$  of the normal metal reservoir attached to dot  $\alpha$ . We note  $t$  the interdot hopping, and  $t_N$  the tunnel hopping constant between dot  $\alpha$  and its reservoir. The double dot Green's function can be defined as

$$G^c = \begin{bmatrix} G_{c_L, c_L^\dagger}^c & G_{c_L, c_R^\dagger}^c \\ G_{c_R, c_L^\dagger}^c & G_{c_R, c_R^\dagger}^c \end{bmatrix}. \quad (\text{B.2})$$

Therefore, using the Keldysh description of nanocircuits [216], one gets from equation (B.1)

$$\mathcal{G}^r(\omega) = \begin{bmatrix} \omega - \varepsilon_L + i\frac{\Gamma_N}{2} & t \\ t & \omega - \varepsilon_R - i\frac{\Gamma_N}{2} \end{bmatrix}^{-1} \quad (\text{B.3})$$

and

$$\check{\Sigma}^<(\omega) = i\Gamma_N f(\omega) \check{1} \quad (\text{B.4})$$

with  $\Gamma_N = 2\pi |t_N|^2$  and  $f(\omega) = 1/(1 + \exp[\omega/k_B T])$ . Then, equation (67) gives

$$\Xi(\omega) = \sum_s \int_{-\infty}^{+\infty} d\varepsilon \left( \frac{2\Gamma_N f(\varepsilon) (\mathcal{F}_{t,s}(\omega) + \mathcal{F}_{l,s}(\omega))}{\pi [(\varepsilon - E_s)^2 + (\frac{\Gamma_N}{2})^2]} \right) \quad (\text{B.5})$$

with

$$E_\pm = \frac{1}{2} \left[ \varepsilon_L + \varepsilon_R \pm \sqrt{(\varepsilon_L - \varepsilon_R)^2 + 4t^2} \right] \quad (\text{B.6})$$

$$\mathcal{F}_{t,s}(\omega) = \frac{g_t^2 (\varepsilon - E_{-s})}{(\varepsilon - E_{-s})^2 - (\omega + i\frac{\Gamma_N}{2})^2} \quad (\text{B.7})$$

and

$$\mathcal{F}_{l,s}(\omega) = \frac{g_{l,s}^2 (\varepsilon - E_s)}{(\varepsilon - E_s)^2 - (\omega + i\frac{\Gamma_N}{2})^2}. \quad (\text{B.8})$$

Here,  $g_t$  is defined by equation (53) of the main text and one has

$$g_{l,s} = \frac{\lambda_L + \lambda_R}{2} + s \frac{\lambda_L - \lambda_R}{2} \frac{\varepsilon_L - \varepsilon_R}{E_+ - E_-}. \quad (\text{B.9})$$

Equation (B.5) is similar to equation (15) of [85], obtained with a non-interacting diagrammatic approach. An inspection of the double dot Hamiltonian in the bonding/antibonding state basis reveals that  $g_t$  corresponds to the transverse coupling between the bonding/antibonding transition and the cavity, whereas  $g_{l,+}$  and  $g_{l,-}$  correspond to the lever arms for the modulation of the bonding and antibonding energy levels by the cavity electric field. The complex expression (B.5) can be simplified in some particular limits to get a better physical insight. First, in the limit  $\omega < \Gamma_N \ll k_B T \ll t$ , one gets, from equation (B.5)

$$\Xi(\omega = 0) \simeq -\frac{\beta}{4} \sum_s \left( \frac{g_{l,s}^2}{\cosh^2[\frac{\beta E_s}{2}]} - 2g_t^2 \frac{f(E_-) - f(E_+)}{\Delta_c} \right). \quad (\text{B.10})$$

Hence, the terms in  $g_{l,s}$  describe a quantum capacitance contribution which is due to the thermal equilibration of the bonding and antibonding states with the reservoirs. The term in  $g_t$  describes another quantum capacitance contribution which is due to a transfer of electrons between the bonding and antibonding states of the double dot. This last term is maximally visible when the double dot has an occupation close to one electron, i.e.  $f(E_-) = 1$  and  $f(E_+) = 0$ . Second, in the limit  $\omega \simeq E_+ - E_-$  and  $2t \gg \Gamma_N$ , one gets

$$\Xi(\omega) = g_t^2 \frac{f(E_-) - f(E_+)}{\omega - E_+ - E_-} \quad (\text{B.11})$$

which is similar to equation (58) of the main text, with  $p_- = f(E_-)$  and  $p_+ = f(E_+)$ . These values of  $p_+$  and  $p_-$  stem from the fact that in the above lines, for simplicity, we have assumed that the normal metal reservoirs are grounded. Therefore, the population of the double dot states is thermal. It would be possible to generalize straightforwardly the above approach to the non-equilibrium case by using a term  $\check{\Sigma}^<(\omega)$  which would depend on the bias voltage. Note that in [49] discussed in section 5.5.3, it is also found that the charge susceptibility  $\Xi(\omega)$  for a Majorana nanowire accounts for both tunneling to normal metal reservoirs (see figure 18(c), step highlighted with magenta dots) and transitions internal to the nanowire (see figure 18(c), resonance highlighted with black dots).

## References

- [1] van Wees B J, van Houten H, Beenakker C W J, Williamson J G, Kouwenhoven L P, van der Marel D and Foxon C T 1988 *Phys. Rev. Lett.* **60** 848
- [2] Krans J M, Van Ruitenbeek J M, Fisun V V, Yanson I K and De Jongh L J 1995 *Nature* **375** 767
- [3] Kouwenhoven L P, Marcus C M, McEuen P L, Tarucha S, Westervelt R M and Wingreen N S 1997 *Mesoscopic Electron Transport (Series E: Applied Sciences vol 345)* ed L L Sohn *et al* (Dordrecht: Kluwer) p 105
- [4] Shulman M D, Dial O E, Harvey S P, Bluhm H, Umansky V and Yacoby A 2012 *Science* **13** 202
- [5] Klein D L, Roth R, Lim A K L, Alivisatos A P and McEuen P L 1997 *Nature* **389** 699
- [6] Tans S J, Devoret M H, Dai H, Thess A, Smalley R E, Geeligs B L and Dekker C 1997 *Nature* **397** 474
- [7] De Franceschi S, van Dam J A, Bakkers E P A M, Feiner L F, Gurevich L and Kouwenhoven L P 2003 *Appl. Phys. Lett.* **83** 344
- [8] Cottet A, Kontos T, Sahoo S, Man H T, Choi M-S, Belzig W, Bruder C, Morpurgo A F and Schönenberger C 2006 *Semicond. Sci. Technol.* **21** S78
- [9] Cottet A and Kontos T 2010 *Phys. Rev. Lett.* **105** 160502
- [10] Recher P, Sukhorukov E V and Loss D 2001 *Phys. Rev. B* **63** 165314
- [11] Leijnse M and Flensberg K 2012 *Semicond. Sci. Technol.* **27** 124003
- [12] Kouwenhoven L P, Jauhar S, McCormick K, Dixon D, McEuen P L, Nazarov Yu V, van der Vaart N C and Foxon C T 1994 *Phys. Rev. B* **50** 2019
- [13] Oosterkamp T H, Fujisawa T, van der Wiel W G, Ishibashi K, Hijman R V, Tarucha S and Kouwenhoven L P 1998 *Nature* **395** 873
- [14] Elzerman J M, De Franceschi S, Goldhaber-Gordon D, van der Wiel W G and Kouwenhoven L P 2000 *J. Low Temp. Phys.* **118** 375
- [15] Schoelkopf R J, Wahlgren P, Kozhevnikov A A, Delsing P and Prober D E 1998 *Science* **280** 1238
- [16] Fujisawa T and Hirayama Y 2000 *Japan. J. Appl. Phys.* **39** 2338
- [17] Cassidy M C, Dzurak A S, Clark R G, Petersson K D, Farrer I, Ritchie D A and Smith C G 2007 *Appl. Phys. Lett.* **91** 222104
- [18] Reilly D J, Marcus C M, Hanson M P and Gossard A C 2007 *Appl. Phys. Lett.* **91** 162101
- [19] Ota T, Hayashi T, Muraki K and Fujisawa T 2010 *Appl. Phys. Lett.* **96** 032104
- [20] Petersson K D, Smith C G, Anderson D, Atkinson P, Jones G A C and Ritchie D A 2010 Charge and spin state readout of a double quantum dot coupled to a resonator *Nano Lett.* **10** 2789
- [21] Chorley S J, Wabnig J, Penfold-Fitch Z V, Petersson K D, Frake J, Smith C G and Buitelaar M R 2012 *Phys. Rev. Lett.* **108** 036802
- [22] Hayashi T, Fujisawa T, Cheong H D, Jeong Y H and Hirayama Y Y 2003 *Phys. Rev. Lett.* **91** 226804
- [23] Koppens F H L, Buizert C, Tielrooij K J, Vink I T, Nowack K C, Meunier T, Kouwenhoven L P and Vandersypen L M K 2006 *Nature* **442** 766
- [24] Nowack K C, Koppens F H L, Nazarov Yu V and Vandersypen L M K 2007 *Science* **318** 1430
- [25] Raimond J M, Brune M and Haroche S 2001 *Rev. Mod. Phys.* **73** 565
- [26] Wallraff A, Schuster D I, Blais A, Frunzio L, Huang R, Majer J, Kumar S, Girvin S M and Schoelkopf R J 2004 *Nature* **431** 162
- [27] Paik H *et al* 2011 *Phys. Rev. Lett.* **107** 240501
- [28] Imamoglu A, Awschalom D D, Burkard G, DiVincenzo D P, Loss D and Small S M 1999 *Phys. Rev. Lett.* **83** 4204
- [29] Burkard G and Imamoglu A 2006 *Phys. Rev. B* **74** 041307
- [30] Mi X, Cady J V, Zajac D M, Stehlik J, Edge L F and Petta J R 2017 *Science* **355** 156
- [31] Bruhat L E, Cubaynes T, Viennot J J, Dartiailh M C, Desjardins M M, Cottet A and Kontos T 2017 arXiv:1612.05214
- [32] Stockklauser A, Scarlino P, Koski J, Gasparinetti S, Kraglund Andersen C, Reichl C, Wegscheider W, Ihn T, Ensslin K and Wallraff A 2017 *Phys. Rev. X* **7** 011030
- [33] Mi X, Cady J V, Zajac D M, Stehlik J, Edge L F and Petta J R 2017 *Appl. Phys. Lett.* **110** 043502
- [34] Viennot J J, Dartiailh M C, Cottet A and Kontos T 2015 *Science* **349** 408
- [35] Janvier C *et al* 2015 *Science* **349** 1199
- [36] Viennot J J, Delbecq M R, Dartiailh M C, Cottet A and Kontos T 2014 *Phys. Rev. B* **89** 165404
- [37] Bruhat L E, Viennot J J, Dartiailh M C, Desjardins M M, Kontos T and Cottet A 2016 *Phys. Rev. X* **6** 021014
- [38] Stockklauser A, Maisi V F, Basset J, Cujia K, Reichl C, Wegscheider W, Ihn T, Wallraff A and Ensslin K 2015 *Phys. Rev. Lett.* **115** 046802
- [39] Liu Y Y, Petersson K D, Stehlik J, Taylor J M and Petta J R 2014 *Phys. Rev. Lett.* **113** 036801
- [40] Liu Y-Y, Stehlik J, Eichler C, Gullans M J, Taylor J M and Petta J R 2015 *Science* **347** 285
- [41] Liu Y-Y, Stehlik J, Gullans M J, Taylor J M and Petta J R 2015 *Phys. Rev. A* **92** 053802
- [42] Cottet A, Kontos T and Levy Yeyati A 2012 *Phys. Rev. Lett.* **108** 166803
- [43] Cottet A 2014 *Phys. Rev. B* **90** 125139
- [44] Trif M and Tserkovnyak Y 2012 *Phys. Rev. Lett.* **109** 257002
- [45] Schmidt T L, Nunnenkamp A and Bruder C 2013 *Phys. Rev. Lett.* **110** 107006
- [46] Schmidt T L, Nunnenkamp A and Bruder C 2013 *New J. Phys.* **15** 025043
- [47] Cottet A, Kontos T and Douçot B 2013 *Phys. Rev. B* **88** 195415
- [48] Dmytruk O, Trif M and Simon P 2015 *Phys. Rev. B* **92** 245432
- [49] Dartiailh M, Kontos T, Douçot M and Cottet A 2017 *Phys. Rev. Lett.* **118** 126803
- [50] Childress L, Sørensen A S and Lukin M D 2004 *Phys. Rev. A* **69** 042302
- [51] Frey T, Leek P J, Beck M, Ensslin K, Wallraff A and Ihn T 2011 *Appl. Phys. Lett.* **98** 262105
- [52] Toida H, Nakajima T and Komiyama S 2012 *Phys. Rev. Lett.* **110** 066802
- [53] Schmidt A R *et al* 2014 *J. Appl. Phys.* **116** 044503
- [54] Delbecq M R, Schmitt V, Parmentier F D, Roch N, Viennot J J, Fève G, Huard B, Mora C, Cottet A and Kontos T 2011 *Phys. Rev. Lett.* **107** 256804
- [55] Ranjan V, Puebla-Hellmann G, Jung M, Hasler T, Nunnenkamp A, Muoth M, Hierold C, Wallraff A and Schönenberger C 2015 *Nat. Commun.* **6** 7165
- [56] Petersson K D, McFaul L W, Schroer M D, Jung M, Taylor J M, Houck A A and Petta J R 2012 *Nature* **490** 380
- [57] Larsen T W, Petersson K D, Kuemmeth F, Jespersen T S, Krogstrup P, Nygard J and Marcus C M 2015 *Phys. Rev. Lett.* **115** 127001
- [58] de Lange G, van Heck B, Bruno A, van Woerkom D J, Geresdi A, Plissard S R, Bakkers E P A M, Akhmerov A R and DiCarlo L 2015 *Phys. Rev. Lett.* **115** 127002
- [59] Wang R, Deacon R S, Car D, Bakkers E P A M and Ishibashi K 2016 *Appl. Phys. Lett.* **108** 203502

- [60] Zhang M-L *et al* 2014 *Appl. Phys. Lett.* **105** 073510
- [61] Crisan A D, Datta S, Viennot J J, Delbecq M R, Cottet A and Kontos T 2016 *Nat. Commun.* **7** 10451
- [62] Waissman J, Honig M, Pecker S, Benyamini A, Hamo A and Ilani S 2013 *Nat. Nanotechnol.* **8** 569
- [63] Viennot J J, Palomo J and Kontos T 2014 *Appl. Phys. Lett.* **104** 113108
- [64] Stehlik J, Liu Y-Y, Quintana C M, Eichler C, Hartke T R and Petta J R 2015 *Phys. Rev. Appl.* **4** 014018
- [65] Samkharadze N, Bruno A, Scarlino P, Zheng G, DiVincenzo D P, DiCarlo L and Vandersypen L M K 2016 *Phys. Rev. Appl.* **5** 044004
- [66] Köpke M and Weis J 2014 *Physica C* **506** 143
- [67] Götz K J G, Blien S, Stiller P L, Vavra O, Mayer T, Huber T, Meier T N G, Kronseder M, Strunk Ch and Hüttel A K 2016 *Nanotechnology* **27** 135202
- [68] Blien S, Götz K J G, Stiller P L, Mayer T, Huber T, Vavra O and Hüttel A K 2016 *Phys. Status Solidi B* **253** 2385
- [69] Fert A 2008 *Rev. Mod. Phys.* **80** 1517
- [70] Cottet A, Kontos T, Belzig W, Schönenberger C and Bruder C 2006 *Europhys. Lett.* **74** 320
- [71] Bertrand B, Flentje H, Takada S, Yamamoto M, Tarucha S, Ludwig A, Wieck A D, Bäuerle C and Meunier T 2015 *Phys. Rev. Lett.* **115** 096801
- [72] Reed M D *et al* 2016 *Phys. Rev. Lett.* **116** 110402
- [73] Martins F, Malinowski F K, Nissen P D, Barnes E, Fallahi S, Gardner G C, Manfra M J, Marcus C M and Kuemmeth F 2016 *Phys. Rev. Lett.* **116** 116801
- [74] Loss D and DiVincenzo D P 1998 *Phys. Rev. A* **57** 120
- [75] Cohen-Tannoudji C, Dupont-Roc J and Grynberg G 1997 *Photons and Atoms: Introduction to Quantum Electrodynamics* (New York: Wiley)
- [76] Blais A, Huang R-S, Wallraff A, Girvin S M and Schoelkopf R J 2004 *Phys. Rev. A* **69** 062320
- [77] Nigg s E, Paik H, Vlastakis B, Kirchmair G, Shankar S, Frunzio L, Devoret M H, Schoelkopf R J and Girvin S M 2012 *Phys. Rev. Lett.* **108** 240502
- [78] Solgun F, Abraham D W and DiVincenzo D P 2014 *Phys. Rev. B* **90** 134504
- [79] Vukics A, Grießer T and Domokos P 2014 *Phys. Rev. Lett.* **112** 073601
- [80] Cottet A, Kontos T and Douçot B 2015 *Phys. Rev. B* **91** 205417
- [81] Prange R E 1963 *Phys. Rev.* **131** 1083
- [82] Reulet B, Ramin M, Bouchiat H and Mailly D 1995 *Phys. Rev. Lett.* **75** 124
- [83] Deblock R, Noat Y, Bouchiat H, Reulet B and Mailly D 2000 *Phys. Rev. Lett.* **84** 5379
- [84] Walls D F and Milburn G J 2008 *Quantum Optics* 2nd edn (Berlin: Springer)
- [85] Cottet A, Mora C and Kontos T 2011 *Phys. Rev. B* **83** 121311
- [86] Thompson R J, Rempé G and Kimble H J 1992 *Phys. Rev. Lett.* **68** 1132
- [87] Brune M, Schmidt-Kaler F, Maali A, Dreyer J, Hagley E, Raimond J M and Haroche S 1996 *Phys. Rev. Lett.* **76** 1800
- [88] Reithmaier J P, Sęk G, Löffler A, Hofmann C, Kuhn S, Reitzenstein S, Keldysh L V, Kulakovskii V D, Reinecke T L and Forchel A 2004 *Nature* **432** 197
- [89] Yoshie T, Scherer A, Hendrickson J, Khitrova G, Gibbs H M, Rupper G, Ell C, Shchekin O B and Deppe D G 2004 *Nature* **432** 200
- [90] Frey T, Leek P J, Beck M, Blais A, Ihn T, Ensslin K and Wallraff A 2012 *Phys. Rev. Lett.* **108** 046807
- [91] Schroer M D, Jung M, Petersson K D and Petta J R 2012 *Phys. Rev. Lett.* **109** 166804
- [92] Frey T, Leek P J, Beck M, Faist J, Wallraff A, Ensslin K, Ihn T and Büttiker M 2012 *Phys. Rev. B* **86** 115303
- [93] Delbecq M R, Bruhat L E, Viennot J J, Datta S, Cottet A and Kontos T 2013 *Nat. Commun.* **4** 1400
- [94] Toida H, Nakajima T and Komiyama S 2013 *Phys. Rev. Lett.* **110** 066802
- [95] Basset J, Jarausch D-D, Stockklauser A, Frey T, Reichl C, Wegscheider W, Ihn T M, Ensslin K and Wallraff A 2013 *Phys. Rev. B* **88** 125312
- [96] Basset J, Stockklauser A, Jarausch D-D, Frey T, Reichl C, Wegscheider W, Wallraff A, Ensslin K and Ihn T 2014 *Appl. Phys. Lett.* **105** 063105
- [97] Deng G-W *et al* 2015 *Nano Lett.* **15** 6620
- [98] Deng G-W *et al* 2015 *Phys. Rev. Lett.* **115** 126804
- [99] Cottet A, Vion V, Joyez P, Aassime A, Esteve D and Devoret M H 2002 *Physica C* **367** 197
- [100] Stehlik J, Liu Y-Y, Eichler C, Hartke T R, Mi X, Gullans M J, Taylor J M and Petta J R 2016 Double quantum dot floquet gain medium *Phys. Rev. X* **6** 041027
- [101] Petersson K D, Petta J R, Lu H and Gossard A C 2010 *Phys. Rev. Lett.* **105** 246804
- [102] Freeman B M, Schoenfeld J S and Jiang H 2016 *Appl. Phys. Lett.* **108** 253108
- [103] Obata T, Takeda K, Kamioka J, Kodera T, Akhtar W M, Sawano K, Oda S, Shiraki Y and Tarucha S 2014 *JPS Conf. Proc.* **1** 012030
- [104] Schuster D I *et al* 2010 *Phys. Rev. Lett.* **105** 140501
- [105] Kubo Y *et al* 2010 *Phys. Rev. Lett.* **105** 140502
- [106] Zhu X *et al* 2011 *Nature* **478** 221
- [107] Tosi G, Mohiyaddin F A, Huebl H and Morello A 2014 *AIP Adv.* **4** 087122
- [108] Haikka P, Kubo Y, Bienfait A, Bertet P and Moelmer K 2017 *Phys. Rev. A* **95** 022306
- [109] Trif M, Golovach V N and Loss D 2008 *Phys. Rev. B* **77** 045434
- [110] Xuedong H, Yu-Xi L and Franco N 2012 *Phys. Rev. B* **86** 035314
- [111] Kloeffel C, Trif M, Stano P and Loss D 2013 *Phys. Rev. B* **88** 241405
- [112] Beaudoïn F, Lachance-Quirion D, Coish W A and Pioro-Ladrière M 2016 *Nanotechnology* **27** 464003
- [113] Khaetskii V and Nazarov Yu V 2000 *Phys. Rev. B* **61** 12639
- [114] Khaetskii V and Nazarov Yu V 2001 *Phys. Rev. B* **64** 125316
- [115] Erlingsson S I and Nazarov Yu V 2002 *Phys. Rev. B* **66** 155327
- [116] Tokura Y, van der Wiel W G, Obata T and Tarucha S 2006 *Phys. Rev. Lett.* **96** 047202
- [117] Takeda K *et al* 2016 *Sci. Adv.* **2** e1600694
- [118] Ono K, Austing D G, Tokura Y and Tarucha S 2002 *Science* **297** 1313
- [119] Pei-Qing J, Marthaler M, Shnirman A and Schön G 2012 *Phys. Rev. Lett.* **108** 190506
- [120] Pei-Qing J, Jeske J, Greentree A D and Cole J H 2015 arXiv:1507.07198
- [121] Wang L, Tu T, Gong B and Guo G-C 2015 *Phys. Rev. A* **92** 062346
- [122] Tian-Yi H, Guang-Wei D, Wei D and Guo-Ping G 2016 *Chin. Phys. Lett.* **33** 47301
- [123] Russ M and Burkard G 2015 *Phys. Rev. B* **92** 205412
- [124] Srinivasa V, Taylor J M and Tahan C 2016 *Phys. Rev. B* **94** 205421
- [125] Russ M, Ginzler F and Burkard G 2016 *Phys. Rev. B* **94** 165411
- [126] Sköldbberg J, Löfwander T, Shumeiko V S and Fogelström M 2008 *Phys. Rev. Lett.* **101** 087002
- [127] Koch J, Yu T M, Gambetta J, Houck A A, Schuster D I, Majer J, Blais A, Devoret M H, Girvin S M and Schoelkopf R J 2007 *Phys. Rev. A* **76** 04319
- [128] Burkard G and Petta J R 2016 *Phys. Rev. B* **94** 195305
- [129] Mi X, Peterfalvi C G, Burkard G and Petta J R 2017 arXiv:1704.06312
- [130] Chirla R, Manolescu A and Moca C P 2016 *Phys. Rev. B* **93** 155110

- [131] Schuetz M J A, Giedke G, Vandersypen L M K and Cirac J I 2017 *Phys. Rev. A* **95** 052335
- [132] Canran X and Vavilov M G 2013 *Phys. Rev. B* **87** 035429
- [133] Schiró M and Le Hur K 2014 *Phys. Rev. B* **89** 195127
- [134] Härtle R and Kulkarni M 2015 *Phys. Rev. B* **91** 245429
- [135] Wong C H and Vavilov M G 2017 *Phys. Rev. A* **95** 012325
- [136] Cirio M, De Liberato S, Lambert N and Nori F 2016 *Phys. Rev. Lett.* **116** 113601
- [137] Dmytruk O, Trif M, Mora C and Simon P 2016 *Phys. Rev. B* **93** 075425
- [138] Agarwalla B K, Kulkarni M, Mukamel S and Segal D 2016 *Phys. Rev. B* **94** 035434
- [139] Agarwalla B K, Kulkarni M, Mukamel S and Segal D 2016 *Phys. Rev. B* **94** 121305
- [140] Gabelli J, Fève G, Berroir J M, Plaçais B, Cavanna A, Etienne B, Jin Y and Glattli D C 2006 *Science* **313** 499
- [141] Nigg S, Lopez R and Büttiker M 2006 *Phys. Rev. Lett.* **97** 206804
- [142] Mora C and Le Hur K 2010 *Nat. Phys.* **6** 697
- [143] Hamamoto Y, Jonckheere T, Kato T and Martin T 2010 *Phys. Rev. B* **81** 153305
- [144] Filippone M, Le Hur K and Mora C 2011 *Phys. Rev. Lett.* **107** 176601
- [145] Alomar M I, Lim J S and Sánchez D 2016 *Phys. Rev. B* **94** 165425
- [146] Büttiker M, Thomas H and Prêtre A 1993 *Phys. Lett. A* **180** 364
- [147] Prêtre A, Thomas H and Büttiker M 1996 *Phys. Rev. B* **54** 8130
- [148] Ng T-K 1996 *Phys. Rev. Lett.* **76** 487
- [149] Pei-Qing J, Marthaler M, Cole J H, Shnirman A and Schön G 2011 *Phys. Rev. B* **84** 035322
- [150] Pei-Qing J, Marthaler M, Cole J H, Shnirman A and Schön G 2012 *Phys. Scr.* **T151** 014032
- [151] Jin J, Marthaler M, Pei-Qing J, Golubev D and Schön G 2013 *New J. Phys.* **15** 025044
- [152] Kulkarni M, Cotlet O and Türeci H E 2014 *Phys. Rev. B* **90** 125402
- [153] Lambert N, Nori F and Flindt C 2015 *Phys. Rev. Lett.* **115** 216803
- [154] Karlewski C, Heimes A and Schön G 2016 *Phys. Rev. B* **93** 045314
- [155] Marthaler M, Utsumi Y and Golubev D S 2015 *Phys. Rev. B* **91** 184515
- [156] Gullans M, Stehlik J J, Liu Y-Y, Eichler C, Petta J R and Taylor J M 2016 *Phys. Rev. Lett.* **117** 056801
- [157] Stover H L and Steier W H 1966 *Appl. Phys. Lett.* **8** 91
- [158] André S, Pei-Qing J, Brosco V, Cole J H, Alessandro Romito A, Shnirman A and Schön G 2010 *Phys. Rev. A* **82** 053802
- [159] André S, Brosco V, Marthaler M, Shnirman A and Schön G 2009 *Phys. Scr. T* **137** 014016
- [160] Astafiev O, Inomata K, Niskanen A O, Yamamoto T, Pashkin Yu A, Nakamura Y and Tsai J S 2007 *Nature* **449** 588
- [161] Franck J, Manchester F and Martin D 1961 *Proc. R. Soc. A* **263** 494
- [162] Kondo J 1964 *Prog. Theor. Phys.* **32** 37
- [163] Cronenwett S M, Oosterkamp T H and Kouwenhoven L P 1998 *Science* **281** 540
- [164] Goldhaber-Gordon D *et al* 1998 *Nature* **391** 156
- [165] Nygård J, Cobden D H and Kondo L P E 2000 *Nature* **408** 342
- [166] Deng G-W *et al* 2015 arXiv:1509.06141
- [167] Desjardins M M, Viennot J J, Dartiaill M C, Bruhat L E, Delbecq M R, Lee M, Choi M-S, Cottet A and Kontos T 2017 *Nature* **545** 71
- [168] Hofstetter L, Csonka S, Nygård J and Schönenberger C 2009 *Nature* **461** 960
- [169] Herrmann L G, Portier F, Roche P, Levy Yeyati A, Kontos T and Strunk C 2010 *Phys. Rev. Lett.* **104** 026801
- [170] Hofstetter L, Csonka S, Baumgartner A, Fülöp G, d'Hollosy S, Nygård J and Schönenberger C 2011 *Phys. Rev. Lett.* **107** 136801
- [171] Schindele J, Baumgartner A and Schönenberger C 2012 *Phys. Rev. Lett.* **109** 157002
- [172] Herrmann L G, Bursat P, Herrera W J, Portier F, Roche P, Strunk C, Levy Yeyati A and Kontos T 2012 arXiv:1205.1972
- [173] Schindele J, Baumgartner A, Maurand R, Weiss M and Schönenberger C 2014 *Phys. Rev. B* **89** 045422
- [174] Das A, Ronen Y, Heiblum M, Mahalu D, Kretinin A V and Shtrikman H 2012 *Nat. Commun.* **3** 1165
- [175] Deacon R S, Oiwa A, Sailer J, Baba S S, Kanai Y, Shibata K, Hirakawa K and Tarucha S 2015 *Nat. Commun.* **6** 7446
- [176] Kitaev A Y 2001 *Phys. Usp.* **44** 131
- [177] Ivanov D A 2001 *Phys. Rev. Lett.* **86** 268
- [178] Nayak C, Simon S H, Stern A, Freedman M and Das Sarma S 2008 *Rev. Mod. Phys.* **80** 1083
- [179] Mourik V, Zuo K, Frolov S M, Plissard S R, Bakkers E P A M and Kouwenhoven L P 2012 *Science* **336** 1003
- [180] Das A, Ronen Y, Most Y, Oreg Y, Heiblum M and Shtrikman H 2012 *Nat. Phys.* **8** 887
- [181] Deng M T, Yu C L, Huang G Y, Larsson M, Caroff P and Xu H Q 2012 *Nano Lett.* **12** 6414
- [182] Churchill H O H, Fatemi V, Grove-Rasmussen K, Deng M T, Caroff P, Xu H Q and Marcus C M 2013 *Phys. Rev. B* **87** 241401
- [183] Albrecht S M, Higginbotham A P, Madsen M, Kuemmeth F, Jespersen T S, Nygård J, Krogstrup P and Marcus C M 2016 *Nature* **531** 206
- [184] Deng M T, Vaitiekenas S, Hansen E B, Danon J, Leijnse M, Flensberg K, Nygård J, Krogstrup P and Marcus C M 2016 *Science* **354** 1557
- [185] Zhang H *et al* 2016 arXiv:1603.04069
- [186] Lutchyn R M, Sau J D and Das Sarma S 2010 *Phys. Rev. Lett.* **105** 077001
- [187] Oreg Y, Refael G and von Oppen F 2010 *Phys. Rev. Lett.* **105** 177002
- [188] Väyrynen J I, Rastelli G, Belzig W and Glazman L I 2015 *Phys. Rev. B* **92** 134508
- [189] Hassler F, Akhmerov A R and Beenakker C W J 2011 *New J. Phys.* **13** 095004
- [190] Hyart T, van Heck B, Fulga I C, Burrello M, Akhmerov A R and Beenakker C W J 2013 *Phys. Rev. B* **88** 035121
- [191] Müller C, Bourassa J and Blais A 2013 *Phys. Rev. B* **88** 235401
- [192] Xue Z-Y, Shao L B, Hu Y, Zhu S-L and Wang Z D 2013 *Phys. Rev. A* **88** 024303
- [193] Pekker D, Hou C-Y, Manucharyan V E and Demler E 2013 *Phys. Rev. Lett.* **111** 107007
- [194] Ginossar E and Grosfeld E 2014 *Nat. Commun.* **5** 4772
- [195] Ohm C and Hassler F 2014 *Phys. Rev. B* **91** 085406
- [196] Yavilberg K, Ginossar E and Grosfeld E 2015 *Phys. Rev. B* **92** 075143
- [197] Mendes U C and Mora C 2015 *New J. Phys.* **17** 113014
- [198] Xu C and Vavilov M G 2013 *Phys. Rev. B* **88** 195307
- [199] Contreras-Pulido L D, Emary C, Brandes T and Aguado R 2013 *New J. Phys.* **15** 095008
- [200] Lambert N, Flindt C and Nori F 2013 *Europhys. Lett.* **103** 17005
- [201] Bergenfeldt C, Samuelsson P, Sothmann B, Flindt C and Büttiker M 2014 *Phys. Rev. Lett.* **112** 076803
- [202] Bergenfeldt C and Samuelsson P 2013 *Phys. Rev. B* **87** 195427

- [203] Ye H, Peng Y-W, Yu Z-Y, Zhang W and Liu Y-M 2015 *Chin. Phys. B* **24** 114202
- [204] van den Berg T L, Bergenfeldt C and Samuelsson P 2014 *Phys. Rev. B* **90** 085416
- [205] Feng Z-B 2012 *Phys. Rev. A* **85** 014302
- [206] Gudmundsson V, Jonasson O, Tang C-S, Goan H-S and Manolescu A 2012 *Phys. Rev. B* **85** 075306
- [207] Jonasson O, Tang C-S, Goan H-S, Manolescu A and Gudmundsson V 2012 *New J. Phys.* **14** 013036
- [208] Abdullah N R, Tang C-S, Manolescu A and Gudmundsson V 2013 *J. Phys.: Condens. Matter* **25** 465302
- [209] Abdullah N R, Tang C-S, Manolescu A and Gudmundsson V 2014 *Physica E* **64** 254
- [210] Arnold T, Tang C-S, Manolescu A and Gudmundsson V 2014 *Physica E* **60** 170
- [211] Gudmundsson V, Sitek A, Lin P-y, Abdullah N R, Tang C-S and Manolescu A 2015 *ACS Photonics* **2** 930
- [212] Gudmundsson V, Sitek A, Abdullah N R, Tang C-S and Manolescu A 2016 *Ann. Phys.* **528** 394
- [213] Abdullah N R, Tang C-S, Manolescu A and Gudmundsson V 2016 *ACS Photonics* **3** 249
- [214] Gudmundsson V, Jonsson T H, Bernodsson M L, Abdullah N R, Sitek A, Goan H-S, Tang C-S and Manolescu A 2017 *Ann. Phys.* **529** 1600177
- [215] Gudmundsson V, Abdullah N R, Sitek A, Goan H-S, Tang C-S and Manolescu A 2017 *Phys. Rev. B* **95** 195307
- [216] Jauho A P, Wingreen N S and Meir Y 1994 *Phys. Rev. B* **50** 5528
- [217] Oliver W D, Yu Y, Lee J C, Berggren K K, Levitov L S and Orlando T P 2005 *Science* **310** 1653
- [218] Jooya H Z, Reihani K and Chu S-I 2016 *Sci. Rep.* **6** 37544
- [219] Leppäkangas J, Marthaler M, Hazra D, Jebari S, Johansson G and Hofheinz M 2017 arXiv:1612.07098